The Dynamics of Vehicular Traffic with Drivers' Reaction Time Delay

Gábor Orosz

Department of Engineering Mathematics

University of Bristol

A dissertation submitted to the University of Bristol in accordance with the requirements of the degree of Doctor of Philosophy in the Faculty of Engineering.

2005

Abstract

The dynamics of highway traffic is examined by investigating an optimal-velocity car-following model which includes the reaction time delay of drivers. Drivers with identical characteristics are considered and periodic boundary conditions are applied in space.

Bifurcations of the corresponding system of delay differential equations are studied analytically and by numerical continuation techniques. By investigating the linear stability of the uniform flow solution, Hopf bifurcations are identified and it is shown that the consequent oscillations correspond to travelling waves, with different wave numbers, that propagate against the flow of traffic.

After eliminating a continuous translational symmetry of the system, normal form calculations are carried out showing that the Hopf bifurcations are robustly subcritical due to the inclusion of the delay. Consequently, the resulting oscillations are unstable in the vicinity of the Hopf bifurcation points, revealing the possibility of bistable behaviour.

The full nonlinear dynamics of the system is investigated by numerical continuation techniques. By following branches of periodic solutions, regions in parameter space are determined where the stable uniform flow co-exists with periodic solutions corresponding to single or multiple traffic jams. Regions of stopping and collision are also computed. As the number of cars is increased, trends are identified by monitoring how the boundaries of these domains change.

It is shown that for large numbers of cars the periodic solutions develop stop-fronts and go-fronts corresponding to the entry and exit points of traffic jams. Detailed investigation of the stability of periodic solutions provides information about the low-dimensional dynamics of the amalgamation and the dispersion of traffic jams.

to Veronika

Acknowledgements

I would like to thank all of those who made my PhD achievable and enjoyable.

First of all, I would like to give special thanks to my supervisors, Eddie Wilson and Bernd Krauskopf, who continuously helped and supported me throughout my PhD. Their expertise and guidance were essential for the completion of this work. Particular thanks go to Eddie for his attentiveness during the process of writing up.

I gratefully acknowledge the help and support of Gábor Stépán whose contribution to this research was irreplaceable. I also thank him for the encouraging emails and long telephone calls despite his hectic and busy life.

I would like to say thanks to Alan Champneys for his valuable comments during the annual review meetings and to John Hogan for his continuous encouragement.

I really appreciate the support of my colleagues at the Department of Engineering Mathematics who also tolerated my idiosyncrasies. Special thanks goes to David Barton, Kirk Green, Jan Sieber, Róbert Szalai and Róbert Vértesi for the scientific conversations, and to Enza di Tomaso, Luke Carrivick, Piotr Kowalczyk, John Malone and Petri Piiroinen for non-scientific conversations.

I thank my father Sándor Orosz very much for the many different kinds of support he has provided. It was always great to visit my family and feel like I was really at home.

Most of all, I would like to thank my girlfriend Veronika Tóth. Without her love, patience, and encouragement I would never have completed this work. She was always able to make sunshine in this rainy place.

Author's Declaration

I declare that the work in this dissertation was carried out in accordance with the regulations of the University of Bristol. The work is original except where indicated by special reference in the text and no part of the dissertation has been submitted for any other degree.

Any views expressed in the dissertation are those of the author and in no way represent those of the University of Bristol.

The dissertation has not been presented to any other University for examination either in the United Kingdom or overseas.

Signed: .....

Date: .....

Contents

List of Figures

List of Tables

Chapter 1

Introduction

Every day the demand for travel increases and consequently roads are becoming more congested. Congestion results in increased travel times and exhaust fume emissions [2, 4, 11, 12]. Politicians have thus realised that it is necessary to tackle congestion, either by suppressing the demand for travel or by sponsoring improved methods of traffic management. For example, in the UK the Department of Transport has developed a Ten Year Plan [13] for the reduction of congestion. Broadly speaking, roads may be categorised as either (i) part of a dense urban network or (ii) part of the long distance trunk road/motorway network. This thesis is concerned with some modelling aspects of the latter.

The economical significance of motorways is enormous. In the UK motorways constitute only one percent of the entire road network in length, but provide approximately one fifth of the country's overall traffic (measured in vehicle kms) [10]. Furthermore, Britain's motorway traffic has increased by more than one third in the last ten years.

Information technology is making available new methods for the measuring, control and optimisation of motorway traffic. For instance, in the UK the Highways Agency [3] has developed the MIDAS (Motorway Incident Detection and Automatic Signalling) temporary speed limit system [7]. The agency has also created the ATM (Active Traffic Management) system [1] where vehicles are diverted to run on hard shoulders at peak times, and the RM

(Ramp Metering) system [9] where the flow of vehicles joining the main carriageway from entry slip roads is controlled by traffic lights. Note that ramp metering is also in use in the USA in many urban areas [8].

Here we give a brief overview of the MIDAS system, which was first installed on London's M25 orbital motorway [5]. The system consists of a distributed network of traffic and weather sensors, and in the case of the M25, variable speed limit signs which control traffic speeds with little human supervision. Speed and flow data is collected by double inductance loops every 500m along the carriageway and this data can be post-processed and used to visualize the macroscopic (by which we mean over large length and long time scales) dynamics of traffic.

In Fig. 1.1 a space time diagram is depicted showing a 17.5 km long section of the M25 during a four and half hour time interval. Each of the 36 sensors averages the velocity of traffic at one minute intervals and a colour is applied according to the computed average velocity. High and low velocity regions are indicated by blue and red colours, as detailed in the colour bar on the right-hand side of the figure. One may recognize that the flow is not homogenous, instead, low and high velocity regions alternate in space, forming patterns which propagate upstream (opposite to the flow of vehicles). This moving pattern consists of so-called *stop-and-go waves*.

It is possible to reconstruct the motion of (hypothetical) individual vehicles (shown by black curves in Fig. 1.1), so that the slope of the $x(t)$ curves are given by the measured average velocities. When driving through stop-and-go waves, vehicles decelerate, stand still/drive slowly, and then accelerate. Thus, patters are formed by vehicles' collective motion. The emergent stop-and-go waves are sometimes called 'phantom' traffic jams since drivers are unable to observe their original cause, because they are far away (both in space and time) from the point where the traffic jam is initiated. It is curious to note that such large-scale structures exist given that drivers tend only to make microscopic actions in response to the speed limit signs and to the motion of the preceding vehicles.

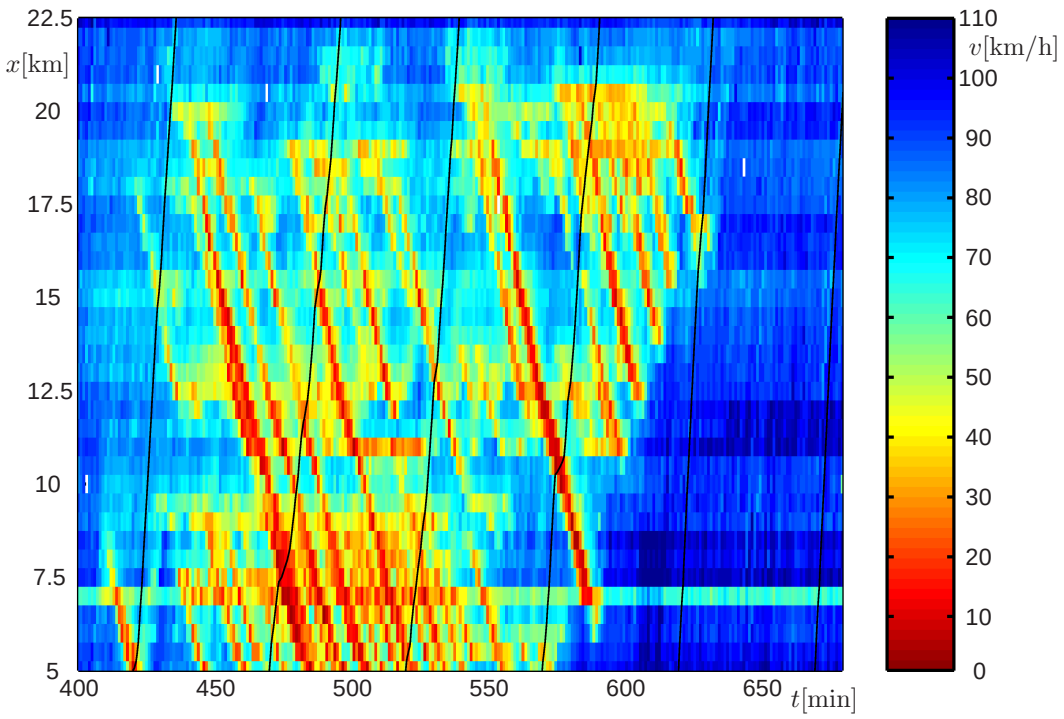

Fig. 1.1: Spatio-temporal plot of a section of one carriageway of London's M25 ring road. The measurements are made with the help of the inductance loops of the MIDAS system. High velocity regions are depicted as blue and low velocity regions as red, according to the colour bar on the right-hand side. The black curves indicate (typical, not measured) vehicle trajectories.

In order to optimize systems like MIDAS we have to understand the fundamental macroscopic dynamics of highway traffic (what happens over large time and length scales). It is possible to construct macroscopic models that describe the dynamics in terms of density and velocity distributions in space and to compare the obtained results with measurements. However, ultimately traffic flow is a discrete phenomenon, so it is important to understand how macroscopic dynamics results from microscopic models of driver behaviour. In the mathematics and physics literature of microscopic traffic models, the psychological reactions of drivers are grossly simplified, but even so they may qualitatively reproduce the correct macroscopic stop-and-go waves whose wavelengths are many times the separation of individual vehicles; see, e.g., [15, 107].

Fig. 1.2 shows a spatio-temporal diagram produced by the microscopic model investigated

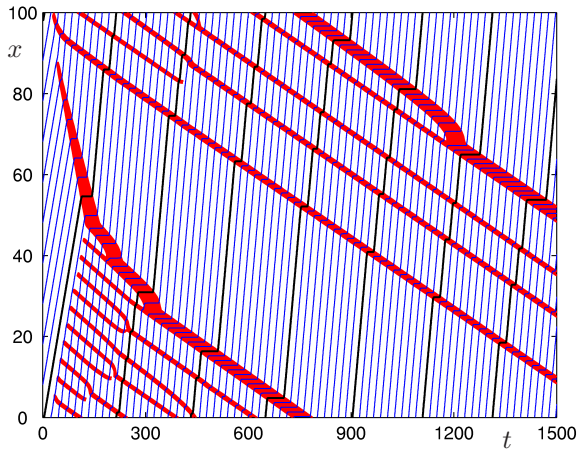

Fig. 1.2: Spatio-temporal plot of a ring road obtained from the model analysed in this thesis when the uniform flow is linearly unstable. Due to the periodic boundary conditions, the boundaries $x \equiv 0$ and $x \equiv L = 100$ are equivalent. The stop-and-go traffic jams are shown in red. The trajectories of every fifth forward travelling vehicle are shown by blue curves (the trajectory of the first vehicle is emphasized in black).

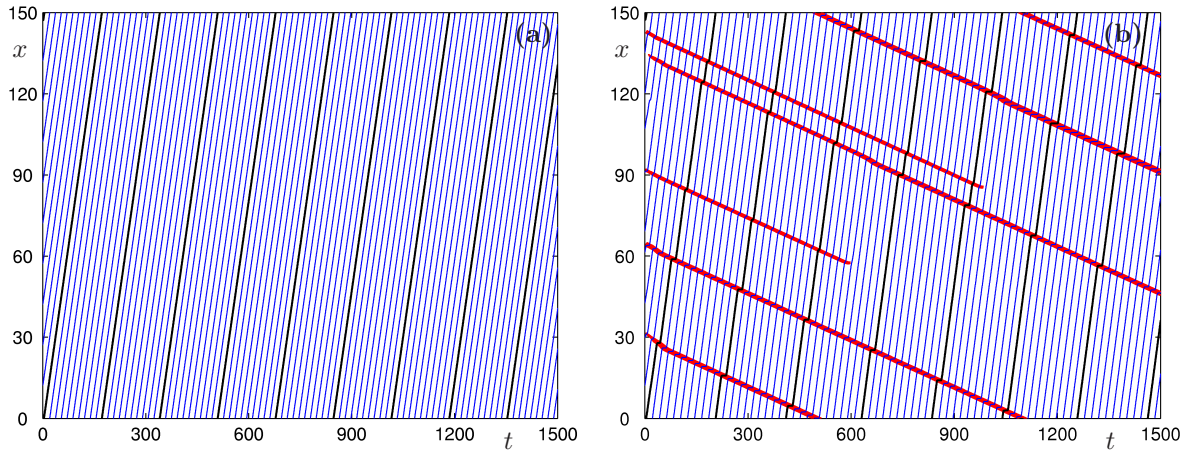

Fig. 1.3: Spatio-temporal plots of a ring road obtained from the model analysed in this thesis when the uniform flow is linearly stable. Due to the periodic boundary conditions, the boundaries $x \equiv 0$ and $x \equiv L = 150$ are equivalent. The stop-and-go traffic jams are shown in red. The trajectories of every fifth forward travelling vehicle are shown by blue curves (the trajectory of the first vehicle is emphasized in black). Panel (a) demonstrates the linear stability of the uniform flow, while panel (b) shows that, by applying sufficiently large perturbations, stop-and-go traffic jams may occur.

in this thesis. Stop-and-go waves propagate backward along a circular road. Traffic jams (red regions) are detected when vehicles' velocities drops below one third of the velocity of sparse

uniform flow. The blue and black curves show how individual drivers pass through these waves. Note that both the macroscopic and microscopic results agree qualitatively with the MIDAS measurements, compare Fig. 1.1 and Fig. 1.2.

The main focus of this thesis is to investigate the dynamics of microscopic models and the emerging macroscopic features. Particularly, we focus on a so-called optimal velocity car-following model where driver behaviour is modelled by differential equations. In this thesis, the technical challenge from the mathematical point of view is the inclusion of delay to model the reaction time of drivers. The principal advances are two-fold:

1. This is the first time that the nonlinear dynamics of a traffic model has been investigated systematically by using bifurcation tools. These investigations provide a deep insight into the dynamics ruled by stable and unstable oscillations.

2. We manage to go beyond the simplest ordinary differential equation case and deal with technically challenging delay differential equations. Thus are we able to study the robust effects caused by the drivers' reaction time delay.

The mathematical tools used in this work are principally from analytical and numerical bifurcation theory, including the application of the numerical continuation package DDE-BIFTOOL [36]. With these tools branches corresponding to uniform flow and stop-and-go wave solutions may be determined as functions of parameters. Bifurcation points can also be detected on these branches showing where the dynamics change qualitatively. Since both stable and unstable solutions can be found, this approach allows us to describe even the 'hidden' dynamics of the system, which cannot be explored by numerical simulation. Consequently, applying bifurcation analysis and numerical continuation is a much more efficient way to explore parameter space than the repeated use of numerical simulation.

While the microscopic models without delay are described by ordinary differential equations (ODEs) presenting the dynamics in finite-dimensional phase spaces, the appearance of the reaction time leads to delay differential equations (DDEs) and to infinite-dimensional phase spaces. The finite-dimensional bifurcation theory that is available in basic textbooks

[47, 73] has been extended to DDEs in [31, 49, 50, 67]. The infinite-dimensional dynamics make the bifurcation analysis more abstract and complicated: functionals and operators need to be handled analytically and their discretised counterparts, (i.e., large matrices) are tackled in numerical tools; see Chapter 2.

In the mathematics and physics literature, linear stability arguments have been used before to investigate the formation of traffic jams [53, 63]. Actually, traffic jam formation had been equated with linear instability of the *uniform flow equilibrium* (a kind of steady state where equidistant vehicles flow with the same time-independent velocity); see Fig. 1.2 for demonstration of this instability. However, it is also thought among traffic engineers that certain events, like a truck pulling out of the slow lane, can trigger traffic jams even when the uniform flow is stable. One of the key advances here is a proper examination of the subcriticality of bifurcations and the co-existence of the stable uniform flow with stable stop-and-go waves. In parameter ranges of co-existence, large enough perturbations can still lead to pattern formation even when the uniform flow is linearly stable.

An initial demonstration of this co-existence is given in Fig. 1.3. Panel (a) demonstrates a case when the uniform flow equilibrium is (linearly) stable. However, as shown in panel (b), by applying sufficiently large random perturbations in vehicles' separations and velocities one can obtain stop-and-go waves in this case as well. This co-existence effect is analysed in Chapters 3 and 4 by applying analytical and numerical bifurcation theory. In Chapter 5 it is shown that numerical bifurcation analysis also allows us to investigate the long-time merging and dispersing dynamics of traffic jams; see Fig. 1.2 and Fig. 1.3(b).

1.1 Review of modelling approaches for vehicular traffic

In this section we give a brief review of the mathematics and physics literature of simplified highway traffic models. In fact, traffic engineers use much more complicated models, for example, as implemented in the software packages AIMSUN, DRACULA, PARAMICS, SISTM, and VISSIM [6]. However, the dynamics of these complicated systems may only be

investigated by numerical solution of the initial value problem. In contrast, detailed investigation of the dynamics of simple models is necessary for the basic understanding of the pattern formation mechanisms of real-world traffic. For more discussion and a much more detailed review see Helbing [53].

A central question in all models is what scales need to be represented. There are *macroscopic models* which do not consider individual vehicles but rather deal with continuous density and velocity distributions as functions of space and time. These so-called *continuum models* describe the dynamics by partial differential equations (PDEs). There are also *microscopic models* which model at the level of individual vehicles. These include two types of models, namely car-following models and cellular automata models. In *car-following models* discrete entities move in continuous space and time and the vehicles' motions are described by ordinary differential equations (ODEs) or by delay differential equations (DDEs). In *cellular automata models*, not only cars but also space, time, and velocities are considered to be discrete and update rules are used to describe the time development of the system.

1.1.1 Continuum models

In continuum models, individual vehicles are neglected and traffic is modelled via a density distribution $\rho(x,t)$ and a velocity distribution $v(x,t)$ which are continuous functions of position x and time t. In all such models, we have conservation of vehicles, so that in the absence of sources and sinks due to on- and off-ramps,

$$\rho_t + (\rho v)_x = 0\,, \tag{1.1}$$

where the subscripts t and x stand for partial derivation. (Further refinements are possible when one considers multi-species models [16], multi-lane models [26, 27, 46, 101], or junctions [20, 113].)

To close the model, either velocity or acceleration information must be provided. The simplest setting, introduced by Lighthill and Whitham [76], supplements (1.1) with

$$v = \mathcal{V}(\rho)\,, \tag{1.2}$$

where $\mathcal{V}(\rho)$ is a decreasing function which models that dense traffic should travel slower than sparse traffic for safety reasons. If we initialize this model so that fast traffic is placed behind slow traffic, the solution profile sharpens and a discontinuous shock develops in finite time, at which vehicles' velocities jump downwards. By investigating the so-called *fundamental diagram*, which is the plot of the flow $Q(\rho) = \rho v$ against density ρ, we obtain information about the propagation of shocks. This analysis indicates that, in a wide range of situations, shocks propagate against the flow of traffic in accordance with the empirical data shown in Fig. 1.1; for more details see Whitham's book [118].

However, not all empirical features can be captured by the Lighthill-Whitham model, and for this reason, second order models have been developed in the form

$$v_t + vv_x = \alpha\big(\mathcal{V}(\rho) - v\big) + N\,, \tag{1.3}$$

where the left-hand side expresses the total derivative of the velocity. The first term on the right-hand side corresponds to relaxation to a density dependent *optimal velocity* given by $\mathcal{V}(\rho)$ with a relaxation time $1/\alpha$. Note that this idea also appears in microscopic modelling as explained further below. The second term on the right-hand side is chosen as $N = -\mu\rho_x/\rho$ by Payne [90], as $N = -\mu\rho_x/\rho - \nu v_{xx}$ by Kühne [72], and as $N = -\mu\rho_x/\rho - \nu v_{xx}/\rho$ by Kerner and Konhäuser [65]. The *pressure terms* $\sim \rho_x$ model anticipation of drivers to events ahead of them on the road, that is, increasing/decreasing density produces deceleration/acceleration, while the *diffusion term* $\sim v_{xx}$ corresponds to the averaged effects of noise. By including these extra terms, the model (1.3) is able to reproduce uniform flow as well as stop-and-go travelling waves (without discontinuities) in correspondence with empirical data; see Fig. 1.1. However, it is not obvious what pressure and viscosity correspond to at the microscopic level. Therefore, most recently, continuum models have also been developed from microscopic models; see [18, 74].

We note that Boltzman-type gas-kinetic models, which are based on 'collisions' of particles, contain noise explicitly as established by Prigogine and Herman [93] and developed by Helbing [52]. However, these models cannot be written in the form (1.3).

The partial differential equations (PDEs) (1.1) and (1.3) can be investigated using analytical methods and numerical simulation, and the results can be compared directly to the results of empirical measurements, e.g., through the fundamental diagram [62, 66]. However, one has to bear in mind the limitations due to the fact that fundamentally discrete systems are being modelled as a continuum.

As mentioned before, microscopic models dealing with individual cars can also reproduce the macroscopic waves appearing on freeways. There are two main types of microscopic modelling approaches considered in the literature, namely car-following models and cellular automata models.

1.1.2 Car-following models

Car-following models are the focus of this thesis. In these models vehicles are considered as discrete entities moving in continuous time and continuous one-dimensional space; see Fig. 1.4. At time t positions of cars are denoted by $x_i(t)$, their velocities by

$$v_i(t) = \dot{x}_i(t)\,, \tag{1.4}$$

and their relative displacements, usually called the *headways*, by

$$h_i(t) = x_{i+1}(t) - x_i(t)\,, \tag{1.5}$$

as is shown in Fig. 1.4. Consequently, the relative velocities are given by the rate of headways, i.e.,

$$\dot{h}_i(t) = v_{i+1}(t) - v_i(t)\,. \tag{1.6}$$

Note that each of the above quantities is a function of the time t, and the dot denotes derivation with respect to t.

To simplify matters, drivers with identical characteristics are usually considered and the accelerations $\dot{v}_i$ of vehicles are given as a function of stimuli which are usually the headway, the relative velocity, and the velocity, that is,

$$\dot{v}_i(t) = f\big(h_i(t-\tau), \dot{h}_i(t-\sigma), v_i(t-\kappa)\big)\,. \tag{1.7}$$

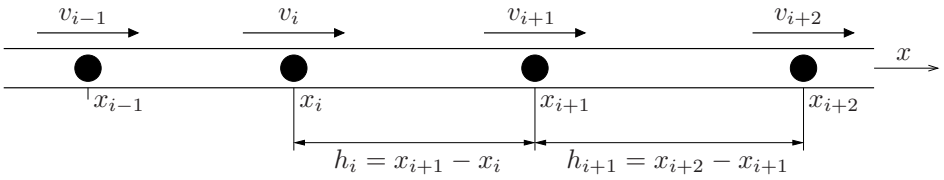

Fig. 1.4: Sequence of cars on a single-lane road in a car-following model showing vehicles' positions, velocities, and headways.

The *reaction time delays* $\tau, \sigma, \kappa \geq 0$ are generally different, but sometimes, for the sake of simplicity, they are considered to be equal to each other or even to be zero. The dynamical equation (1.7) together with any of the supplementary kinematic conditions (1.4) or (1.6) constitute a system of delay differential equations (DDEs), which is simplified to a system of ordinary differential equations (ODEs) for $\tau = \sigma = \kappa = 0$. (Of course, when the constraint (1.4) is considered the definition (1.5) is substituted into (1.7).)

The study of car-following models began in the fifties by Herman and his colleagues [25, 40, 41], constructing models of the form

$$\dot{v}_i(t) = \alpha \frac{v_i(t)^{s_1} \dot{h}_i(t-\tau)^{s_2}}{h_i(t-\tau)^{s_3}}, \quad s_1, s_2, s_3 \in \mathbb{N}, \tag{1.8}$$

and investigating the linear stability of the uniform flow equilibrium. However, they were not able to investigate the nonlinear behaviour due to limitations in computing at that time. Comparing (1.8) with the general setup (1.7), one can see that $\kappa = 0$ and $\tau = \sigma > 0$ is considered here. Further models in this class were investigated later by analytical and numerical methods [33, 77, 91].

Other models, like Newell's [82], were also constructed where, rather than acceleration, velocities v_i are given as a function of stimuli, that is,

$$v_i = \mathrm{V}(h_i(t-\tau)), \tag{1.9}$$

which does not conform to (1.7), but rather is similar to the continuum model (1.2). Nevertheless, (1.9) still reproduces some qualitative dynamics correctly as is shown in [58]. Also more complicated models, such as that of Gipps [42], have been investigated in detail [119]. Reviews of the above car-following models are given by Berg [17] and by Holland [57].

Development and investigation of higher fidelity car-following models is still an ongoing procedure. For example, one may consider the generalized force model [54] and the intelligent driver model [113] built by Helbing *et al.*, the model of Safonov *et al.* [95, 96] (with and without delay), and the recent model of Gasser *et al.* [38].

There are two obvious extensions of the general car-following model (1.7). One of them is the so-called *multi-look-ahead* approach [55, 75, 99, 114, 121]. Here drivers respond to the motion of more than one vehicle ahead. For example, a *double-look-ahead* model is generally described by the DDEs

$$\dot{v}_i(t) = f\big(h_i(t-\tau), \dot{h}_i(t-\sigma), v_i(t-\kappa), (h_i+h_{i+1})(t-\gamma), (\dot{h}_i+\dot{h}_{i+1})(t-\delta)\big)\,, \tag{1.10}$$

where $\tau, \sigma, \kappa, \gamma, \delta \geq 0$, and indeed the relative displacements $h_i(t) + h_{i+1}(t) = x_{i+2}(t) - x_i(t)$ and the relative velocities $\dot{h}_i(t) + \dot{h}_{i+1}(t) = v_{i+2}(t) - v_i(t)$ appear in the right-hand side; see Fig. 1.4. It can be shown that these next-nearest neighbourhood interactions can stabilise the uniform flow. Furthermore, there exist multi-species models [79, 80] that consider drivers with different characteristics and consequently the system

$$\dot{v}_i(t) = f_i\big(h_i(t-\tau_i), \dot{h}_i(t-\sigma_i), v_i(t-\kappa_i)\big)\,, \tag{1.11}$$

with $\tau_i, \sigma_i, \kappa_i \geq 0$. However, usually only two different species are mixed corresponding to cars and lorries. One might also construct car-following models which are capable of modelling multilane traffic or junctions [30, 56, 78, 97].

It is also possible to include noise to model that drivers are not deterministic (they change their behaviour from time to time) and to model external disturbances (such as the weather or road unevenness). However, in the current mathematics and physics literature car-following models with noise are not typical. Many of them use dicretised time (but still continuous space and velocity), e.g., [64, 70, 110] and only a few of them consider continuous time [111, 112].

A famous class of car-following models are the so-called *optimal velocity (OV) models* where the accelerations are given by

$$\dot{v}_i(t) = \alpha\big(\mathrm{V}(h_i(t-\tau)) - v_i(t-\kappa)\big)\,. \tag{1.12}$$

Here $\alpha > 0$ is known as the *sensitivity* and $\mathrm{V}(h)$ is known as the *optimal velocity (OV) function*. In this model, drivers wish to achieve the optimal velocity given by $\mathrm{V}(h)$ in a characteristic *relaxation time* $T = 1/\alpha$.

The first OV model, called the California model [25], contained a linear OV function and set the delays $\tau = \kappa > 0$. The first nonlinear OV function was introduced by Bando *et al.* [15] in the mid-nineties who also chose the simple setup $\tau = \kappa = 0$ and obtained the ODEs

$$\dot{v}_i(t) = \alpha\big(\mathrm{V}(h_i(t)) - v_i(t)\big)\,. \tag{1.13}$$

Using numerical simulation they were able to reproduce traffic waves when the uniform flow equilibrium was unstable. This model generated much interest and many modifications and extensions; for example, piecewise linear OV functions were used in [107] and delays $\tau = \kappa > 0$ were included in [14] while delays $\tau > 0$, $\kappa = 0$ were applied in [28, 29]. The last of these is considered in this thesis as detailed in Section 1.2. Most of the authors used numerical simulation to examine the model (1.13), but in some recent articles bifurcation tools have begun to be applied [19, 39].

1.1.3 Cellular automata models

Cellular automata models are similar to car-following models, but they involve discrete vehicles moving in discrete time and space with discrete velocities. The road is divided into cells of a certain size which can be occupied by one car only (see Fig. 1.5), and the discretised velocity v can take only the integer values $0, 1, \ldots, v^{\max}$. The time development of the system is governed by a couple of updating rules in each time step. One of the most widely analysed updating schemes, proposed by Nagel and Schreckenberg [81], is described in Fig. 1.5. Note that car-following models may be obtained as natural continuum limits of cellular automata models; see [70].

Since each quantity in cellular automata models is discrete, a quick realization of numerical simulations is possible. Cellular automata models are found to be successful models of highways [98], and they are also applicable to model city traffic since it is easy to introduce

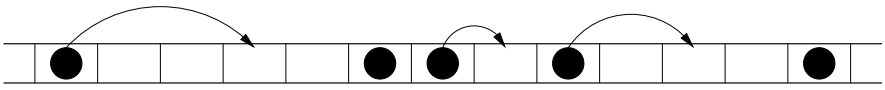

- if the velocity v of a vehicle is smaller than the speed $v^{\max}$ and the distance to the preceding car is larger than $v+1$, then the velocity is increased by 1;
- if a driver with velocity v sees the car ahead at distance $j < v$ it reduces its velocity to $j-1$;
- the velocity of each car is decreased by 1 with probability p when $v > 0$;
- each vehicle is advanced by as many sites as the value of its velocity.

Fig. 1.5: Cell hopping on a single lane according to the updating rules of the Nagel-Schreckenberg cellular automata model [81].

junctions and traffic lights [117].

1.2 Details of the model used in this thesis

In this section we describe the delayed optimal velocity car-following model that is subject to detailed investigation within the main body of this thesis. We chose a very simple optimal velocity model which nevertheless describes certain features of traffic correctly at the qualitative level.

We consider drivers with identical characteristics and the optimal velocity model given by (1.12). Furthermore, we take the assumptions $\tau > 0$ and $\kappa = 0$, that is, the accelerations of vehicles are given by

$$\dot{v}_i(t) = \alpha\big(\mathrm{V}(h_i(t-\tau)) - v_i(t)\big)\,. \tag{1.14}$$

Recall that α is the *sensitivity*, τ is the *reaction time delay* of the drivers, and $\mathrm{V}(h)$ is the *optimal velocity function*. Note that τ is different from the characteristic *relaxation time* $T = 1/\alpha$ for adjustment of the vehicles' velocities. Considering the kinematic conditions (1.6), the corresponding equations (1.6) and (1.14) constitute a system of delay differential equations (DDEs) for the vehicles' motions. (Of course, one may consider the kinematic conditions (1.4) and the corresponding DDE system (1.4),(1.14)). The model (1.14) has recently been investigated with numerical simulation by Davis [28, 29]. The case where (the

same) delay occurs both in the drivers' perceptions of their headway and in their perceptions of their own velocities (i.e., $\tau = \kappa > 0$) was considered by Bando *et al.* [14]. In our view, it is more realistic to suppose that drivers know their speed, i.e., they react to it instantaneously, but they react only to their headway via the delay τ.

We consider a single-lane model without overtaking (as shown in Fig. 1.4), but to further simplify matters we suppose that n vehicles are placed on a circular road of length L, so that

$$\sum_{i=1}^{n} h_i(t) = \sum_{i=1}^{n-1}(x_{i+1}(t) - x_i(t)) + (x_1(t) - x_n(t) + L) = L\,. \tag{1.15}$$

All OV models (1.12) (including (1.14)) admit a one-parameter family of *uniform flow equilibrium* solutions of the form

$$h_i^{\mathrm{eq}}(t) \equiv h^*\,, \quad v_i^{\mathrm{eq}}(t) \equiv v^*\,, \quad i = 1, \ldots, n\,. \tag{1.16}$$

When considering the system on the closed ring we obtain

$$h^* = L/n > 0\,, \quad v^* = \mathrm{V}(h^*)\,. \tag{1.17}$$

This yields

$$x_i^{\mathrm{eq}}(t) = v^* t + x_i^*\,, \quad i = 1, \ldots, n\,, \tag{1.18}$$

where

$$x_{i+1}^* - x_i^* = x_1^* - x_n^* + L = h^*\,, \quad i = 1, \ldots, n-1\,. \tag{1.19}$$

Previous studies in both ODE and DDE settings have been concerned with the linear stability calculation of the uniform flow solution and numerical simulation when the flow is unstable [14, 15, 28, 29, 107]. The loss of linear stability of uniform flow solutions is widely accepted as a cause of traffic jams. However, in this thesis we show that this is not necessary for traffic jam formation.

The main task now is to identify desirable properties of the OV function $\mathrm{V}(h)$ and to estimate physical ranges for the parameters. Since $\mathrm{V}(h)$ describes the uniform flow equilibria, the following properties seem necessary from the modelling point of view:

1. $\mathrm{V}(h)$ is continuous, nonnegative, and monotone increasing. (Drivers wish to travel forward and the desired velocity should increase smoothly as headway increases. Note that if $\mathrm{V}(h)$ were to attain negative values, there would exist unrealistic equilibria where vehicles reverse.)

2. $\mathrm{V}(h) \to v^0$ as $h \to \infty$. (In the case of very large headway, the desired velocity should approach an upper limit v^0 called the *desired speed*. This limit should be related to the legal speed limit.)

3. There exists a *jam headway* $h_{\mathrm{stop}} \geq 0$ such that $\mathrm{V}(h) \equiv 0$ for $h \in [0, h_{\mathrm{stop}}]$. (If cars become too closely packed, then drivers want to come to a full stop.) In our view, one should take h_{stop} strictly positive. Firstly, this is because real vehicles have finite length, so that small positive headways correspond to collisions, and secondly because real traffic flows have a finite characteristic jam density at which traffic comes to a complete stop.

Note that a further advantage of choosing $h_{\mathrm{stop}} > 0$ is that maximum principles may be used to show that vehicles do not reverse under *any* (even dynamic) situations, for either model (1.13) or (1.14). However, it is still possible for vehicles to collide if other parameters are chosen appropriately.

In the original paper by Bando *et al.* [15], the OV function was given (in rescaled coordinates) by

$$\mathrm{V}_{\mathrm{B1}}(h) = \tanh(h-2) + \tanh(2)\,. \tag{1.20}$$

It may be shown that this OV function satisfies each of the properties 1.–3. above, although with $h_{\mathrm{stop}} = 0$, which we do not regard as suitable. The later paper of Bando *et al.* [14] uses a dimensional OV function of the form

$$\mathrm{V}_{\mathrm{B2}}(h) = 16.8\big(\tanh(0.086(h-25)) + 0.913\big)\,, \tag{1.21}$$

which was fitted to Japanese highway traffic data. Here h is measured in meters and $\mathrm{V}(h)$ in meters per second. It may be shown that $h_{\mathrm{stop}} \simeq 7.0319$ m and $v^0 \simeq 32.1384$ ms^{-1}.

Table 1.1: Dimensional parameters with estimates of their ranges.

Name	Symbol	Estimated values
Reaction time	τ	$0.5 - 2$ s
Relaxation time	$T = 1/\alpha$	$0.5 - 50$ s
Sensitivity	α	$0.04 - 2$ s^{-1}
Desired speed	v^0	$10 - 35$ ms^{-1}
Jam headway	h_{stop}	$2 - 15$ m
Average headway	$h^* = L/n$	...

However, $\mathrm{V}_{\mathrm{B2}}(h)$ is a poor model for small headways since it is negative for $h \in [0, h_{\text{stop}}]$. Thus properties 1.–3. are satisfied by the OV function

$$\mathrm{V}_{\mathrm{B3}}(h) = \max[0, \mathrm{V}_{\mathrm{B2}}(h)]\,. \tag{1.22}$$

The numerical continuation method used in this thesis requires the continuous differentiability of the model's right-hand side in terms of its dependent variables. Since $\mathrm{V}'_{\mathrm{B3}}(h)$ is not continuous at $h = h_{\text{stop}}$, we must use a different OV function. Our goal is therefore to choose an OV function $\mathrm{V}(h)$ that satisfies properties 1.–3. with $h_{\text{stop}} > 0$ and for which $\mathrm{V}'(h)$ is continuous. The OV function should also have the correct S shape, i.e., we require $\mathrm{V}'(h)$ to have a single maximum strictly to the right of h_{stop}.

Table 1.2: Non-dimensionalized parameters and their ranges.

Name	Symbol and Definition	Estimated values
Sensitivity	$\tilde{\alpha} = \tau\alpha = \tau/T$	$0.02 - 4$
Desired speed	$\tilde{v}^0 = v^0\tau/h_{\text{stop}}$	$0.33 - 35$
Average headway	$\tilde{h}^* = h^*/h_{\text{stop}}$	...

Our approach is to first non-dimensionalize (1.14). Since we assume that $\tau, h_{\text{stop}} > 0$, we may introduce the rescaled variables $\tilde{t} := t/\tau$ and $\tilde{h} := h/h_{\text{stop}}$. All speed-like quantities (including the OV function) have rescalings of the form $\tilde{v} = v\tau/h_{\text{stop}}$. To simplify notation

we remove tildes, so that the rescaled version of (1.14) becomes

$$\dot{v}_i(t) = \alpha\big(\mathrm{V}(h_i(t-1)) - v_i(t)\big)\,. \tag{1.23}$$

Table 1.1 suggests ranges for dimensional parameters and Table 1.2 gives the non-dimensionalized counterparts. The dimensional desired speed v^0 corresponds to the speed limit or to a speed chosen according to weather and road conditions. The dimensional relaxation time $T = 1/\alpha$ is approximately the time which is needed for a single vehicle to reach the desired speed.

Note that definition (1.5) and the kinematic conditions (1.4) and (1.6) keep their form after rescaling. Furthermore, the uniform flow equilibrium may still be written in the form (1.16) using rescaled quantities. The rescaled OV function $\mathrm{V}(h)$ has the following properties:

1. $\mathrm{V}(h)$ is continuously differentiable, nonnegative, and monotone increasing.
2. $\mathrm{V}(h) \to v^0$ as $h \to \infty$, where v^0 is the rescaled *desired speed*.
3. $\mathrm{V}(h) \equiv 0$ for $h \in [0, 1]$, so that 1 is the rescaled *jam headway*.

The remainder of this thesis uses the rescaled OV function

$$\mathrm{V}(h) = \begin{cases} 0\,, & \text{if} \quad 0 \le h \le 1\,, \\ v^0 \dfrac{\big((h-1)/s\big)^3}{1 + \big((h-1)/s\big)^3}\,, & \text{if} \quad h > 1\,, \end{cases} \tag{1.24}$$

which satisfies properties 1.–3. above, has the requisite shape, and is smooth at $h = 1$. This OV function possesses two non-dimensional parameters, namely v^0 and s. The former is determined by the dimensional version of v^0 and the applied rescaling. However, s is a wholly new parameter that describes how the OV function is stretched to the right of $h = 1$. In this thesis we choose $s = 1$; the parameter s may be varied to shift the value of h at which $\mathrm{V}'(h)$ attains its maximum.

Figures 1.6(a) and 1.6(b) compare (1.24) and its derivative (blue solid curves) with the

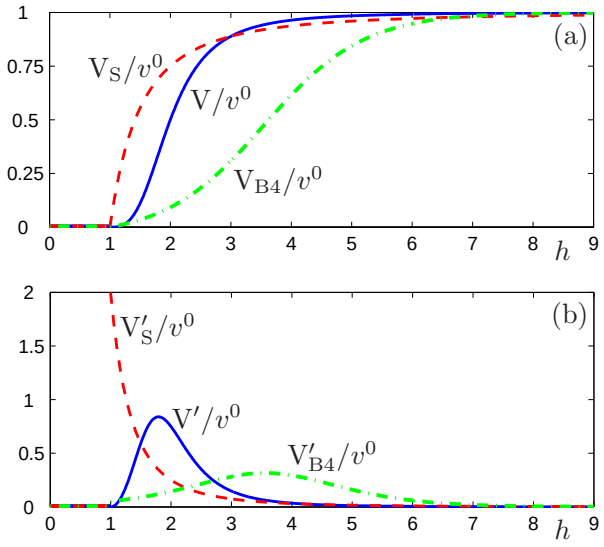

Fig. 1.6: Three different rescaled optimal velocity (OV) functions given by (1.24), (1.25), and (1.26) are shown in panel (a) as blue solid curve, green dashed-dotted curve, and red dashed curve, respectively. The corresponding derivatives with respect to the headway h are depicted in panel (b).

rescaled version of the OV function (1.22) defined by

$$V_{B4}(h) = \begin{cases} 0\,, & \text{if} \quad 0 \le h \le 1\,, \\ v^0\big(0.523\tanh(0.605h - 2.15) + 0.477\big)\,, & \text{if} \quad h > 1\,, \end{cases} \tag{1.25}$$

(green dashed-dotted curves). For comparison, we have also included a plot of the OV function

$$V_S(h) = \begin{cases} 0\,, & \text{if} \quad 0 \le h \le 1\,, \\ v^0\big(1 - 1/h^2\big)\,, & \text{if} \quad h > 1\,, \end{cases} \tag{1.26}$$

(red dashed curves), which does not have an S shape for $h > 1$.

The key point we wish to emphasize is that, although one may consider different OV functions, we have found that the results presented in this thesis are robust in the sense that the qualitative features do not depend on the precise analytical form of the OV function.

1.3 Outline of thesis

In this section we briefly summarize the framework of this thesis. The modelling issues have already been discussed earlier in this chapter. In Chapter 2 the theoretical background of delay differential equations is described since it is necessary for understanding in detail the technical results of the thesis. After some basic definitions related to the infinite-dimensional dynamics of DDEs, the stability and bifurcations of equilibria and periodic solutions are considered. Then we describe the basic tools used later in the thesis, namely, the analytical Hopf bifurcation calculations and the numerical continuation package DDE-BIFTOOL.

The detailed investigation of our traffic model is commenced in Chapter 3, where the stability of the uniform flow equilibrium and small amplitude oscillations are investigated analytically. First, Hopf bifurcations of equilibria are detected revealing oscillations and corresponding waves with several different wavelengths. The investigation of the criticality of these bifurcations via Hopf normal form calculations shows that fully-developed waves might co-exist with stable uniform flow. In order to carry out these investigations a theory of Hopf bifurcation calculations is developed for systems containing translational symmetry. The main work of this chapter has been published in [86, 87].

Chapter 4 is devoted to the detailed numerical investigation of the consequent oscillations and corresponding waves using numerical continuation techniques. First, for proof-of-concept purposes the system is investigated for $n = 3$ cars. Then the number of cars is increased towards more realistic traffic situations and the corresponding trends determined. In parameter space, regions of bistability and co-existence (between stable uniform flow and waves) are computed systematically. Furthermore, motions like collision or stopping are also investigated in detail. The main work of this chapter has been published in [85, 89].

Traffic waves are subject to further study in Chapter 5, where the long-time dynamics of the system is investigated. By using DDE-BIFTOOL, it is shown how unstable oscillations lead to stop-fronts and go-fronts moving relative to each other. The motions of these fronts are then studied by numerical simulation. The main work of this chapter has been published in

[85]. Finally, in Chapter 6 conclusions are drawn and possible future research is discussed.

Chapter 2

Review on delay differential equations with a single fixed delay

Equations (1.6) and (1.14) constitute a system of delay differential equations (DDEs) with a single fixed delay. We now recall some basic facts from the bifurcation theory for DDEs as needed in later chapters. In general form, such a system can be written as

$$\dot{x}(t) = f(x(t), x(t-\tau); \eta)\,, \tag{2.1}$$

where dot refers to derivation with respect to the time t, $x\colon \mathbb{R} \to \mathbb{R}^m$ is the state variable, the function $f\colon \mathbb{R}^m \times \mathbb{R}^m \times \mathbb{R}^l \to \mathbb{R}^m$ is differentiable, $\tau \in \mathbb{R}$ is the time delay, and $\eta \in \mathbb{R}^l$ is a (multi-dimensional) parameter. For system (1.6),(1.14) we have $m = 2n$ (or $m = 2n-1$ if we apply the condition (1.15)) and $l = 3$ corresponding to the parameters h^*, α and v^0.

The bifurcation theory of ordinary differential equations (ODEs) can be generalized to delay differential equations (DDEs) through the investigation of retarded functional differential equations (RFDEs) and operator differential equations (OpDEs); see Hale & Verduyn Lunel [50] or Diekmann *et al.* [31] for details. We recall the fundamental description of RFDEs and OpDEs in Section 2.1 showing the connection with DDEs, while the stability of equilibria and periodic orbits are discussed in Section 2.2.

The theory of normal form calculations for DDEs has been reviewed by Hale *et al.* in

[49]. For Hopf bifurcations of equilibria the first closed-form normal form calculations were executed by Hassard *et al.* [51] in the case of a simple scalar first order DDE, while Stépán presented first such calculations for system of DDEs [104, 105]. The normal form calculations, which are discussed in Section 2.3, use third order approximations to nonlinearities to find the criticality of bifurcations and the amplitude of oscillations in the vicinity of the bifurcation point. In Section 3.2, these calculations are extended to systems with translational symmetry. Using this method we carry out the Hopf calculations for system (1.4),(1.23) in Section 3.3.

In Section 2.4, we discuss the capabilities of the Matlab package DDE-BIFTOOL that has recently been developed by Engelborghs *et al.* [35, 36]. This continuation package can compute branches of stable and unstable equilibria and periodic solutions against a chosen bifurcation parameter. This numerical method uses the exact form of the nonlinearities, hence it provides reliable results even when the chosen bifurcation parameter is far away from its critical value taken at the bifurcation point. In Chapter 4 this package is applied to explore the global dynamics of system (1.6),(1.23).

2.1 Infinite-dimensional dynamics

In this section we explain how the dynamics of (2.1) become infinite-dimensional and consequently more complicated through the functional and the operator formalism of DDEs. Since the delay $\tau > 0$ in (2.1) we may introduce the rescaled time $\tilde{t} := t/\tau$ and the function $\tilde{f} := \tau f$. After rescaling we may drop the tildes immediately and obtain

$$\dot{x}(t) = f(x(t), x(t-1); \eta)\,. \tag{2.2}$$

Note that the rescaled model (1.4),(1.23) is written the above form. The vector $\eta \in \mathbb{R}^l$ consists of the rescaled bifurcation parameters, and we assume that for a fixed η there exist an equilibrium

$$x(t) = x(t-1) \equiv c\,, \tag{2.3}$$

where the constant vector $c = c(\eta) \in \mathbb{R}$ is defined by

$$f(c, c; \eta) = 0\,. \tag{2.4}$$

Note that initial data must be prescribed in the form of a continuous function over the interval $[-1, 0]$ with values in the physical space $\mathbb{R}^m$. Therefore, the phase space $\mathbb{X}_{\mathbb{R}^m}$ of $\mathbb{R} \to \mathbb{R}^m$ continuous functions, is infinite-dimensional. Particularly, in this section $[-1, 0] \to \mathbb{R}^m$ functions are considered.

Equation (2.4) can be written as a retarded functional differential equation (RFDE)

$$\dot{x}(t) = G(x_t; \eta)\,, \tag{2.5}$$

where dot refers to the derivative with respect to the (rescaled) time t, the state variable is $x\colon \mathbb{R} \to \mathbb{R}^m$, while the function $x_t\colon \mathbb{R} \to \mathbb{X}_{\mathbb{R}^m}$ is defined by the shift

$$x_t(\vartheta) = x(t + \vartheta)\,, \quad -1 \le \vartheta \le 0\,. \tag{2.6}$$

The nonlinear functional $G\colon \mathbb{X}_{\mathbb{R}^m} \times \mathbb{R}^l \to \mathbb{R}^m$ defined as

$$G(x_t; \eta) = g\bigg(\int_{-1}^{0} \mathrm{d}\gamma(\vartheta) \rho_\vartheta\big(x(t + \vartheta)\big); \eta \bigg)\,, \tag{2.7}$$

where $g\colon \mathbb{R}^m \times \mathbb{R}^l \to \mathbb{R}^m$, $\rho_\vartheta\colon \mathbb{R}^m \times \mathbb{R} \to \mathbb{R}^m$, and the matrix $\mathrm{d}\gamma\colon [-1, 0] \to \mathbb{R}^{m \times m}$ is defined as

$$\mathrm{d}\gamma(\vartheta) = \mathrm{I}\big(\delta(\vartheta) + \delta(\vartheta + 1)\big)\mathrm{d}\vartheta\,, \tag{2.8}$$

where $\mathrm{I} \in \mathbb{R}^{\mathrm{m} \times \mathrm{m}}$ is the $m \times m$ identity matrix. Here the equilibrium (2.3) is written as

$$x(t) = x_t \equiv c\,. \tag{2.9}$$

The form (2.5) with general functional G is used to construct the general theory of RFDEs as described in [50]. Furthermore, equations (2.2) and (2.5) can be rewritten as an operator differential equation (OpDE)

$$\dot{x}_t = \mathcal{G}(x_t)\,, \tag{2.10}$$

where the nonlinear operator $\mathcal{G}\colon \mathbb{X}_{\mathbb{R}^m} \times \mathbb{R}^l \to \mathbb{X}_{\mathbb{R}^m}$ is defined by

$$\mathcal{G}(\phi)(\vartheta) = \begin{cases} \dfrac{\partial}{\partial \vartheta}\phi(\vartheta)\,, & \text{if} \quad -1 \le \vartheta < 0\,, \\ f(\phi(0), \phi(-1); \eta)\,, & \text{if} \quad \vartheta = 0\,. \end{cases} \tag{2.11}$$

The linearization of this operator is used when investigating the linear stability of equilibrium (2.9) as described in Section 2.2. Note that $\mathcal{G}$ still depends on the parameter η as indicated (only) on the right-hand side of definition (2.11): we adopt this abbreviated notation for the remainder of the thesis. We note also that one may consider only the first row of $\mathcal{G}$ as an operator on a domain in $\mathbb{X}_{\mathbb{R}^m}$ defined by the second row of $\mathcal{G}$; this gives the same mathematical description as shown in [31, 115].

Using the initial function $x_0 = \varphi(\vartheta)\,, \vartheta \in [-1, 0]$, the solution of (2.10) can be written as

$$x_t = \mathcal{T}_t(x_0)\,, \tag{2.12}$$

where the nonlinear operator $\mathcal{T}_t \colon \mathbb{X}_{\mathbb{R}^m} \to \mathbb{X}_{\mathbb{R}^m}$, called the *solution operator* or the *semiflow*, gives the evolution of the state variable $x_t \in \mathbb{X}_{\mathbb{R}^m}$. The linearization of this operator is used to investigate the stability of periodic orbits as shown in Section 2.2.

2.2 Stability and bifurcations

In this section we discuss the stability and bifurcations taking place in system (2.2). First we define the perturbation

$$y(t) = x(t) - c\,, \tag{2.13}$$

around equilibrium (2.3) and consider the linearization of (2.2) as

$$\dot{y}(t) = \tilde{\mathrm{L}}(\eta)\, y(t) + \tilde{\mathrm{R}}(\eta)\, y(t-1)\,, \tag{2.14}$$

where $y \colon \mathbb{R} \to \mathbb{R}^m$ and $\tilde{\mathrm{L}}, \tilde{\mathrm{R}} \colon \mathbb{R}^l \to \mathbb{R}^{m\times m}$ are constant matrices (depending only on the parameter η). By inserting trial solutions in the form $y(t) = C\mathrm{e}^{\lambda t}$, $C \in \mathbb{C}^m, \lambda \in \mathbb{C}$ into (2.14), one obtains the characteristic equation

$$D(\lambda; \eta) = \det\bigl(\lambda \mathrm{I} - \tilde{\mathrm{L}}(\eta) - \tilde{\mathrm{R}}(\eta)\, \mathrm{e}^{-\lambda}\bigr) = 0\,. \tag{2.15}$$

This equation has infinitely many *characteristic exponents* (also called *characteristic roots*) $\lambda \in \mathbb{C}$, which have no accumulation point in $\mathbb{C}$ (because of the fixed delay; see [50]). Furthermore, only a finite number of these characteristic roots are situated in the right-half complex

plane [105]. The linear equation (2.14) can be rewritten as the OpDE

$$\dot{y}_t = \mathcal{L} y_t \,, \tag{2.16}$$

where $y_t \colon \mathbb{R} \to \mathbb{X}_{\mathbb{R}^m}$ is also defined by a shift so that $y_t(\vartheta) = y(t+\vartheta)$, $\vartheta \in [-1, 0]$, and the linear operator $\mathcal{L} \colon \mathbb{X}_{\mathbb{R}^m} \to \mathbb{X}_{\mathbb{R}^m}$ is defined by

$$\mathcal{L}\phi(\vartheta) = \begin{cases} \dfrac{\partial}{\partial \vartheta}\phi(\vartheta) \,, & \text{if} \quad -1 \leq \vartheta < 0 \,, \\ \tilde{\mathrm{L}}(\eta)\phi(0) + \tilde{\mathrm{R}}(\eta)\phi(-1) \,, & \text{if} \quad \vartheta = 0 \,. \end{cases} \tag{2.17}$$

The operator $\mathcal{L}$ provides the same characteristic roots as the characteristic equation (2.15), when its eigenvalues are computed from

$$\mathrm{Ker}(\lambda \mathcal{I} - \mathcal{L}) \neq \{0\} \,. \tag{2.18}$$

Equation (2.16) is the linearization of (2.10) around equilibrium (2.9), because the operator $\mathcal{L}$ (2.17) is the linearization of the operator $\mathcal{G}$ (2.11).

The trivial solution (2.3) of the nonlinear DDE (2.2) is asymptotically stable (that is, stable in the Lyapunov sense as well) for a fixed value of the bifurcation parameter η if all the infinitely many characteristic exponents are situated on the left-hand side of the imaginary axis. Since (2.15) and (2.18) have infinitely many solutions for λ, infinite-dimensional version of *Routh-Hurwitz* criteria are needed to decide on whether the steady state is stable or unstable for a fixed value of the bifurcation parameter η. These kind of criteria can be determined by calculating complex integrals around the characteristic exponents; see [68, 92, 105] for detailed calculations.

Although the technical details are more difficult, the bifurcation theory of ODEs [47, 73] can be extended to DDEs and the same kind of bifurcations of equilibria occur. Now we briefly discuss these bifurcations. We should note that system (1.4),(1.23) possesses a translational symmetry: shifting the position of all vehicles along the ring by an arbitrary distance results in the same system. This gives rise to a zero characteristic exponent, which requires the analysis introduced in Section 3.2.

When varying η, the equilibrium can lose its stability if some of the infinitely many characteristic roots move into the right-hand side of the complex plane. The bifurcation happens when these roots are situated at the imaginary axis for a critical parameter value η_{cr}. A fold bifurcation takes place if (2.15) and (2.18) possess a zero characteristic root at η_{cr}, that is,

$$\lambda_0(\eta_{\mathrm{cr}}) = 0\,. \tag{2.19}$$

In the parameter space $\eta \in \mathbb{R}^l$ the corresponding stability boundaries are $(l-1)$-dimensional hypersurfaces which are described by

$$\operatorname{Re} D(0;\eta_{\mathrm{cr}}) = 0\,, \qquad \operatorname{Im} D(0;\eta_{\mathrm{cr}}) = 0\,. \tag{2.20}$$

Note that in the presence of translational symmetry the zero root may exist for any values of η: this case is not a fold bifurcation and is discussed further in Section 3.2.

Apart from the zero characteristic root (2.19) there is another condition for the existence of a fold bifurcation, namely the critical characteristic exponent has to cross the origin with a non-zero speed as the bifurcation parameter η is varied, that is,

$$\operatorname{Re}\left(\frac{\mathrm{d}\lambda_0(\eta_{\mathrm{cr}})}{\mathrm{d}\eta}\right) = \operatorname{Re}\left(-\frac{\partial D(\lambda_0;\eta_{\mathrm{cr}})}{\partial \eta}\left(\frac{\partial D(\lambda_0;\eta_{\mathrm{cr}})}{\partial \lambda}\right)^{-1}\right) \neq 0\,, \tag{2.21}$$

where the first equality can be verified by implicit differentiation of the characteristic function (2.15). Note that η is usually varied so that only one of its components is changed and its other $(l-1)$ components are kept fixed.

A Hopf bifurcation may occur at the critical parameter value η_{cr} if there exists a complex conjugate pair of purely imaginary characteristic exponents

$$\lambda_{1,2}(\eta_{\mathrm{cr}}) = \pm \mathrm{i}\omega\,, \quad \omega \in \mathbb{R}^+\,. \tag{2.22}$$

At this bifurcation periodic oscillations appear or disappear around the equilibrium. In this case the corresponding stability boundaries ($(l-1)$-dimensional hypersurfaces) are described by

$$R(\omega) = \operatorname{Re} D(\mathrm{i}\omega;\eta_{\mathrm{cr}}) = 0\,, \qquad S(\omega) = \operatorname{Im} D(\mathrm{i}\omega;\eta_{\mathrm{cr}}) = 0\,, \tag{2.23}$$

which are parameterised by the frequency $\omega \in \mathbb{R}^+$.

Again, apart from the purely imaginary characteristic roots (2.22) there is another condition for the existence of a Hopf bifurcation, namely the critical characteristic exponents have to cross the imaginary axis with a non-zero speed as the bifurcation parameter η is varied, that is,

$$\mathrm{Re}\left(\frac{\mathrm{d}\lambda_{1,2}(\eta_{\mathrm{cr}})}{\mathrm{d}\eta}\right) = \mathrm{Re}\left(-\frac{\partial D(\lambda_{1,2};\eta_{\mathrm{cr}})}{\partial \eta}\left(\frac{\partial D(\lambda_{1,2};\eta_{\mathrm{cr}})}{\partial \lambda}\right)^{-1}\right) \neq 0 \tag{2.24}$$

has to be satisfied.

In the same way as for ODEs [47, 73], the above bifurcations can occur together in DDEs when their hypersurfaces intersect each other in the parameter space. In the case when a zero exponent and a pair of purely imaginary exponents co-exist at η_{cr}, then a fold bifurcation occurs together with a Hopf bifurcation, as was found by Sieber & Krauskopf [102] in an unfolding of a degenerate case of a controlled inverted pendulum. The intersection of a fold hypersurface and a Hopf hypersurface locates this bifurcation in the parameter space. When not only one but two pairs of purely imaginary characteristic exponents $\pm\mathrm{i}\omega_1$ and $\pm\mathrm{i}\omega_2$ co-exist at η_{cr} (with two different frequencies $\omega_1 \in \mathbb{R}^+$ and $\omega_2 \in \mathbb{R}^+$), then a co-dimension two double Hopf bifurcation occurs as was demonstrated by Stépán & Haller [106] for robot dynamics and by Green *et al.* [45] in laser systems. Due to this bifurcation quasi-periodic oscillations appear around the equilibrium. The intersection of two Hopf hypersurfaces shows where this bifurcation takes place in the parameter space. Note that phase-locking happens on the torus of quasi-periodic oscillations (i.e., the oscillations become periodic) when the two frequencies ω_1 and ω_2 are rationally related. This can be expressed by $n_1\omega_1 = n_2\omega_2$ for $n_1, n_2 \in \mathbb{N}^+$, $n_1 > n_2$. Note also that strong resonances occur in the cases $n_1/n_2 = 1, 2, 3, 4$.

It is also possible to investigate the system around a periodic solution

$$x(t) = x_{\mathrm{p}}(t) = x_{\mathrm{p}}(t + T_{\mathrm{p}})\,, \tag{2.25}$$

with period $T_{\mathrm{p}} \in \mathbb{R}^+$. If the periodic orbit is born in a Hopf bifurcation then close to the bifurcation point the period T_{p} can be approximated as $T_{\mathrm{p}} \simeq 2\pi/\omega$, where ω is the frequency given by (2.22).

By defining the perturbation

$$z(t) = x(t) - x_{\mathrm{p}}(t)\,, \tag{2.26}$$

around the periodic solution (2.25), the linearization of (2.2) can be written as

$$\dot{z}(t) = \mathrm{L}_{\mathrm{p}}(t;\eta)\, z(t) + \mathrm{R}_{\mathrm{p}}(t;\eta)\, z(t-1)\,, \tag{2.27}$$

where the matrix functions $\mathrm{L}_{\mathrm{p}}, \mathrm{R}_{\mathrm{p}} \colon \mathbb{R} \times \mathbb{R}^l \to \mathbb{R}^{m\times m}$ are periodic in time so that $\mathrm{L}_{\mathrm{p}}(t;\eta) = \mathrm{L}_{\mathrm{p}}(t+T_{\mathrm{p}};\eta)$, $\mathrm{R}_{\mathrm{p}}(t;\eta) = \mathrm{R}_{\mathrm{p}}(t+T_{\mathrm{p}};\eta)$. Note that the period $T_{\mathrm{p}} = T_{\mathrm{p}}(\eta)$ itself also depends on the parameters. By using the notation $z_t(\vartheta) = z(t+\vartheta)$, $\vartheta \in [-1,0]$ again, and considering an initial condition $z_0 = \varphi(\vartheta)$ the solution of (2.27) is given by

$$z_t = \mathcal{U}_t z_0\,, \tag{2.28}$$

where $\mathcal{U}_t \colon \mathbb{X}_{\mathbb{R}^n} \to \mathbb{X}_{\mathbb{R}^n}$ is the semiflow. Equation (2.28) is the linearization of (2.12) around the periodic orbit (2.25) because the operator $\mathcal{U}_t$ is the linearization of the operator $\mathcal{T}_t$.

The operator $\mathcal{U}_{T_{\mathrm{p}}}$ is called the *monodromy operator*. Its infinitely many eigenvalues are called the *Floquet multipliers* and they are defined by

$$\mathrm{Ker}(\mu\mathcal{I} - \mathcal{U}_{T_{\mathrm{p}}}) \neq \{0\}\,. \tag{2.29}$$

It can be shown that $\mathcal{U}_{T_{\mathrm{p}}}$ is a compact operator and, hence, the only accumulation point of the infinitely many Floquet multipliers is the origin [50]. Note that there is always a *trivial Floquet multiplier* at 1 which corresponds to a shift along the periodic orbit. Further note that $\mathcal{U}_{T_{\mathrm{p}}}$ cannot be written in closed form, but can only be tackled numerically by semi-discretization [59] or by full discretization [35, 60].

The periodic solution (2.25) is stable when all the infinitely many Floquet multipliers μ (except the trivial one) are situated inside unit circle on the complex plane. In a similar way as for ODEs [47, 73], the periodic solution can lose its stability thought different bifurcations when the parameter takes a critical value η_{cr}. A fold (saddle-node) bifurcation of the periodic solution happens when a (non-trivial) Floquet multiplier satisfies

$$\mu_0(\eta_{\mathrm{cr}}) = 1\,, \tag{2.30}$$

i.e., crosses the unit circle at 1. A torus (Neimark-Sacker) bifurcation of the periodic motion takes place when a pair of complex conjugate multipliers

$$\mu_{1,2}(\eta_{\rm cr}) = \mathrm{e}^{\pm \mathrm{i}\chi}\,, \quad \chi \in (0,\pi)\,, \tag{2.31}$$

crosses the unit circle. This bifurcation yields quasi-periodic oscillations with frequencies $\chi/T_{\rm p}$ and $2\pi/T_{\rm p}$. Note that phase-locking occurs on the bifurcating torus (that is, the oscillations become periodic) when these frequencies are rationally related. In this case we have $n_1\chi = n_2 2\pi$ for $n_1, n_2 \in \mathbb{N}^+$, $n_1 > 2n_2$. Note also that strong resonances take place in the cases $n_1/n_2 = 3, 4$. Finally, a period doubling bifurcation occurs for a Floquet multiplier

$$\mu_3(\eta_{\rm cr}) = -1\,. \tag{2.32}$$

We remark that the above bifurcations take place in $(l-1)$-dimensional hypersurfaces of the parameter space and they can coincide in co-dimension two bifurcations when these hypersurfaces intersect each other, yielding even more complicated motions in their neighbourhood.

2.3 Hopf bifurcation calculation: weak nonlinearities

In this section we show how a Hopf bifurcation can be analysed analytically, giving the first Fourier approximation of stable or unstable periodic solutions as a function of the bifurcation parameters. However, this approach is only weakly nonlinear and is acceptable only for parameters close enough to the bifurcation point, since it uses a third order Taylor series expansion of the DDE's nonlinearity. These analytical normal from calculations are very complicated, particularly in systems where a centre manifold reduction is required. However, in some cases it is possible to use computer algebra packages to simplify the matter; see, e.g., Campbell & Bélair [21].

This approximate analytical approach is useful in many applications, especially when the bifurcating periodic solutions are unstable, i.e., when the Hopf bifurcation is subcritical. Analytical studies of Hopf bifurcations in delayed systems are carried out, for example, on

machine tool vibrations by Kalmár-Nagy *et al.* [61] and on voltage oscillations of neuron systems by Shayer & Campbell [100].

The conditions (2.22) and (2.24) can be checked using the variational systems (2.14) and (2.16). However, the super- or subcritical nature of the Hopf bifurcation, i.e., the stability and estimated amplitudes of the periodic solutions arising about the stable or unstable equilibrium (2.3),(2.9) can be determined only by the investigation of the third degree power series of the original nonlinear systems (2.2) and (2.10).

Let us consider the third order approximation of the nonlinear system (2.2) around the equilibrium (2.3) in the form

$$\dot{y}(t) = \tilde{\mathrm{L}}(\eta)\, y(t) + \tilde{\mathrm{R}}(\eta)\, y(t-1) + \tilde{F}(y(t), y(t-1); \eta)\,, \tag{2.33}$$

where $\tilde{\mathrm{L}}, \tilde{\mathrm{R}} \colon \mathbb{R}^l \to \mathbb{R}^{m\times m}$ are the matrices already shown in (2.14), and $\tilde{F} \colon \mathbb{R}^m \times \mathbb{R}^m \times \mathbb{R}^l \to \mathbb{R}^m$ is an analytic function with the near-zero feature $\tilde{F}(0, 0; \eta) = 0$, which contains the second and third order terms.

As mentioned above, we suppose that the necessary conditions (2.22) and (2.24) of Hopf bifurcation are also fulfilled, that is, there exists a critical parameter η_{cr} such that

$$\lambda_{1,2}(\eta_{\mathrm{cr}}) = \pm \mathrm{i}\omega\,, \quad \mathrm{Re}\left(\frac{\mathrm{d}\lambda_{1,2}(\eta_{\mathrm{cr}})}{\mathrm{d}\eta}\right) \neq 0\,. \tag{2.34}$$

By considering (2.33) at the critical parameter η_{cr}, we may obtain

$$\dot{y}(t) = \mathrm{L}y(t) + \mathrm{R}y(t-1) + F(y(t), y(t-1))\,, \tag{2.35}$$

where the matrices $\mathrm{L}, \mathrm{R} \in \mathbb{R}^{m\times m}$, and the nonlinear function $F \colon \mathbb{R}^m \times \mathbb{R}^m \to \mathbb{R}^m$ are given by

$$\mathrm{L} = \tilde{\mathrm{L}}(\eta_{\mathrm{cr}})\,, \quad \mathrm{R} = \tilde{\mathrm{R}}(\eta_{\mathrm{cr}})\,, \quad \text{and} \quad F(y(t), y(t-1)) = \tilde{F}(y(t), y(t-1); \eta_{\mathrm{cr}})\,, \tag{2.36}$$

preserving the near-zero feature according to $F(0, 0) = 0$. The DDE (2.35) can also be rewritten in operator differential equation (OpDE) form

$$\dot{x}_t = \mathcal{A}x_t + \mathcal{F}(x_t)\,, \tag{2.37}$$

where the linear and nonlinear operators $\mathcal{A}$, $\mathcal{F}\colon \mathbb{X}_{\mathbb{R}^m} \to \mathbb{X}_{\mathbb{R}^m}$ are defined as

$$\mathcal{A}\phi(\vartheta) = \begin{cases} \dfrac{\partial}{\partial\vartheta}\phi(\vartheta)\,, & \text{if} \quad -1 \le \vartheta < 0\,, \\ \mathrm{L}\phi(0) + \mathrm{R}\phi(-1)\,, & \text{if} \quad \vartheta = 0\,, \end{cases} \tag{2.38}$$

$$\mathcal{F}(\phi)(\vartheta) = \begin{cases} 0\,, & \text{if} \quad -1 \le \vartheta < 0\,, \\ F(\phi(0), \phi(-1))\,, & \text{if} \quad \vartheta = 0\,. \end{cases} \tag{2.39}$$

Indeed (2.37) is the third order approximation of (2.10) around the equilibrium (2.9) at η_{cr}, so that the operator $\mathcal{A}$ contains the linear and the operator $\mathcal{F}$ contains the nonlinear part of the operator $\mathcal{G}$ (2.11). Furthermore, comparing (2.17) and (2.38) one can see that $\mathcal{A} = \mathcal{L}(\eta_{\mathrm{cr}})$.

We now briefly discuss the algorithm of Hopf bifurcation calculation for the OpDE (2.37), when the system does not possess any special symmetry. More technical detail can be found in [84]. The case with an additional translational symmetry (an original result of this thesis) is presented in Section 3.2 with all the technical details.

Due to the Hopf bifurcation the two eigendirections of the equilibrium (2.3),(2.9) belonging to the characteristic roots (2.34) become unstable. In order to analyse the bifurcation we need to project the system onto the plane spanned by these two directions and onto its complementary space.

The real and imaginary parts $s_1, s_2 \in \mathbb{X}_{\mathbb{R}^m}$ of the eigenvector of the linear operator $\mathcal{A}$, which belongs to the critical eigenvalue $\lambda_1 = \mathrm{i}\omega$, can be determined by

$$\mathcal{A}(s_1 + \mathrm{i}s_2) = \lambda_1(s_1 + \mathrm{i}s_2) \quad \Rightarrow \quad \mathcal{A}s_1 = -\omega s_2\,, \quad \mathcal{A}s_2 = \omega s_1\,. \tag{2.40}$$

In order to project the system onto the plane spanned by s_1 and s_2, and onto its complementary space, we also need to determine the the real and imaginary parts $n_1, n_2 \in \mathbb{X}^*_{\mathbb{R}^m}$ of eigenvectors of the adjoint operator $\mathcal{A}^*$ associated with $\lambda_1^* = -\mathrm{i}\omega$. These are given by

$$\mathcal{A}^*(n_1 + \mathrm{i}n_2) = \lambda_1^*(n_1 + \mathrm{i}n_2) \quad \Rightarrow \quad \mathcal{A}^*n_1 = \omega n_2\,, \quad \mathcal{A}^*n_2 = -\omega n_1\,. \tag{2.41}$$

where the adjoint operator is defined by

$$\mathcal{A}^*\psi(\sigma) = \begin{cases} -\dfrac{\partial}{\partial\sigma}\psi(\sigma)\,, & \text{if} \quad 0 < \sigma \leq 1\,, \\ \mathrm{L}^*\psi(0) + \mathrm{R}^*\psi(1)\,, & \text{if} \quad \sigma = 0\,, \end{cases} \tag{2.42}$$

where $*$ denotes either adjoint operator or transposed conjugate vector and matrix.

These vectors also have to satisfy the orthonormality conditions

$$\langle n_1, s_1\rangle = 1\,, \quad \langle n_1, s_2\rangle = 0\,, \tag{2.43}$$

where the inner product is calculated by

$$\langle \psi, \phi\rangle = \psi^*(0)\phi(0) + \int_{-1}^{0} \psi^*(\xi+1)\mathrm{R}\phi(\xi)\mathrm{d}\xi\,. \tag{2.44}$$

With the help of the right and left eigenvectors s_1, s_2 and n_1, n_2 of operator $\mathcal{A}$, we are able to introduce the new state variables

$$\begin{cases} z_1 = \langle n_1, y_t\rangle\,, \\ z_2 = \langle n_2, y_t\rangle\,, \\ w = y_t - z_1 s_1 - z_2 s_2\,, \end{cases} \tag{2.45}$$

where $z_1, z_2 \colon \mathbb{R} \to \mathbb{R}$ and $w \colon \mathbb{R} \to \mathbb{X}_{\mathbb{R}^m}$. Using the eigenvectors given by (2.40) and (2.41), and the inner product definition (2.44), the OpDE (2.37) can be rewritten with the new variables (2.45) as

$$\begin{aligned} \begin{bmatrix} \dot{z}_1 \\ \dot{z}_2 \\ \dot{w} \end{bmatrix} &= \begin{bmatrix} 0 & \omega & \mathcal{O} \\ -\omega & 0 & \mathcal{O} \\ 0 & 0 & \mathcal{A} \end{bmatrix} \begin{bmatrix} z_1 \\ z_2 \\ w \end{bmatrix} \\ &\quad + \begin{bmatrix} n_1^*(0)\mathcal{F}(z_1 s_1 + z_2 s_2 + w)(0) \\ n_2^*(0)\mathcal{F}(z_1 s_1 + z_2 s_2 + w)(0) \\ -\sum_{j=1,2} n_j^*(0)\mathcal{F}(z_1 s_1 + z_2 s_2 + w)(0) s_j + \mathcal{F}(z_1 s_1 + z_2 s_2 + w) \end{bmatrix}. \end{aligned} \tag{2.46}$$

It shows the structure of OpDE (2.37) after projection onto the plane spanned by s_1 and s_2, and onto its complementary space. Note that the first two equations still contain the variable w.

The plane spanned by the eigenvectors s_1 and s_2 is tangent to the centre manifold at the origin. This means, that the centre manifold can be approximated locally as a truncated power series of w depending on the second order of the co-ordinates z_1 and z_2 as

$$w(\vartheta) = \frac{1}{2}\left(h_{20}(\vartheta)z_1^2 + 2h_{11}(\vartheta)z_1z_2 + h_{02}(\vartheta)z_2^2\right) . \tag{2.47}$$

The unknown coefficients $h_{20}, h_{11}, h_{02} \in \mathbb{X}_{\mathbb{R}^m}$ can be determined by calculating the derivative of w and substituting into the third equation of (2.46). The resulting w can be substituted into the first two equations of (2.46), thus these two equations lead to ODEs with right-hand sides containing only the variables z_1 and z_2. These equations describe the flow restricted to the two-dimensional centre manifold.

The so-called Poincaré-Lyapunov coefficient Δ can be determined by the Bautin formula as shown in [47, 105], which shows the (super- or subcritical) type of the bifurcation and approximate amplitude of the periodic solution. The Hopf bifurcation is supercritical (subcritical) if $\Delta < 0$ ($\Delta > 0$), and the amplitude of the stable (unstable) oscillations is expressed by

$$A = \sqrt{-\frac{1}{\Delta}\mathrm{Re}\left(\frac{\mathrm{d}\lambda_{1,2}(\eta_{\mathrm{cr}})}{\mathrm{d}\eta}\right)(\eta - \eta_{\mathrm{cr}})} . \tag{2.48}$$

As mentioned above we consider the variation of η through its chosen (scalar) component. In the cases of super- and subcritical bifurcations not only the sign of Δ changes but also the sign of $(\eta - \eta_{\mathrm{cr}})$. Thus, in the case of supercritical bifurcation a branch of stable oscillations appears 'above' the unstable part of the branch of equilibria, while when the bifurcation is subcritical a branch of unstable oscillations exists 'above' the stable part of the branch of equilibria. The first Fourier term of the oscillations on the centre manifold is given by

$$\begin{bmatrix} z_1(t) \\ z_2(t) \end{bmatrix} = A \begin{bmatrix} \cos(\omega t) \\ -\sin(\omega t) \end{bmatrix} . \tag{2.49}$$

Since $y(t) = y_t(0)$ by definition, and close to the critical bifurcation parameter η_{cr} we have $y_t(\vartheta) \approx z_1(t)s_1(\vartheta) + z_2(t)s_2(\vartheta)$, the formula (2.49) for periodic solutions yields

$$y(t) \approx z_1(t)s_1(0) + z_2(t)s_2(0) = A\big(s_1(0)\cos(\omega t) - s_2(0)\sin(\omega t)\big) . \tag{2.50}$$

The nonlinear oscillations around the equilibrium (2.3),(2.9) are well approximated with these harmonic oscillations when $|\eta - \eta_{\rm cr}|$ is sufficiently small.

2.4 Numerical continuation: strong nonlinearities

Our principal tool in Chapters 4 and 5 is the numerical continuation package DDE-BIFTOOL [35, 36] which is able to follow branches of equilibria and periodic solutions of DDEs as parameters are changed, similarly to the package AUTO [32] for ODEs. Stability information is computed along solution branches. Co-dimension one bifurcation points, where the stability of solutions changes, are detected automatically. In particular, we may follow the branches of periodic solutions that are born at Hopf bifurcations and detect subsequent secondary bifurcations such as fold (saddle-node) bifurcations. Furthermore, the Floquet multipliers and the corresponding eigendirections are available from DDE-BIFTOOL. This allows us to identify characteristic time scales of repulsion when the solutions are unstable.

To avoid the singularities caused by translational symmetry of system (1.6),(1.23) we use (1.15) and define

$$h_n(t) = L - \sum_{i=1}^{n-1} h_i(t)\,, \tag{2.51}$$

reducing the number of equations to $2n-1$. (Note that the problem of symmetry is handled in a different way in Section 3.2.)

At first we fix $(l-1)$ of the l parameters contained by $\eta \in \mathbb{R}^l$ and vary the remaining one. Substituting the equilibrium (2.3) into (2.2) we obtain the algebraic equation (2.4) which can be solved numerically for a chosen parameter η by using, e.g., the Newton-Raphson method. Then this result can be used as an initial approximation when solving the same algebraic equation for the slightly changed parameter $\eta + {\rm d}\eta$. By continuing this process, a branch of equilibria is obtained as a function of the bifurcation parameter. Problems may occur when the branch folds back, and arclength parametrization of the curve is used in DDE-BIFTOOL to avoid this problem. In order to determine the stability of equilibria,

the operator $\mathcal{L}$ (2.17), that is, the eigenvalue problem (2.18), needs to be discretised and the eigenvalues of the resulting (large-sized) matrix have to be computed. DDE-BIFTOOL computes these eigenvalues and detects fold and Hopf bifurcations of equilibria when a real or a pair of complex conjugated characteristic exponents crosses the imaginary axis as discussed in Section 2.1. The corresponding eigenvectors, e.g., s_1 and s_2 in (2.40) for the critical eigenvalue $\lambda_1 = \mathrm{i}\omega$, can also be computed numerically. They are necessary for starting data when one continues branches bifurcating from the bifurcation points, e.g., branches of periodic solutions as discussed below.

It is also possible to fix only $l-2$ parameters and vary the remaining two. Thus the corresponding intersection of a stability boundary ($(l-1)$-dimensional hypersurface) and the plane of the two non-fixed parameters is a curve. Applying the condition of the bifurcation taking place on the boundary (zero root (2.19) for fold bifurcation and purely imaginary roots (2.22) for Hopf bifurcation), DDE-BIFTOOL is able to follow the corresponding curves. This two-parameter continuation gives a discretized representation of the boundaries (2.20) and (2.23).

When the periodic solution (2.25) is considered the differential equation (2.2) has to be solved. In order to do this, the periodic solution is represented by a number of mesh points, with a (small) number of so-called collocation points in between them. On each mesh interval the solution is represented by a polynomial, and the number of collocation points defines its degree [34]. Thus, the DDE (2.2) with condition (2.25) leads to algebraic equations. Hence, in a way similar to the continuation of equilibria, the branch of periodic solutions can be continued using pseudo arclength continuation. Note that the oscillations computed by continuation is well approximated by (2.50) in the vicinity a Hopf bifurcation point of equilibria. In order to determine the stability of periodic solutions, the operator $\mathcal{U}_{T_\mathrm{p}}$ defined by (2.28), that is, the eigenvalue problem (2.29), needs to be discretised and the eigenvalues of the resulting (large-sized) matrix have to be computed. By computing these eigenvalues, fold and period doubling bifurcations of the periodic solutions can be detected when real Floquet multipliers cross the unit circle at 1 and -1, respectively. Torus bifurcations may

also be found by detecting when a pair of complex conjugated Floquet multipliers crosses the unit circle. These bifurcations were discussed in Section 2.1. The eigendirections belonging to these multipliers are also available from DDE-BIFTOOL, which can give an indication how the repelling/attracting dynamics change along the periodic orbit.

We note that it is not possible at present to perform two-parameter continuation of bifurcations of periodic orbits with DDE-BIFTOOL, i.e., to determine curves where fold, torus, or period doubling bifurcation takes place. However, the package PDDE-CONT has recently been developed by Szalai [108, 109], which is able to follow the boundaries of fold and period doubling bifurcations in autonomous systems described by (2.2) and also in periodically forced delayed systems.

Overall, DDE-BIFTOOL performs similar functions for DDE systems that the well known package AUTO [32] performs for ODE systems. In general, the application of continuation packages such as AUTO and DDE-BIFTOOL is a much more efficient way of exploring parameter space than performing mass ensemble simulation of the initial value problem.

Chapter 3

Local stability analysis

The goal of this chapter is the local stability analysis of the DDE model (1.23) about the uniform flow equilibrium (1.16),(1.18). This includes a linear stability analysis of system (1.4),(1.23) and the detection of Hopf bifurcations in the neighbourhood of which there are small amplitude oscillating solutions. We also present a weakly nonlinear analysis which examines the criticality of the Hopf bifurcations, that is, the stability of the small amplitude oscillations.

Bando *et al.* [14, 15] and many subsequent papers have explained traffic jam formation in terms of the loss of linear stability of the uniform flow equilibrium (1.16),(1.18) to oscillations. The weakly nonlinear analysis presented here shows that the Hopf bifurcations are generally subcritical, that is, the oscillations appearing in the vicinity of the Hopf bifurcation points are unstable. In Chapter 4 we show that the branches of unstable oscillations usually undergo fold bifurcations which give the co-existence of stable periodic solutions with stable equilibria. Thus, put together, our analysis shows that the linear instability of the uniform flow is not necessary for traffic jam formation.

The linear stability analysis is presented in Section 3.1 where it is shown how the developing oscillations lead to wave formations propagating in the opposite direction to the vehicle flow. In Section 3.2 we develop a general theory extending standard normal form calcula-

tions [21, 51, 84, 104, 105] of DDEs with a single time delay to a situation when translational symmetry is included in the system. Finally, in Section 3.3 we apply this general theory to the car-following model (1.23). This is a very complicated calculation which motivates the numerical bifurcation analysis presented in Chapter 4. The material presented in this chapter was published in the articles [85, 86, 87].

3.1 Linear stability analysis

Here we perform a linear stability analysis of the DDE system (1.4),(1.23) following the methodology of Section 2.2. The details of the analysis are presented in Section 3.1.1, and are summarised in the form of two-dimensional stability diagrams in Section 3.1.2.

3.1.1 Determination of Hopf bifurcation curves

Let us define the perturbed solution of (1.4),(1.23) about the equilibrium (1.16),(1.18) as

$$x_i^{\mathrm{p}}(t) \colon = x_i(t) - (v^* t + x_i^*)\,, \quad v_i^{\mathrm{p}}(t) \colon = v_i(t) - v^*\,, \quad h_i^{\mathrm{p}}(t) \colon = h_i(t) - h^*\,, \quad i = 1, \ldots, n\,, \tag{3.1}$$

so that

$$h_i^{\mathrm{p}}(t) = x_{i+1}^{\mathrm{p}}(t) - x_i^{\mathrm{p}}(t)\,, \quad i = 1, \ldots, n\,. \tag{3.2}$$

Note that $v^* = \mathrm{V}(h^*)$ is defined by (1.17). Linearizing $\mathrm{V}(h)$ around $h = h^*$ (1.23) gives the differential equations

$$\dot{v}_i^{\mathrm{p}}(t) = -\alpha\, v_i^{\mathrm{p}}(t) + \alpha \mathrm{V}'(h^*)\big(x_{i+1}^{\mathrm{p}}(t-1) - x_i^{\mathrm{p}}(t-1)\big)\,, \quad i = 1, \ldots, n\,. \tag{3.3}$$

In (3.2) and (3.3) we model the circular road by identifying the $(n+1)$-st vehicle with the first one, i.e., $x_{n+1}^{\mathrm{p}}(t) = x_1^{\mathrm{p}}(t)$, $v_{n+1}^{\mathrm{p}}(t) = v_1^{\mathrm{p}}(t)$, and $h_{n+1}^{\mathrm{p}}(t) = h_1^{\mathrm{p}}(t)$. In addition, the kinematic condition (1.4) can be written in the form

$$v_i^{\mathrm{p}}(t) = \dot{x}_i^{\mathrm{p}}(t)\,, \quad i = 1, \ldots, n\,. \tag{3.4}$$

We now substitute the trial solution

$$v_i^{\mathrm{p}}(t) = P_i \mathrm{e}^{\lambda t}\,, \quad x_i^{\mathrm{p}}(t) = P_{n+i}\mathrm{e}^{\lambda t}\,, \quad i = 1, \ldots, n\,, \tag{3.5}$$

into system (3.3),(3.4), where $\lambda, P_i \in \mathbb{C}$. Thus we obtain the linear homogeneous equation

$$\Delta\left(\lambda; \alpha, \mathrm{V}'(h^*)\right) \begin{bmatrix} P_1 \\ \vdots \\ P_{2n} \end{bmatrix} = \begin{bmatrix} (\lambda+\alpha)\mathrm{I} & \alpha \mathrm{V}'(h^*)\mathrm{e}^{-\lambda}\mathrm{A} \\ -\mathrm{I} & \lambda \mathrm{I} \end{bmatrix} \begin{bmatrix} P_1 \\ \vdots \\ P_{2n} \end{bmatrix} = 0\,, \tag{3.6}$$

where $\Delta \in \mathbb{C}^{2n} \times \mathbb{C}^{2n}$, $\mathrm{I} \in \mathbb{R}^{n\times n}$ is the $n \times n$ identity matrix, and the matrix $\mathrm{A} \in \mathbb{R}^{n\times n}$ is given by

$$\mathrm{A} = \begin{bmatrix} \ddots & \ddots & & \\ & 1 & -1 & \\ & & \ddots & \ddots \\ -1 & & & \ddots \end{bmatrix}. \tag{3.7}$$

The characteristic equation is given by

$$D\left(\lambda; \alpha, \mathrm{V}'(h^*)\right) = \det \Delta\left(\lambda; \alpha, \mathrm{V}'(h^*)\right) = \left(\lambda^2 + \alpha\lambda + \alpha \mathrm{V}'(h^*)\mathrm{e}^{-\lambda}\right)^n - \left(\alpha \mathrm{V}'(h^*)\mathrm{e}^{-\lambda}\right)^n = 0\,. \tag{3.8}$$

At a bifurcation point defined by $h^* = h^*_{\mathrm{cr}}$, Hopf bifurcations may occur when there exists a complex conjugate pair of purely imaginary characteristic exponents

$$\lambda_{1,2}(h^*_{\mathrm{cr}}) = \pm \mathrm{i}\omega\,, \quad \omega \in \mathbb{R}^+\,, \tag{3.9}$$

which satisfies (3.8). To find the Hopf boundaries in the parameter space we substitute the critical eigenvalue $\lambda_1 = \mathrm{i}\omega$ into (3.8), and after taking real and imaginary parts, and some further calculation, we find that

$$\begin{aligned} \mathrm{V}'(h^*_{\mathrm{cr}}) &= \frac{\omega}{2\,\cos(\omega - \frac{k\pi}{n})\,\sin(\frac{k\pi}{n})}\,, \\ \alpha &= -\omega\,\cot(\omega - \tfrac{k\pi}{n})\,, \end{aligned} \tag{3.10}$$

where $k = 1, \ldots, n-1$ is introduced by taking the nth root of unity. Equation (3.10) can also be written in the form

$$\begin{aligned} \cos\omega &= \frac{\omega}{2\mathrm{V}'(h^*_{\mathrm{cr}})}\left(\frac{\omega}{\alpha} + \cot(\tfrac{k\pi}{n})\right), \\ \sin\omega &= \frac{\omega}{2\mathrm{V}'(h^*_{\mathrm{cr}})}\left(1 - \frac{\omega}{\alpha}\cot(\tfrac{k\pi}{n})\right), \end{aligned} \tag{3.11}$$

which yields

$$\frac{4\mathrm{V}'(h^*_{\mathrm{cr}})^2}{\omega^2}\sin^2(\tfrac{k\pi}{n}) = 1 + \frac{\omega^2}{\alpha^2}\,. \tag{3.12}$$

By substituting (3.11) into (3.6), we may find the eigenvector components

$$P_i = \mathrm{e}^{\mathrm{i}\frac{2\pi k}{n}i}\,, \quad P_{n+i} = \frac{1}{\mathrm{i}\omega}\,\mathrm{e}^{\mathrm{i}\frac{2\pi k}{n}i}\,, \quad i = 1, \ldots, n\,, \tag{3.13}$$

where i is the imaginary unit. This shows that k is the discrete spatial wave number of oscillations along the ring. The effects of (3.13) on the infinite dimensional dynamics are described in Section 3.3. Note that we have omitted the discussion of the $k = 0$ (spatially independent) mode, since it violates the constraint

$$\sum_{i=1}^{n} h_i^{\mathrm{p}}(t) = \sum_{i=1}^{n}\left(x_{i+1}^{\mathrm{p}}(t) - x_i^{\mathrm{p}}(t)\right) = 0\,, \tag{3.14}$$

implied by (1.15).

By using (3.5) and (3.13) and taking the real part, the perturbation can be written as

$$v_i^{\mathrm{p}}(t) = v_{\mathrm{amp}}\cos\left(\tfrac{2\pi k}{n}i + \omega t\right), \quad i = 1, \ldots, n\,, \tag{3.15}$$

where the amplitude v_{amp} is determined by the nonlinear terms as shown in Section 3.3. This perturbation mode corresponds to a wave travelling upstream (opposite to the car flow) with spatial wave number k (i.e., with spatial wavelength $L/k = h^*n/k$), and with frequency ω. Thus the related wave speed is

$$c^{\mathrm{p}}_{\mathrm{wave}} = -\tfrac{n}{2k\pi}h^*\omega < 0\,. \tag{3.16}$$

Using (3.12) and (3.16), and assuming that $\frac{k}{n} \ll 1$, we obtain

$$c^{\mathrm{p}}_{\mathrm{wave}} = -h^*\mathrm{V}'(h^*_{\mathrm{cr}})\Big(1 - \mathcal{O}\big(\tfrac{k\pi}{n}\big)^2\Big)\,. \tag{3.17}$$

Since this motion is a perturbation relative to the equilibrium (1.16),(1.18) where vehicles travel downstream with speed $v^* = \mathrm{V}(h^*)$, the speed of the wave relative to the absolute spatial coordinate is given by

$$\begin{aligned} c_{\text{wave}} = v^* + c^{\text{p}}_{\text{wave}} &= \mathrm{V}(h^*) - h^*\mathrm{V}'(h^*_{\text{cr}})\Big(1 - \mathcal{O}\big(\tfrac{k\pi}{n}\big)^2\Big) \\ &\simeq \mathrm{V}(h^*) - h^*\mathrm{V}'(h^*_{\text{cr}})\,. \end{aligned} \tag{3.18}$$

By considering the optimal velocity function (1.24), we obtain $c_{\text{wave}} < 0$, that is, the resulting wave propagates in the opposite direction to the flow of vehicles. Note that the non-delayed model introduced in [15] exhibits the same wave speed apart from some differences in the coefficient of the correction term $\mathcal{O}\big(\frac{k\pi}{n}\big)^2$. Furthermore, this small-amplitude wave speed is consistent with that predicted by the Lighthill-Whitham continuum theory of highway traffic; see [76, 118].

Now, note that if (ω, k) solves (3.10), then so does $(-\omega, n-k)$. Here we chose to work with $\omega > 0$ and the full set of $k = 1, \ldots, n-1$. Alternatively, one could work with general $\omega \in \mathbb{R}$ and restrict attention to $k = 1, \ldots, n/2$ (even n) or $k = 1, \ldots, (n-1)/2$ (odd n). However, as can be seen below, even when considering $\omega > 0$ only the wave numbers $k \leq n/2$ are significant.

Equations (3.10) describe branches of curves in the $(\mathrm{V}'(h^*), \alpha)$ parameter plane, which are parametrised by the frequency ω. Since we require $\omega, \alpha, \mathrm{V}'(h^*) > 0$, for each k, we find a sequence of feasible intervals

$$\omega \in \left(-\frac{\pi}{2} + \frac{k\pi}{n} + 2l\pi,\ \frac{k\pi}{n} + 2l\pi\right) \cap \mathbb{R}^+,\ l = 0, 1, 2, \ldots\,, \tag{3.19}$$

each of which traces out a different stability curve. Hence, we have a two-parameter family of stability curves described by $k = 1, \ldots, n-1$ and $l = 0, 1, 2, \ldots$.

We now consider the left-most branch of curves in the $(\mathrm{V}'(h^*), \alpha)$ plane which belongs to $l = 0$. It turns out that this branch is responsible for the loss of stability of equilibrium (1.16),(1.18). Each curve belongs to a particular wave number k and is parameterised by the frequency $\omega \in (0, k\pi/n)$. However, we are only interested in the curves for $k \leq n/2$ because those for $k > n/2$ correspond to conjugated waves, i.e., to the same spatial patterns. When

n is even, the Hopf bifurcation curve for $k = n/2$ starts ($\omega = 0$) from the point $(1/2, 0)$ but all other Hopf bifurcation curves, for n even or odd and for any k, start from the origin. Further, all curves converge to the vertical asymptotes

$$\mathrm{V}'(h^*) = \frac{k\pi/n}{2\sin(k\pi/n)}\,, \tag{3.20}$$

when $\omega \to k\pi/n$; see already Figs. 3.1(a) and 3.2(a). This means that the curves are ordered from left to right as k increases. When $n \to \infty$, the first asymptote for $k = 1$ converges to $\mathrm{V}'(h^*) = 1/2$, while the last asymptote for $k = n/2$ or $k = (n-1)/2$ converges to $\mathrm{V}'(h^*) = \pi/4$. Further, the $k > 1$ curves accumulate on the $k = 1$ curve when $n \to \infty$. Using the stability criteria presented in [105], one may show that the stability boundary for the equilibrium is the first (i.e., $k = 1$) Hopf bifurcation curve. This means that the uniform flow equilibrium (1.16),(1.18) is stable to the left of the $k = 1$ Hopf bifurcation curve; see Figs. 3.1(a) and 3.2(a). It may also be shown that the uniform flow equilibrium remains unstable to the right of the $k = 1$ curve, and as each of the $k > 1$ curves is crossed from left to right, an extra pair of complex conjugate characteristic exponents crosses into the right-half complex plane.

3.1.2 Two-dimensional stability diagrams

We now summarise the results of Section 3.1.1 by using two-parameter diagrams, i.e., we present the Hopf bifurcation curves (3.10) in the (h^*, α) plane for representative values of v^0 and n. We first focus on the case of $n = 3$ cars, where $h^* = L/3$ and wave numbers $k = 1, 2$ describe the same spatial pattern, i.e., one wave along the ring. It may be shown that the $k = 1$ curve, which is parametrised by $\omega \in (0, \pi/3)$ and depicted in Fig. 3.1(a), is the left-most curve in the $(\mathrm{V}'(h^*), \alpha)$ plane found by the above theory. This curve has a monotone shape with a vertical asymptote at $\mathrm{V}'(h^*) = \pi\sqrt{3}/9$, $\simeq 0.6046$.

By considering large α, one may apply infinite-dimensional *Routh-Hurwitz* criteria (see Stépán [105]), to show that the uniform flow equilibrium is stable to the left of this curve (all eigenvalues are situated in the left-half complex plane); see the blue shaded region in

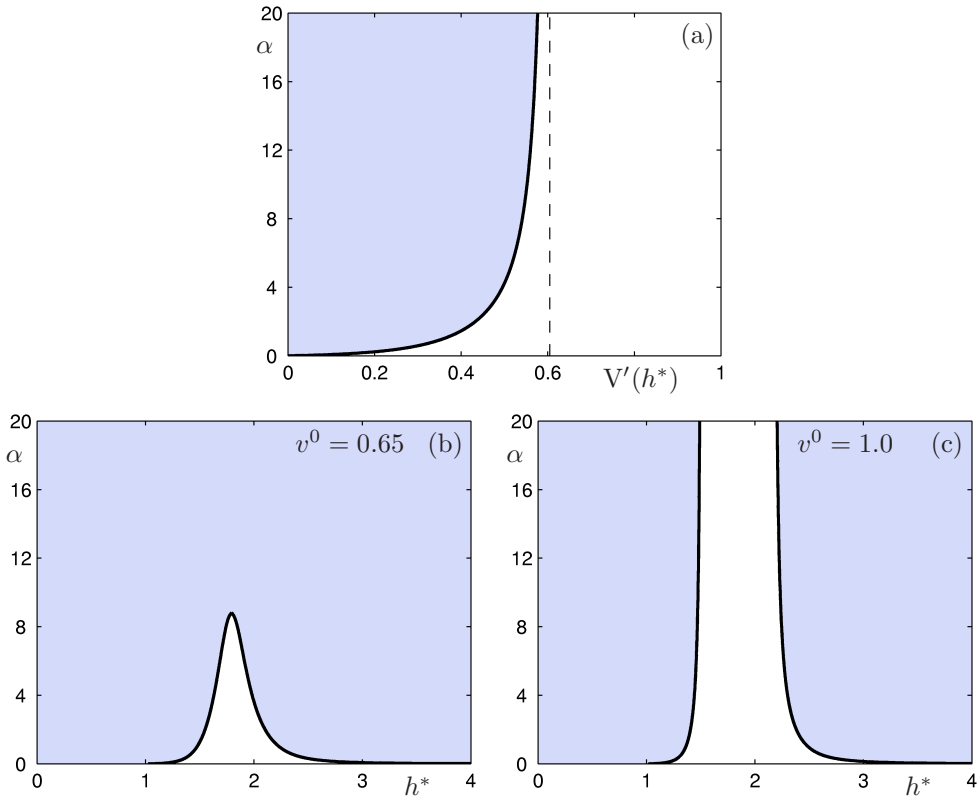

Fig. 3.1: Stability diagrams for $n = 3$ cars where blue shading denotes the stable region. Panel (a) shows the sensitivity α as a function of the slope of the OV function $\mathrm{V}'(h^*)$, where the dashed asymptote is situated at $\mathrm{V}'(h^*) \simeq 0.6046$. Panels (b) and (c) show stability diagrams in the (h^*, α) plane for particular values of v^0 (indicated in each panel), which correspond to $\mathrm{V}'_{\max} \simeq 0.5459$ and $\mathrm{V}'_{\max} \simeq 0.8399$, respectively.

Fig. 3.1(a). The equilibrium is linearly unstable in a neighbourhood of the right of the curve (there exist eigenvalues in the right-half complex plane). Hence, the $k = 1$ curve divides the $(\mathrm{V}'(h^*), \alpha)$ plane into regions where the uniform flow state is linearly stable or unstable.

Our main interest is to convert Fig. 3.1(a) to a stability diagram in the average headway-sensitivity (h^*, α) plane, when we choose the optimal velocity function $\mathrm{V}(h)$ given by (1.24) with $s = 1$. In this case $\mathrm{V}'(h)$ has a single maximum over the interval $h \in [1, \infty)$ (blue solid curve in Fig. 1.6(b)). Hence, the (h^*, α) stability diagram can be obtained from the $(\mathrm{V}'(h^*), \alpha)$ diagram by a kind of *nonlinear folding* about a vertical line whose abscissa corresponds to the maximum value $\mathrm{V}'_{\max}$ of $\mathrm{V}'(h)$; see Fig. 3.1(b) and (c), where the blue shaded regions

are stable. For $\mathrm{V}(h)$ given by (1.24) with $s = 1$, we have $\mathrm{V}'_{\max} = (2\sqrt[3]{2}/3)\, v^0$, $\simeq 0.8399\, v^0$. Hence, two qualitatively different cases of diagrams in the (h^*, α) plane are possible:

1. In the first case shown in Fig. 3.1(b), the maximum value $\mathrm{V}'_{\max}$ is to the left of the asymptote on the $(\mathrm{V}'(h^*), \alpha)$ plane. This corresponds to $v^0 < \pi\sqrt{3}/6\sqrt[3]{2}$, $\simeq 0.7198$. In this case, there is a critical sensitivity, $\tilde{\alpha}$; such that for $\alpha > \tilde{\alpha}$, uniform flow equilibria are stable for all values of the average headway h^*. For $\alpha < \tilde{\alpha}$, there is a bounded interval of h^* corresponding to unstable equilibria.

2. In the second case shown in Fig. 3.1(c), the maximum value $\mathrm{V}'_{\max}$ is to the right of the asymptote on the $(\mathrm{V}'(h^*), \alpha)$ plane. This corresponds to $v^0 \geq \pi\sqrt{3}/6\sqrt[3]{2}$, $\simeq 0.7198$. In this case, for *any* value of α there is an unstable interval of the average headway h^*. It is not possible to stabilise all uniform flows by increasing α.

In either of the two cases above, decreasing α (or increasing v^0) increases the size of the unstable h^* interval, with the left-hand end point approaching 1, and the right-hand end point approaching $+\infty$, as $\alpha \to 0$.

When we consider different values of the scaling parameter s the stability charts shown in Fig. 3.1(b) and (c) do not change qualitatively. Here $\mathrm{V}'_{\max} = (2\sqrt[3]{2}/3s)\, v^0$, $\simeq (0.8399/s)\, v^0$ for general s, which only yields quantitative changes.

The qualitative picture for OV functions $\mathrm{V}_{\mathrm{B4}}(h)$ (1.25) and $\mathrm{V}_{\mathrm{S}}(h)$ (1.26) (green dashed-dotted and red dashed curves in Fig. 1.6) is similar, except for the following. For the function $\mathrm{V}_{\mathrm{S}}(h)$, the left-hand end of the unstable h^* interval is fixed at $h^* = 1$ for all α for which there is instability. For the function $\mathrm{V}_{\mathrm{B4}}(h)$, the left-hand end point of the unstable h^* interval attains $h^* = 1$ for positive α. These features are due to the discontinuities in the functions $\mathrm{V}'_{\mathrm{B4}}(h)$ and $\mathrm{V}'_{\mathrm{S}}(h)$ at $h^* = 1$ and the fact that $\mathrm{V}'_{\mathrm{S}}(h)$ also has its maximum at $h^* = 1^+$.

Now, we demonstrate how the stability diagrams change when the number of the cars is increased. In Fig. 3.2 we present stability diagrams for $n = 9$ cars. There are four nested Hopf bifurcation curves corresponding to the four admissible wave numbers $k = 1, 2, 3, 4$. This

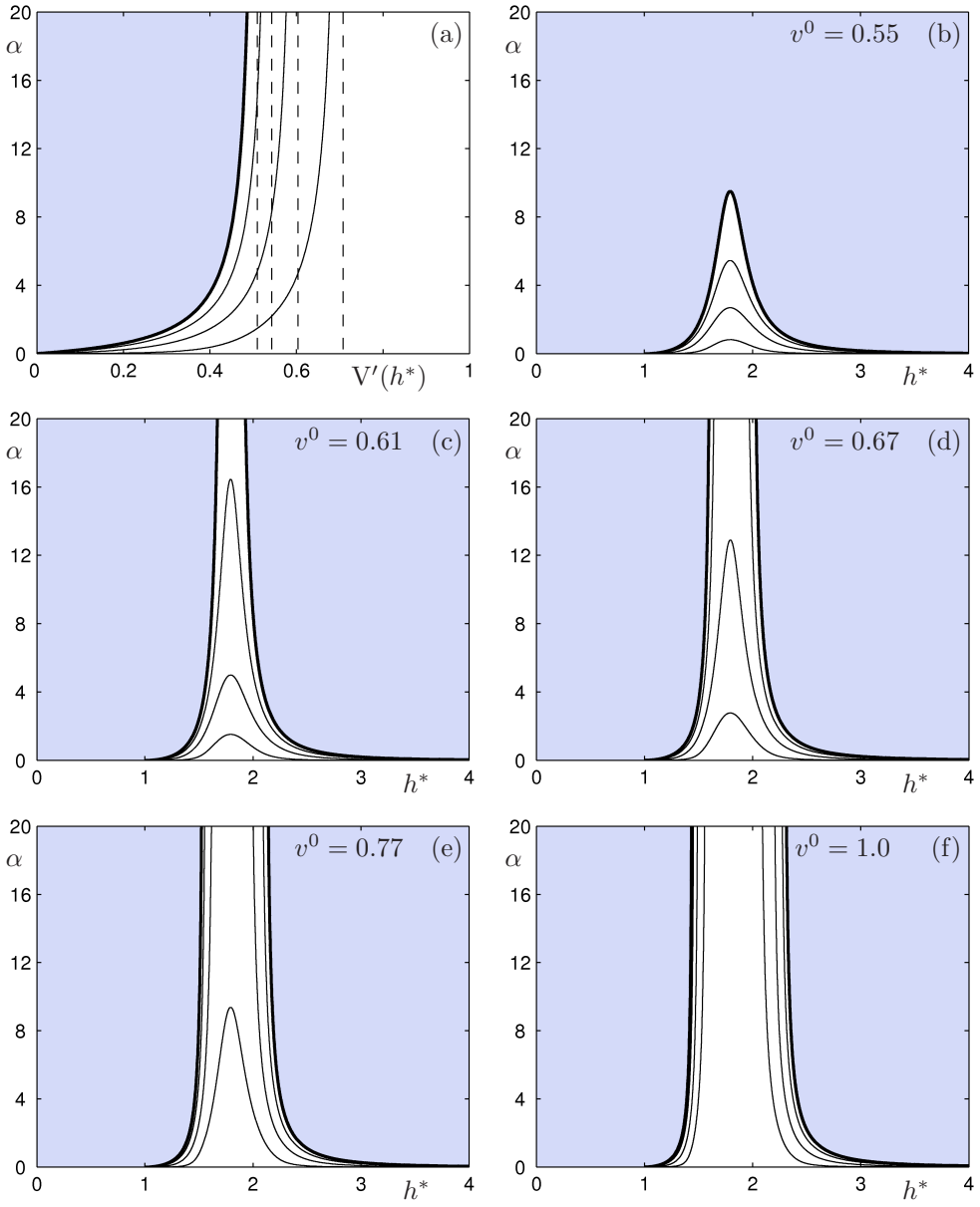

Fig. 3.2: Stability diagrams for $n = 9$ cars where blue shading denotes the stable region. Panel (a) shows the sensitivity α as a function of the slope of the OV function $\mathrm{V}'(h^*)$, where the dashed asymptotes are situated at $\mathrm{V}'(h^*) \simeq 0.5103$, $\mathrm{V}'(h^*) \simeq 0.5431$, $\mathrm{V}'(h^*) \simeq 0.6046$, and $\mathrm{V}'(h^*) \simeq 0.7089$. Panels (b)–(f) show stability diagrams in the (h^*, α) plane for particular values of v^0 (indicated in each panel), which correspond to $\mathrm{V}'_{\max} \simeq 0.4619$, $\mathrm{V}'_{\max} \simeq 0.5123$, $\mathrm{V}'_{\max} \simeq 0.5627$, $\mathrm{V}'_{\max} \simeq 0.6367$, and $\mathrm{V}'_{\max} \simeq 0.8399$, respectively.

example is sufficient to give an indication of the structure for large n. The Hopf bifurcation curves are shown in the $(\mathrm{V}'(h^*), \alpha)$ plane in Fig. 3.2(a). The stability boundary, i.e., the curve for $k = 1$, is the bold curve. The asymptotes are indicated by vertical dashed lines and the blue shaded area is the stable region of the uniform flow equilibrium (1.16),(1.18).

Since the first derivative of the OV function (1.24) has a turning point (see Fig. 1.6(b)), the $(\mathrm{V}'(h^*), \alpha)$ stability diagram of Fig. 3.2(a) may be transformed again into the (h^*, α) plane by a sort of *nonlinear folding*. Here, five qualitatively different configurations are possible and shown in Figs. 3.2(b)–(f); which situation occurs depends on the value of $\mathrm{V}'_{\max} = (2\sqrt[3]{2}/3)\, v^0$, $\simeq 0.8399\, v^0$.

The blue shaded area again corresponds to the stability of the uniform flow equilibrium (1.16),(1.18) and the Hopf bifurcation curves are nested in strict order from outside to inside as k increases. When $\mathrm{V}'_{\max}$ is to the left of a particular asymptote in the $(\mathrm{V}'(h^*), \alpha)$ plane, the corresponding curve in the (h^*, α) plane is a single curve with a maximum. On the other hand, when $\mathrm{V}'_{\max}$ is to the right of this asymptote, there are two corresponding curves in the (h^*, α) plane and each possesses a vertical asymptote. Correspondingly, all curves have maxima in Fig. 3.2(b) because $\mathrm{V}'_{\max}$ is to the left of the first (bold) Hopf curve in Fig. 3.2(a). When $\mathrm{V}'_{\max}$ exceeds the $\mathrm{V}'(h^*)$ value of the asymptote of a certain Hopf curve in the $(\mathrm{V}'(h^*), \alpha)$ plane, then the corresponding curve in the (h^*, α) plane becomes unbounded. Because there are four Hopf curves, this analysis leads to the additional four possibilities shown in Fig. 3.2(c)–(f). The left-hand endpoints of the Hopf curves approach $(1, 0)$, while their right-hand endpoints approach $(+\infty, 0)$.

By considering (3.20) and taking into account the first derivative of the OV function (1.24), it can be shown that when $\mathrm{V}'_{\max} \geq \pi/4$, (that is, when $v^0 \geq 3\pi/8\sqrt[3]{2}$, $\simeq 0.9351$), the asymptotes converge to particular values of h^* as $n \to \infty$; see Fig. 3.2(f) for which $v^0 = 1.0$. Moreover, the $k > 1$ curves accumulate on the $k = 1$ curves as $n \to \infty$.

In the absence of reaction time delay, it may be shown that the Hopf bifurcation curves are straight lines in the $(\mathrm{V}'(h^*), \alpha)$ plane given by $\alpha = 2\cos^2(k\pi/n)\, \mathrm{V}'(h^*)$. As a consequence, the

stability diagram in the (h^*, α) plane is always qualitatively the same as that in Fig. 3.2(b). Further, for non-zero delay, the Hopf curves are always nested in strict order in the (h^*, α) plane when $\mathrm{V}'_{\max} \geq \pi/4$ (i.e., when $v^0 \geq 3\pi/8\sqrt[3]{2}$, $\simeq 0.9351$). However, when the delay is zero, such a nesting only occurs for sufficiently large v^0. Thus even at the linear level, the inclusion of delay leads to new types of qualitative dynamics.

In Chapter 4, numerical continuation software is used to add further curves to Figs. 3.1 and 3.2 corresponding to fold bifurcations of the periodic orbits.

3.2 General theory of weakly nonlinear analysis

We now attempt a weakly nonlinear analysis of the Hopf bifurcations which were analysed at the linear level in Section 3.1. In particular this allows us to determine the criticality of these bifurcations. This work is split into two parts: in this section we develop a general theory for the Hopf bifurcation calculation in the presence of translational symmetry, and in Section 3.3 we apply this theory to the car-following example (1.4),(1.23).

The presence of translational symmetry gives rise to a zero characteristic exponent in the linearized system at any of the equilibrium solutions. This happens in a way similar to that of the so-called compartment systems presented by Krisztin in [71], and causes singularities in the standard Hopf bifurcation calculation shown in Section 2.3. Some of the corresponding linear algebraic equations, which arise in the standard Hopf bifurcation calculation, cannot be solved due to the presence of the zero characteristic root. This causes major difficulties when the algorithm is implemented in symbolic manipulation (such as Maple or Mathematica). To avoid this problem, we develop the Hopf bifurcation calculation for these systems after subtracting the subspace related to the translational symmetry. We note that this kind of symmetry can also be found in the dynamics of coupled cell networks near an equilibrium, as presented by Campbell *et al.* [22], and in the dynamics of semiconductor lasers near a *continuous wave* state, as shown by Rottschäfer & Krauskopf [94] and by Verduyn Lunel & Krauskopf [115].

3.2.1 Analytical framework in the presence of translational symmetry

When translational symmetry occurs in a delayed dynamical system, its motion can be shifted by constant values, in the following sense. Let us consider the special nonlinear retarded functional differential equation (RFDE) in the form

$$\dot{y}(t) = f(Ky_t; \eta)\,, \tag{3.21}$$

where the dot refers to the derivative with respect to the time t, the state variable is $y\colon \mathbb{R} \to \mathbb{R}^m$, and the function $y_t\colon \mathbb{R} \to \mathbb{X}_{\mathbb{R}^m}$ is defined by the shift $y_t(\vartheta) = y(t+\vartheta)$, $\vartheta \in [-r, 0]$, where the length of the delay $r \in \mathbb{R}^+$ is assumed to be finite. The linear functional $K\colon \mathbb{X}_{\mathbb{R}^m} \to \mathbb{R}^m$ acts on the function space $\mathbb{X}_{\mathbb{R}^m}$ of $\mathbb{R} \to \mathbb{R}^m$ continuous functions. Particularly, in this section we consider $[-r, 0] \to \mathbb{R}^m$ functions, while in the subsequent section we deal with $[-1, 0] \to \mathbb{R}^m$ functions. For the sake of simplicity, let the bifurcation parameter be the scalar $\eta \in \mathbb{R}$, and then let the function $f\colon \mathbb{R}^m \times \mathbb{R} \to \mathbb{R}^m$ be analytic, and

$$f(0; \eta) = 0\,, \tag{3.22}$$

for any η. Thus the trivial solution $y(t) \equiv 0$ of the RFDE (3.21) exists for all the values of the bifurcation parameter. Since the space $\mathbb{X}_{\mathbb{R}^m}$ is infinite-dimensional, the dimension of the phase space of RFDE (3.21) also becomes infinite.

According to the *Riesz Representation Theorem*, the linear functional K has the general form defined by the *Stieltjes integral*

$$Ky_t = \int_{-r}^{0} \mathrm{d}\gamma(\vartheta) y(t+\vartheta)\,, \tag{3.23}$$

where the matrix $\gamma\colon [-r, 0] \to \mathbb{R}^{m\times m}$ is a function of bounded variation.

The translational symmetry of the system (3.21) is expressed by the following property of the linear functional K:

$$\mathrm{Ker}\left(\int_{-r}^{0} \mathrm{d}\gamma(\vartheta)\right) \neq \{0\} \quad \Leftrightarrow \quad \det \int_{-r}^{0} \mathrm{d}\gamma(\vartheta) = 0\,. \tag{3.24}$$

Consequently, if there is a solution $\hat{y}(t)$ of (3.21) for a certain parameter η, then $\hat{y}(t) + c$ is also a solution if the constant vector $c \in \mathbb{R}^m$ satisfies $Kc = 0$ or, equivalently, if the linear

homogeneous algebraic equation

$$\int_{-r}^{0} \mathrm{d}\gamma(\vartheta)c = 0\,, \tag{3.25}$$

is satisfied. Indeed,

$$\frac{\mathrm{d}}{\mathrm{d}t}(\hat{y}(t)+c) = \dot{\hat{y}}(t)\,, \tag{3.26}$$

and

$$f\left(K(\hat{y}_t + c);\eta\right) = f\left(K\hat{y}_t + Kc;\eta\right) = f(K\hat{y}_t;\eta)\,, \tag{3.27}$$

which is implied by (3.24). Condition (3.24) also implies that infinitely many vectors c satisfy (3.25).

In other words, $y(t) \equiv 0$ is not the only trivial solution of RFDE (3.21). Any solution $y(t) \equiv c$ satisfies (3.21) for all the parameter values η since

$$f(Kc;\eta) = f\left(\int_{-r}^{0} \mathrm{d}\gamma(\vartheta)c;\eta\right) = f(0;\eta) = 0 \tag{3.28}$$

is satisfied by infinitely many vectors c due to the property (3.24).

The class of delayed systems described above can be generalised further for systems governed by

$$\dot{y}(t) = f_1(K_1 y_t;\eta) + f_2(K_2 y_t;\eta)\,. \tag{3.29}$$

These systems also have translational symmetry if the two linear functionals satisfy

$$\mathrm{Ker}\left(\int_{-r}^{0} \mathrm{d}\gamma_1(\vartheta)\right) \cap \mathrm{Ker}\left(\int_{-r}^{0} \mathrm{d}\gamma_2(\vartheta)\right) \neq \{0\}\,, \tag{3.30}$$

which implies that the corresponding determinants are zero:

$$\det \int_{-r}^{0} \mathrm{d}\gamma_1(\vartheta) = 0\,, \quad \det \int_{-r}^{0} \mathrm{d}\gamma_2(\vartheta) = 0\,. \tag{3.31}$$

However, it is condition (3.30) that guarantees that infinitely many constant vectors c satisfy $K_1 c = 0$ and $K_2 c = 0$. Consequently, if there is a solution $\hat{y}(t)$ of (3.29) for a certain parameter η, then $\hat{y}(t) + c$ is also a solution.

The linearization of RFDE (3.21) at any of its trivial solutions c in (3.25) results in the variational system

$$\dot{y}(t) = \int_{-r}^{0} \mathrm{d}_\vartheta \zeta(\vartheta;\eta) y(t+\vartheta)\,, \tag{3.32}$$

where the matrix function $\eta\colon \mathbb{R}\times\mathbb{R}\to\mathbb{R}^{m\times m}$ is defined by

$$\zeta(\vartheta;\eta) = \mathrm{D}_y f(0;\eta)\gamma(\vartheta)\,, \tag{3.33}$$

and the matrix $\mathrm{D}_y f \in \mathbb{R}^{m\times m}$ is the derivative of f. Clearly, condition (3.24) yields

$$\det \int_{-r}^{0} \mathrm{d}_\vartheta \zeta(\vartheta;\eta) = \det\left(\mathrm{D}_y f(0;\eta)\int_{-r}^{0}\mathrm{d}\gamma(\vartheta)\right) = 0\,, \tag{3.34}$$

for all values of the bifurcation parameter η.

Similar to the case of linear ODEs, the substitution of the trial solution $y(t) = C\mathrm{e}^{\lambda t}$ into (3.32) with a constant vector $C\in\mathbb{C}^m$ and characteristic exponent $\lambda\in\mathbb{C}$ results in the characteristic equation

$$D(\lambda;\eta) = \det\left(\lambda\mathrm{I} - \int_{-r}^{0}\mathrm{d}_\vartheta\zeta(\vartheta;\eta)\mathrm{e}^{\lambda\vartheta}\right) = 0\,. \tag{3.35}$$

Among the infinitely many characteristic exponents, there is

$$\lambda_0(\eta) \equiv 0\,, \tag{3.36}$$

for any η, since ζ satisfies (3.34). If the multiplicity of the zero characteristic exponent is only one, the corresponding eigenvector spans the linear one-dimensional eigenspace embedded in the infinite-dimensional phase space of the nonlinear RFDE (3.21). Along this the trivial solutions $y(t)\equiv c$ satisfying condition (3.25) are located. In the same way, possible corresponding high-dimensional subspaces can also be identified for the more general case (3.29).

Obviously, these trivial solutions of the nonlinear RFDE (3.21) cannot be asymptotically stable for any bifurcation parameter η. Still, they can be stable in the Lyapunov sense if all the other infinitely many characteristic exponents are situated in the left half of the complex plane. Also, Hopf bifurcations may occur in the complementary part of the phase space with respect to the eigenspace of the zero characteristic exponent if there exist purely imaginary characteristic exponents at some critical parameter value η_{cr}:

$$\lambda_{1,2}(\eta_{\mathrm{cr}}) = \pm\mathrm{i}\omega\,, \quad \omega\in\mathbb{R}^+\,. \tag{3.37}$$

Similarly to the case without translational symmetry described in Section 2.2, the corresponding stability boundaries are described by

$$R(\omega) = \operatorname{Re} D(\mathrm{i}\omega; \eta_{\mathrm{cr}}) = 0\,, \qquad S(\omega) = \operatorname{Im} D(\mathrm{i}\omega; \eta_{\mathrm{cr}}) = 0\,, \tag{3.38}$$

and are parameterised by the frequency $\omega \in \mathbb{R}^+$ referring to the imaginary part of the critical characteristic exponents (3.37). Since (3.35) has infinitely many solutions for λ, infinite-dimensional version of *Routh-Hurwitz* criteria are needed to decide on which side of the stability boundaries the steady state is stable or unstable [68, 92, 103, 105].

Another condition on the existence of Hopf bifurcation is the nonzero speed of the critical characteristic exponents $\lambda_{1,2}$ (3.37) when they cross the imaginary axis due to the variation of the bifurcation parameter η:

$$\operatorname{Re}\left(\frac{\mathrm{d}\lambda_{1,2}(\eta_{\mathrm{cr}})}{\mathrm{d}\eta}\right) = \operatorname{Re}\left(-\frac{\partial D(\lambda_{1,2}; \eta_{\mathrm{cr}})}{\partial \eta}\left(\frac{\partial D(\lambda_{1,2}; \eta_{\mathrm{cr}})}{\partial \lambda}\right)^{-1}\right) \neq 0\,. \tag{3.39}$$

This can be checked by implicit differentiation of the characteristic function (3.35).

The super- or subcritical nature of the Hopf bifurcation, that is, the stability and estimated amplitudes of the periodic motions arising about the stable or unstable trivial solutions, can be determined via the investigation of the third-degree power series of the original nonlinear RFDE (3.21). The above conditions (3.37) and (3.39) can be checked using the variational system (3.32) independently from the zero characteristic exponent (3.36). In contrast, the lengthy calculation with the nonlinear part leads to unsolvable singular equations if the eigenspace corresponding to the zero characteristic exponent is not removed.

In the subsequent sections, the type of the Hopf bifurcation is determined when a zero characteristic exponent exists due to the translational symmetry in the nonlinear system (3.21) induced by (3.24). The algorithm will be presented for the case of a single discrete time delay.

3.2.2 Hopf bifurcation calculations in the presence of translational symmetry

The following analysis is based on the work of Stépán [104, 105]. However, the calculations here are carried out for a DDE system of arbitrary size and also for the case of a singular Jacobian resulted by a translational symmetry as explained above. Let us consider the following autonomous nonlinear system

$$\dot{y}(t) = \tilde{\mathrm{L}}(\eta)y(t) + \tilde{\mathrm{R}}(\eta)y(t-1) + \tilde{F}(y(t), y(t-1); \eta)\,, \tag{3.40}$$

where the delay has already been rescaled to 1. According to (3.24), the constant matrices $\tilde{\mathrm{L}}, \tilde{\mathrm{R}} \colon \mathbb{R} \to \mathbb{R}^{m\times m}$ satisfy

$$\det\big(\tilde{\mathrm{L}}(\eta) + \tilde{\mathrm{R}}(\eta)\big) = 0\,. \tag{3.41}$$

The near-zero analytic function $\tilde{F} \colon \mathbb{R}^m \times \mathbb{R}^m \times \mathbb{R} \to \mathbb{R}^m$ keeps the translational symmetry, so that

$$\tilde{F}(y(t) + c, y(t-1) + c; \eta) = \tilde{F}(y(t), y(t-1); \eta)\,, \tag{3.42}$$

for all $c \neq 0$, such that $\big(\tilde{\mathrm{L}}(\eta) + \tilde{\mathrm{R}}(\eta)\big)c = 0$. This condition is fulfilled, for example, by

$$\tilde{F}(y(t), y(t-1); \eta) = \tilde{F}^{\mathrm{ex}}\big(\tilde{\mathrm{L}}(\eta)y(t) + \tilde{\mathrm{R}}(\eta)y(t-1)\big)\,, \tag{3.43}$$

when system (3.40) is considered in the form of (3.21) satisfying conditions (3.24), and consequently (3.25).

The characteristic equation of (3.40) assumes the form

$$D(\lambda; \eta) = \det\big(\lambda \mathrm{I} - \tilde{\mathrm{L}}(\eta) - \tilde{\mathrm{R}}(\eta)\mathrm{e}^{-\lambda}\big) = 0\,. \tag{3.44}$$

Condition (3.41) implies that the zero exponent (3.36) exists, that is,

$$\lambda_0(\eta) \equiv 0 \tag{3.45}$$

is always a characteristic root.

Furthermore, we suppose that the necessary conditions (3.37) and (3.39) are also fulfilled, i.e., there exists a critical parameter η_{cr}, such that

$$\lambda_{1,2}(\eta_{\mathrm{cr}}) = \pm \mathrm{i}\omega\,, \quad \mathrm{Re}\left(\frac{\mathrm{d}\lambda_{1,2}(\eta_{\mathrm{cr}})}{\mathrm{d}\eta}\right) \neq 0\,. \tag{3.46}$$

At the critical bifurcation parameter η_{cr}, the delay differential equation (3.40) takes the form

$$\dot{y}(t) = \mathrm{L}y(t) + \mathrm{R}y(t-1) + F(y(t), y(t-1))\,, \tag{3.47}$$

where the matrices $\mathrm{L}, \mathrm{R} \in \mathbb{R}^{m\times m}$, and the near-zero nonlinear function $F\colon \mathbb{R}^m \times \mathbb{R}^m \to \mathbb{R}^m$ are given by

$$\mathrm{L} = \tilde{\mathrm{L}}(\eta_{\mathrm{cr}})\,, \quad \mathrm{R} = \tilde{\mathrm{R}}(\eta_{\mathrm{cr}})\,, \quad \text{and} \quad F(y(t), y(t-1)) = \tilde{F}(y(t), y(t-1); \eta_{\mathrm{cr}})\,. \tag{3.48}$$

Equation (3.47) can be rewritten in the form of an operator differential equation (OpDE):

$$\dot{y}_t = \mathcal{A}y_t + \mathcal{F}(y_t)\,, \tag{3.49}$$

where the dot still refers to differentiation with respect to the time t, and the linear and nonlinear operators $\mathcal{A}$, $\mathcal{F}\colon \mathbb{X}_{\mathbb{R}^m} \to \mathbb{X}_{\mathbb{R}^m}$ are defined as

$$\mathcal{A}\phi(\vartheta) = \begin{cases} \dfrac{\partial}{\partial\vartheta}\phi(\vartheta)\,, & \text{if} \quad -1 \leq \vartheta < 0\,, \\ \mathrm{L}\phi(0) + \mathrm{R}\phi(-1)\,, & \text{if} \quad \vartheta = 0\,, \end{cases} \tag{3.50}$$

$$\mathcal{F}(\phi)(\vartheta) = \begin{cases} 0\,, & \text{if} \quad -1 \leq \vartheta < 0\,, \\ F(\phi(0), \phi(-1))\,, & \text{if} \quad \vartheta = 0\,. \end{cases} \tag{3.51}$$

We note that here the $[-1, 0] \to \mathbb{R}^m$ functions are considered in the function space $\mathbb{X}_{\mathbb{R}^m}$ of $\mathbb{R} \to \mathbb{R}^m$ continuous functions.

The translational symmetry is inherited by the DDE (3.47) and by the OpDE (3.49), since (3.41) implies

$$\det(\mathrm{L} + \mathrm{R}) = 0\,, \tag{3.52}$$

and similarly, (3.42) implies that the near-zero nonlinear function F and the near-zero nonlinear operator $\mathcal{F}$ satisfy

$$F(y(t) + c, y(t-1) + c) = F(y(t), y(t-1)) \quad \Leftrightarrow \quad \mathcal{F}(y_t + c) = \mathcal{F}(y_t)\,, \tag{3.53}$$

for all $c \neq 0$, such that $(\mathrm{L}+\mathrm{R})c = 0$. In accordance with (3.43), condition (3.53) is fulfilled, for example, by

$$F(y(t), y(t-1)) = F^{\mathrm{ex}}\big(\mathrm{L}y(t) + \mathrm{R}y(t-1)\big)\,. \tag{3.54}$$

Clearly, the characteristic roots of the linear part of delay differential equation (3.47) are the same as the eigenvalues of operator $\mathcal{A}$:

$$D(\lambda;\eta_{\mathrm{cr}}) = \det\big(\lambda\mathrm{I} - \mathrm{L} - \mathrm{R}\mathrm{e}^{-\lambda}\big) = 0 \quad \Leftrightarrow \quad \mathrm{Ker}(\lambda\mathcal{I} - \mathcal{A}) \neq \{0\}\,, \tag{3.55}$$

and the corresponding three critical characteristic exponents (3.45) and (3.46) are also the same:

$$\lambda_0(\eta) \equiv 0\,, \quad \lambda_{1,2}(\eta_{\mathrm{cr}}) = \pm\mathrm{i}\omega\,. \tag{3.56}$$

If the zero characteristic root appeared only for the critical bifurcation parameter η_{cr}, then it would mean that a fold bifurcation occurs together with a Hopf bifurcation, as was found by Sieber & Krauskopf [102] in an unfolding of a degenerate case of a controlled inverted pendulum. In contrast, we consider the case where the determinants (3.41) and (3.52) hold, and the corresponding zero characteristic exponent (3.45),(3.56) exists for arbitrary bifurcation parameter η. In this case, it is impossible to carry out the Hopf bifurcation calculation by disregarding this zero characteristic root. More exactly, the centre manifold reduction related to the purely imaginary characteristic roots cannot be carried out by the usual algorithm: a linear non-homogeneous equation occurs with coefficient matrix $(\mathrm{L}+\mathrm{R})$ which cannot be solved.

We can avoid the above problem in the phase space if we restrict the system to the complementary (infinite-dimensional) space of the linear one-dimensional invariant manifold spanned by that eigenvector of the operator $\mathcal{A}$ which belongs to the zero eigenvalue. After the construction of the reduced OpDE, the usual Hopf bifurcation calculation algorithm can be carried out including the centre manifold reduction related to the purely imaginary eigenvalues.

Although the reduction of the OpDE (3.49) can be carried out for any value of the bifurcation parameter η, the calculations are presented for only the critical value η_{cr}, since

the subsequent Hopf bifurcation calculations use the system parameters only at the critical values.

The eigenvector $s_0 \in \mathbb{X}_{\mathbb{R}^m}$ of $\mathcal{A}$ associated with the eigenvalue $\lambda_0 = 0$ satisfies

$$\mathcal{A}s_0 = \lambda_0 s_0 \quad \Rightarrow \quad \mathcal{A}s_0 = 0\,. \tag{3.57}$$

The definition (3.50) of the linear operator $\mathcal{A}$ in (3.57) leads to the simple boundary value problem

$$\frac{\partial}{\partial \vartheta} s_0(\vartheta) = 0\,, \quad \mathrm{L}s_0(0) + \mathrm{R}s_0(-1) = 0\,. \tag{3.58}$$

Its constant solution is

$$s_0(\vartheta) \equiv S_0 \in \mathbb{R}^m\,, \quad (\mathrm{L} + \mathrm{R})S_0 = 0\,. \tag{3.59}$$

In order to project the system to s_0 and to its complementary space, we also need the adjoint operator:

$$\mathcal{A}^*\psi(\sigma) = \begin{cases} -\dfrac{\partial}{\partial \sigma}\psi(\sigma)\,, & \text{if} \quad 0 < \sigma \leq 1\,, \\ \mathrm{L}^*\psi(0) + \mathrm{R}^*\psi(1)\,, & \text{if} \quad \sigma = 0\,, \end{cases} \tag{3.60}$$

where * denotes either adjoint operator or transposed conjugate vector and matrix. The eigenvector $n_0 \in \mathbb{X}^*_{\mathbb{R}^m}$ of $\mathcal{A}^*$ associated with the eigenvalue $\lambda_0^* = 0$ satisfies

$$\mathcal{A}^* n_0 = \lambda_0^* n_0 \quad \Rightarrow \quad \mathcal{A}^* n_0 = 0\,. \tag{3.61}$$

Using the definition (3.60) of the adjoint operator $\mathcal{A}^*$ in (3.61) results in another boundary value problem

$$\frac{\partial}{\partial \sigma} n_0(\sigma) = 0\,, \quad \mathrm{L}^* n_0(0) + \mathrm{R}^* n_0(1) = 0\,. \tag{3.62}$$

Its solution gives

$$n_0(\sigma) \equiv N_0 \in \mathbb{R}^m\,, \quad (\mathrm{L}^* + \mathrm{R}^*)N_0 = 0\,. \tag{3.63}$$

Note that, as the vectors s_0 and n_0 are the right and left eigenvectors of the operator $\mathcal{A}$ belonging to the eigenvalues $\lambda_0 = 0$ and $\lambda_0^* = 0$, similarly the vectors S_0 and N_0 are the right and left eigenvectors of the matrix $(\mathrm{L} + \mathrm{R}\mathrm{e}^{-\lambda})$, belonging to the same eigenvalues.

One of the two free scalar variables in S_0, N_0 is determined by the normality condition

$$\langle n_0, s_0 \rangle = 1 \,. \tag{3.64}$$

Defining the inner product

$$\langle \psi, \phi \rangle = \psi^*(0)\phi(0) + \int_{-1}^{0} \psi^*(\xi+1)\mathrm{R}\phi(\xi)\mathrm{d}\xi \,, \tag{3.65}$$

condition (3.64) gives the scalar equation

$$N_0^*(\mathrm{I}+\mathrm{R})S_0 = 1 \,. \tag{3.66}$$

Let us separate the phase space with the help of the new state variables $z_0 \colon \mathbb{R} \to \mathbb{R}$ and $y_t^- : \mathbb{R} \to \mathbb{X}_{\mathbb{R}^m}$ defined as

$$\begin{cases} z_0 = \langle n_0, y_t \rangle \,, \\ y_t^- = y_t - z_0 s_0 \,. \end{cases} \tag{3.67}$$

Now the OpDE (3.49) can be semi-decoupled by using the above definitions, the normalised eigenvectors (3.59) and (3.63) satisfying (3.57) and (3.61), the inner product definition (3.65), and the translational symmetry expressed by (3.53):

$$\begin{aligned} \dot{z}_0 &= \langle n_0, \dot{y}_t \rangle = \langle n_0, \mathcal{A}y_t + \mathcal{F}(y_t) \rangle \\ &= \langle \mathcal{A}^* n_0, y_t \rangle + \langle n_0, \mathcal{F}(y_t^- + z_0 s_0) \rangle \\ &= n_0^*(0)\mathcal{F}(y_t^- + z_0 S_0)(0) = N_0^* \mathcal{F}(y_t^-)(0) \,, \\ \dot{y}_t^- &= \dot{y}_t - \dot{z}_0 s_0 = \mathcal{A}y_t + \mathcal{F}(y_t) - n_0^*(0)\mathcal{F}(y_t^- + z_0 S_0)(0) s_0 \\ &= \mathcal{A}y_t^- + z_0 \mathcal{A}s_0 + \mathcal{F}(y_t^- + z_0 S_0) - n_0^*(0)\mathcal{F}(y_t^- + z_0 S_0)(0) s_0 \\ &= \mathcal{A}y_t^- + \mathcal{F}(y_t^-) - N_0^* \mathcal{F}(y_t^-)(0) S_0 \,. \end{aligned} \tag{3.68}$$

In the first part, the scalar differential equation of (3.68) becomes fully separated, if the equation is restricted to the corresponding manifold spanned by the eigenvector s_0. Assuming $y_t^- = 0$ implies $\dot{z}_0 = 0$; hence, all the trivial solutions $y(t) \equiv c = z_0 S_0$ are situated along a straight line (the corresponding invariant manifold) at any constant z_0.

In the second part, the operator differential equation of (3.68) is already fully decoupled, and can be re-defined as

$$\dot{y}_t^- = \mathcal{A} y_t^- + \mathcal{F}^-(y_t^-)\,, \tag{3.69}$$

where the new nonlinear operator $\mathcal{F}^-$ assumes the form

$$\mathcal{F}^-(\phi)(\vartheta) = \begin{cases} -N_0^* \mathcal{F}(\phi)(0) S_0\,, & \text{if} \quad -1 \le \vartheta < 0\,, \\ \mathcal{F}(\phi)(0) - N_0^* \mathcal{F}(\phi)(0) S_0\,, & \text{if} \quad \vartheta = 0\,, \end{cases} \tag{3.70}$$

and after the substitution of definition (3.51) of the near-zero nonlinear operator $\mathcal{F}$ we obtain

$$\mathcal{F}^-(\phi)(\vartheta) = \begin{cases} -N_0^* F(\phi(0), \phi(-1)) S_0\,, & \text{if} \quad -1 \le \vartheta < 0\,, \\ F(\phi(0), \phi(-1)) - N_0^* F(\phi(0), \phi(-1)) S_0\,, & \text{if} \quad \vartheta = 0\,. \end{cases} \tag{3.71}$$

While the linear operator remains the same, the reduction of the system related to the translational symmetry changes the nonlinear operator. This change will have an essential role in the centre manifold reduction of the Hopf analysis given below.

The algorithm of the usual Hopf bifurcation analysis, reviewed in Section 2.3, is well known and presented in several books [51, 105]. Here, we apply this for the reduced OpDE (3.69). First, let us determine the real and imaginary parts $s_1, s_2 \in \mathbb{X}_{\mathbb{R}^m}$ of the eigenvector of the linear operator $\mathcal{A}$ associated with the critical eigenvalue $\lambda_1 = \mathrm{i}\omega$. These vectors satisfy

$$\mathcal{A}(s_1 + \mathrm{i}s_2) = \lambda_1(s_1 + \mathrm{i}s_2) \quad \Rightarrow \quad \mathcal{A}s_1 = -\omega s_2\,, \quad \mathcal{A}s_2 = \omega s_1\,. \tag{3.72}$$

After the substitution of definition (3.50) of operator $\mathcal{A}$, these equations form a $2m$-dimensional linear first-order boundary value problem:

$$\frac{\partial}{\partial\vartheta}\begin{bmatrix} s_1(\vartheta) \\ s_2(\vartheta) \end{bmatrix} = \omega \begin{bmatrix} 0 & -\mathrm{I} \\ \mathrm{I} & 0 \end{bmatrix} \begin{bmatrix} s_1(\vartheta) \\ s_2(\vartheta) \end{bmatrix}, \quad \begin{bmatrix} \mathrm{L} & \omega\mathrm{I} \\ -\omega\mathrm{I} & \mathrm{L} \end{bmatrix} \begin{bmatrix} s_1(0) \\ s_2(0) \end{bmatrix} + \begin{bmatrix} \mathrm{R} & 0 \\ 0 & \mathrm{R} \end{bmatrix} \begin{bmatrix} s_1(-1) \\ s_2(-1) \end{bmatrix} = \begin{bmatrix} 0 \\ 0 \end{bmatrix}. \tag{3.73}$$

Its solution is

$$\begin{bmatrix} s_1(\vartheta) \\ s_2(\vartheta) \end{bmatrix} = \begin{bmatrix} S_1 \\ S_2 \end{bmatrix} \cos(\omega\vartheta) + \begin{bmatrix} -S_2 \\ S_1 \end{bmatrix} \sin(\omega\vartheta)\,, \tag{3.74}$$

with constant vectors $S_1, S_2 \in \mathbb{R}^m$ having two freely eligible scalar variables while satisfying the homogeneous equations

$$\begin{bmatrix} \mathrm{L} + \mathrm{R}\cos\omega & \omega\mathrm{I} + \mathrm{R}\sin\omega \\ -(\omega\mathrm{I} + \mathrm{R}\sin\omega) & \mathrm{L} + \mathrm{R}\cos\omega \end{bmatrix} \begin{bmatrix} S_1 \\ S_2 \end{bmatrix} = \begin{bmatrix} 0 \\ 0 \end{bmatrix} . \tag{3.75}$$

The real and imaginary parts $n_1, n_2 \in \mathbb{X}^*_{\mathbb{R}^m}$ of the eigenvector of the adjoint operator $\mathcal{A}^*$ associated with the eigenvalue $\lambda_1^* = -\mathrm{i}\omega$ are determined by

$$\mathcal{A}^*(n_1 + \mathrm{i}n_2) = \lambda_1^*(n_1 + \mathrm{i}n_2) \quad \Rightarrow \quad \mathcal{A}^* n_1 = \omega n_2 \,, \quad \mathcal{A}^* n_2 = -\omega n_1 \,. \tag{3.76}$$

It results in the $2m$-dimensional boundary value problem

$$\frac{\partial}{\partial\sigma} \begin{bmatrix} n_1(\sigma) \\ n_2(\sigma) \end{bmatrix} = \omega \begin{bmatrix} 0 & -\mathrm{I} \\ \mathrm{I} & 0 \end{bmatrix} \begin{bmatrix} n_1(\sigma) \\ n_2(\sigma) \end{bmatrix}, \quad \begin{bmatrix} \mathrm{L}^* & -\omega\mathrm{I} \\ \omega\mathrm{I} & \mathrm{L}^* \end{bmatrix} \begin{bmatrix} n_1(0) \\ n_2(0) \end{bmatrix} + \begin{bmatrix} \mathrm{R}^* & 0 \\ 0 & \mathrm{R}^* \end{bmatrix} \begin{bmatrix} n_1(1) \\ n_2(1) \end{bmatrix} = \begin{bmatrix} 0 \\ 0 \end{bmatrix} , \tag{3.77}$$

when one uses definition (3.60) of operator $\mathcal{A}^*$. It has the solution

$$\begin{bmatrix} n_1(\sigma) \\ n_2(\sigma) \end{bmatrix} = \begin{bmatrix} N_1 \\ N_2 \end{bmatrix} \cos(\omega\sigma) + \begin{bmatrix} -N_2 \\ N_1 \end{bmatrix} \sin(\omega\sigma) \,, \tag{3.78}$$

where the constant vectors $N_1, N_2 \in \mathbb{R}^m$ also possess two free scalar variables while satisfying

$$\begin{bmatrix} \mathrm{L}^* + \mathrm{R}^*\cos\omega & -(\omega\mathrm{I} + \mathrm{R}^*\sin\omega) \\ \omega\mathrm{I} + \mathrm{R}^*\sin\omega & \mathrm{L}^* + \mathrm{R}^*\cos\omega \end{bmatrix} \begin{bmatrix} N_1 \\ N_2 \end{bmatrix} = \begin{bmatrix} 0 \\ 0 \end{bmatrix} . \tag{3.79}$$

As $s_1 + \mathrm{i}s_2$ and $n_1 + \mathrm{i}n_2$ are the right and left eigenvectors of the operator $\mathcal{A}$ belonging to the eigenvalues $\lambda_1 = \mathrm{i}\omega$ and $\lambda_1^* = -\mathrm{i}\omega$, the vectors $S_1 + \mathrm{i}S_2$ and $N_1 + \mathrm{i}N_2$ are similarly the right and left eigenvectors of the matrix $(\mathrm{L} + \mathrm{R}\mathrm{e}^{-\lambda})$ belonging to the same eigenvalues.

The orthonormality conditions

$$\langle n_1, s_1 \rangle = 1 \,, \quad \langle n_1, s_2 \rangle = 0 \tag{3.80}$$

determine two of the four free scalar values in vectors S_1, S_2, N_1, N_2. The application of the inner product definition (3.65) results in two linear equations, which are arranged for the two

free parameters in N_1 and N_2 in the following way:

$$\frac{1}{2}\begin{bmatrix} S_1^*\left(2\mathrm{I}+\mathrm{R}^*\left(\cos\omega+\frac{\sin\omega}{\omega}\right)\right)+S_2^*\mathrm{R}^*\sin\omega & -S_1^*\mathrm{R}^*\sin\omega+S_2^*\mathrm{R}^*\left(\cos\omega-\frac{\sin\omega}{\omega}\right) \\ -S_1^*\mathrm{R}^*\sin\omega+S_2^*\left(2\mathrm{I}+\mathrm{R}^*\left(\cos\omega+\frac{\sin\omega}{\omega}\right)\right) & -S_1^*\mathrm{R}^*\left(\cos\omega-\frac{\sin\omega}{\omega}\right)-S_2^*\mathrm{R}^*\sin\omega \end{bmatrix} \times \begin{bmatrix} N_1 \\ N_2 \end{bmatrix} = \begin{bmatrix} 1 \\ 0 \end{bmatrix}. \tag{3.81}$$

Note that taking 1 and 0 as first (or last) components of the vectors S_1 and S_2, respectively, is a reasonable choice for the two remaining scalar parameters; see Section 3.3 and also [21].

With the help of the right and left eigenvectors s_1, s_2 and n_1, n_2 of operator $\mathcal{A}$, we introduce the new state variables

$$\begin{cases} z_1 = \langle n_1, y_t^- \rangle\,, \\ z_2 = \langle n_2, y_t^- \rangle\,, \\ w = y_t^- - z_1 s_1 - z_2 s_2\,, \end{cases} \tag{3.82}$$

where $z_1, z_2 \colon \mathbb{R} \to \mathbb{R}$ and $w \colon \mathbb{R} \to \mathbb{X}_{\mathbb{R}^m}$. Using the above definitions, the eigenvectors (3.74) and (3.78) satisfying (3.72) and (3.76), the inner product definition (3.65), and the definition of operator $\mathcal{F}^-$ (3.70), the reduced OpDE (3.69) can be rewritten in the form

$$\begin{aligned} \dot{z}_1 &= \langle n_1, \dot{y}_t^- \rangle = \langle n_1, \mathcal{A}y_t^- + \mathcal{F}^-(y_t^-) \rangle = \langle \mathcal{A}^* n_1, y_t^- \rangle + \langle n_1, \mathcal{F}^-(y_t^-) \rangle \\ &= \omega \langle n_2, y_t^- \rangle + n_1^*(0)\mathcal{F}^-(y_t^-)(0) + \int_{-1}^{0} n_1^*(\xi+1)\mathrm{R}\mathcal{F}^-(y_t^-)(\xi)\mathrm{d}\xi \\ &= \omega z_2 + n_1^*(0)\mathcal{F}(y_t^-)(0) - \left(n_1^*(0)\mathrm{I} + \int_{-1}^{0} n_1^*(\xi+1)\mathrm{d}\xi\mathrm{R}\right)(N_0^*\mathcal{F}(y_t^-)(0)S_0) \\ &= \omega z_2 + \left(N_1^* - \left(\left(N_1^*(\mathrm{I}+\tfrac{\sin\omega}{\omega}\mathrm{R}) - N_2^*\tfrac{1-\cos\omega}{\omega}\mathrm{R}\right)S_0\right)N_0^*\right)\mathcal{F}(y_t^-)(0)\,, \\ \dot{z}_2 &= -\omega z_1 + \left(N_2^* - \left(\left(N_1^*\tfrac{1-\cos\omega}{\omega}\mathrm{R} + N_2^*(\mathrm{I}+\tfrac{\sin\omega}{\omega}\mathrm{R})\right)S_0\right)N_0^*\right)\mathcal{F}(y_t^-)(0)\,, \\ \dot{w} &= \dot{y}_t^- - \dot{z}_1 s_1 - \dot{z}_2 s_2 = \mathcal{A}y_t^- + \mathcal{F}^-(y_t^-) - \omega z_2 s_1 + \omega z_1 s_2 \\ &\quad - \left(N_1^* - \left(\left(N_1^*(\mathrm{I}+\tfrac{\sin\omega}{\omega}\mathrm{R}) - N_2^*\tfrac{1-\cos\omega}{\omega}\mathrm{R}\right)S_0\right)N_0^*\right)\mathcal{F}(y_t^-)(0)s_1 \\ &\quad - \left(N_2^* - \left(\left(N_1^*\tfrac{1-\cos\omega}{\omega}\mathrm{R} + N_2^*(\mathrm{I}+\tfrac{\sin\omega}{\omega}\mathrm{R})\right)S_0\right)N_0^*\right)\mathcal{F}(y_t^-)(0)s_2\,. \end{aligned} \tag{3.83}$$

The introduction of the new scalar parameters

$$\begin{aligned} q_1 &= \left(N_1^*(\mathrm{I} + \tfrac{\sin\omega}{\omega}\mathrm{R}) - N_2^*\tfrac{1-\cos\omega}{\omega}\mathrm{R}\right) S_0\,, \\ q_2 &= \left(N_1^*\tfrac{1-\cos\omega}{\omega}\mathrm{R} + N_2^*(\mathrm{I} + \tfrac{\sin\omega}{\omega}\mathrm{R})\right) S_0 \end{aligned} \tag{3.84}$$

is related to the translational symmetry, that is, q_1 and q_2 would be zero if there were no zero characteristic root in the system (3.49), because in that case $S_0 = 0$. But even if the translational symmetry is there, it is often possible to find $N_1^*\mathrm{R}S_0 = N_2^*\mathrm{R}S_0 = N_1^*S_0 = N_2^*S_0 = 0$ resulting in $q_1 = q_2 = 0$, for example, when $\mathrm{R}S_0 = 0$ also holds in addition to $(\mathrm{L} + \mathrm{R})S_0 = 0$ in (3.59).

The structure of the new form of the reduced OpDE (3.69) is as follows:

$$\begin{aligned} \begin{bmatrix} \dot{z}_1 \\ \dot{z}_2 \\ \dot{w} \end{bmatrix} &= \begin{bmatrix} 0 & \omega & \mathcal{O} \\ -\omega & 0 & \mathcal{O} \\ 0 & 0 & \mathcal{A} \end{bmatrix} \begin{bmatrix} z_1 \\ z_2 \\ w \end{bmatrix} \\ &+ \begin{bmatrix} (N_1^* - q_1N_0^*)\mathcal{F}(z_1s_1 + z_2s_2 + w)(0) \\ (N_2^* - q_2N_0^*)\mathcal{F}(z_1s_1 + z_2s_2 + w)(0) \\ -\sum_{j=1,2}(N_j^* - q_jN_0^*)\mathcal{F}(z_1s_1 + z_2s_2 + w)(0)s_j + \mathcal{F}^-(z_1s_1 + z_2s_2 + w) \end{bmatrix}, \end{aligned} \tag{3.85}$$

where $\mathcal{F}(z_1s_1 + z_2s_2 + w)(0) = F(z_1s_1(0) + z_2s_2(0) + w(0), z_1s_1(-1) + z_2s_2(-1) + w(-1))$ according to (3.51), and this expression also appears in $\mathcal{F}^-(z_1s_1 + z_2s_2 + w)$ as defined by (3.70) and (3.71).

We need to expand the nonlinearities in power series form, and to keep only those which result in terms up to third order after the reduction to the centre manifold. In order to do this, we calculate only the terms having second and third order in z_1, z_2 and the terms wz_1, wz_2 for $\dot{z}_1, \dot{z}_2$, while only the second-order terms in z_1, z_2 are needed for $\dot{w}$; see already (3.87) and (3.88). This calculation is possible via the Taylor expansion of the analytic function $F\colon \mathbb{R}^m \times \mathbb{R}^m \to \mathbb{R}^m$ of (3.48) in the definitions (3.51) and (3.71) of the near-zero operators

$\mathcal{F}$ and $\mathcal{F}^-$. The resulting truncated OpDE assumes the form

$$\begin{aligned}\begin{bmatrix}\dot{z}_1\\ \dot{z}_2\\ \dot{w}\end{bmatrix} &= \begin{bmatrix}0 & \omega & \mathcal{O}\\ -\omega & 0 & \mathcal{O}\\ 0 & 0 & \mathcal{A}\end{bmatrix}\begin{bmatrix}z_1\\ z_2\\ w\end{bmatrix} + \begin{bmatrix}\sum_{j,k\geq 0}^{j+k=2,3} f_{jk}^{(1)} z_1^j z_2^k\\ \sum_{j,k\geq 0}^{j+k=2,3} f_{jk}^{(2)} z_1^j z_2^k\\ \frac{1}{2}\sum_{j,k\geq 0}^{j+k=2}\big(F_{jk}^{(3\mathrm{c})}\cos(\omega\vartheta) + F_{jk}^{(3\mathrm{s})}\sin(\omega\vartheta)\big) z_1^j z_2^k\end{bmatrix}\\ &+ \begin{bmatrix}\big(F_{10}^{(1l)*}w(0) + F_{10}^{(1r)*}w(-1)\big)z_1 + \big(F_{01}^{(1l)*}w(0) + F_{01}^{(1r)*}w(-1)\big)z_2\\ \big(F_{10}^{(2l)*}w(0) + F_{10}^{(2r)*}w(-1)\big)z_1 + \big(F_{01}^{(2l)*}w(0) + F_{01}^{(2r)*}w(-1)\big)z_2\\ \frac{1}{2}\begin{cases}\sum_{j,k\geq 0}^{j+k=2} F_{jk}^{(3-)} z_1^j z_2^k\,, & \text{if} \quad -1\leq\vartheta<0\,,\\ \sum_{j,k\geq 0}^{j+k=2}\big(F_{jk}^{(3)} + F_{jk}^{(3-)}\big) z_1^j z_2^k\,, & \text{if} \quad \vartheta=0\end{cases}\end{bmatrix}.\end{aligned} \tag{3.86}$$

The subscripts of the constant coefficients $f_{jk}^{(1)}, f_{jk}^{(2)} \in \mathbb{R}$ and the vector ones $F_{jk}^{(1l)}, F_{jk}^{(1r)}, F_{jk}^{(2l)}$, $F_{jk}^{(2r)}, F_{jk}^{(3\mathrm{c})}, F_{jk}^{(3\mathrm{s})}, F_{jk}^{(3)}, F_{jk}^{(3-)} \in \mathbb{R}^m$ refer to the corresponding jth and kth orders of z_1 and z_2, respectively. The terms with the coefficients $F_{jk}^{(3\mathrm{c})}$ and $F_{jk}^{(3\mathrm{s})}$ come from the linear combinations of $s_1(\vartheta)$ and $s_2(\vartheta)$. Note that all coefficients of the nonlinear terms are influenced by the scalar parameters q_1 and q_2 (see (3.84)) related to the translational symmetry, except for $F_{jk}^{(3)}$ and $F_{jk}^{(3-)}$ (see (3.85)). The terms with coefficients $F_{jk}^{(3)}$ and $F_{jk}^{(3-)}$ refer to the structure of the modified nonlinear operator $\mathcal{F}^-$ (see (3.70), (3.71)), that is, the vectors $F_{jk}^{(3-)}$ appear due to the translational symmetry only, while the vectors $F_{jk}^{(3)}$ would appear anyway.

The plane spanned by the eigenvectors s_1 and s_2 is tangent to the centre manifold at the origin. This means that the centre manifold can be approximated locally as a truncated power series of w depending on the second order of the coordinates z_1 and z_2:

$$w(\vartheta) = \frac{1}{2}\left(h_{20}(\vartheta)z_1^2 + 2h_{11}(\vartheta)z_1 z_2 + h_{02}(\vartheta)z_2^2\right). \tag{3.87}$$

The unknown coefficients h_{20}, $h_{11}, h_{02} \in \mathbb{X}_{\mathbb{R}^m}$ can be determined by calculating the derivative of w in (3.87). On the one hand, it is expressed to second order by the substitution of the linear part of the first two equations of (3.86):

$$\dot{w}(\vartheta) = -\omega h_{11}(\vartheta)z_1^2 + \omega(h_{20}(\vartheta) - h_{02}(\vartheta))z_1 z_2 + \omega h_{11}(\vartheta)z_2^2\,. \tag{3.88}$$

On the other hand, this derivative can also be expressed by the third equation of (3.86). The comparison of the coefficients of z_1^2, $z_1 z_2$, and z_2^2 gives a linear boundary value problem with

differential equation

$$\begin{aligned}\frac{\partial}{\partial\vartheta}\begin{bmatrix}h_{20}(\vartheta)\\ h_{11}(\vartheta)\\ h_{02}(\vartheta)\end{bmatrix} &= \begin{bmatrix}0 & -2\omega\mathrm{I} & 0\\ \omega\mathrm{I} & 0 & -\omega\mathrm{I}\\ 0 & 2\omega\mathrm{I} & 0\end{bmatrix}\begin{bmatrix}h_{20}(\vartheta)\\ h_{11}(\vartheta)\\ h_{02}(\vartheta)\end{bmatrix}\\ &\quad - \begin{bmatrix}F_{20}^{(3\mathrm{c})}\\ \frac{1}{2}F_{11}^{(3\mathrm{c})}\\ F_{02}^{(3\mathrm{c})}\end{bmatrix}\cos(\omega\vartheta) - \begin{bmatrix}F_{20}^{(3\mathrm{s})}\\ \frac{1}{2}F_{11}^{(3\mathrm{s})}\\ F_{02}^{(3\mathrm{s})}\end{bmatrix}\sin(\omega\vartheta) - \begin{bmatrix}F_{20}^{(3-)}\\ \frac{1}{2}F_{11}^{(3-)}\\ F_{02}^{(3-)}\end{bmatrix},\end{aligned} \tag{3.89}$$

and boundary condition

$$\begin{bmatrix}\mathrm{L} & 2\omega\mathrm{I} & 0\\ -\omega\mathrm{I} & \mathrm{L} & \omega\mathrm{I}\\ 0 & -2\omega\mathrm{I} & \mathrm{L}\end{bmatrix}\begin{bmatrix}h_{20}(0)\\ h_{11}(0)\\ h_{02}(0)\end{bmatrix} + \begin{bmatrix}\mathrm{R} & 0 & 0\\ 0 & \mathrm{R} & 0\\ 0 & 0 & \mathrm{R}\end{bmatrix}\begin{bmatrix}h_{20}(-1)\\ h_{11}(-1)\\ h_{02}(-1)\end{bmatrix} = -\begin{bmatrix}F_{20}^{(3\mathrm{c})}+F_{20}^{(3)}+F_{20}^{(3-)}\\ \frac{1}{2}\big(F_{11}^{(3\mathrm{c})}+F_{11}^{(3)}+F_{11}^{(3-)}\big)\\ F_{02}^{(3\mathrm{c})}+F_{02}^{(3)}+F_{02}^{(3-)}\end{bmatrix}. \tag{3.90}$$

Note that the constant vector in the non-homogeneous term of (3.89), formed by the vectors $F_{jk}^{(3-)}$, does not show up if there is no translational symmetry, that is, if there is no zero characteristic exponent in the system. The general solution of (3.89) also contains extra terms that are related to the translational symmetry through the vectors $F_{jk}^{(3-)}$:

$$\begin{aligned}\begin{bmatrix}h_{20}(\vartheta)\\ h_{11}(\vartheta)\\ h_{02}(\vartheta)\end{bmatrix} &= \begin{bmatrix}H_1\\ H_2\\ -H_1\end{bmatrix}\cos(2\omega\vartheta) + \begin{bmatrix}-H_2\\ H_1\\ H_2\end{bmatrix}\sin(2\omega\vartheta) + \begin{bmatrix}H_0\\ 0\\ H_0\end{bmatrix}\\ &\quad + \frac{1}{3\omega}\left(\begin{bmatrix}F_{11}^{(3\mathrm{c})}+F_{20}^{(3\mathrm{s})}+2F_{02}^{(3\mathrm{s})}\\ -\frac{1}{2}F_{11}^{(3\mathrm{s})}-F_{20}^{(3\mathrm{c})}+F_{02}^{(3\mathrm{c})}\\ -F_{11}^{(3\mathrm{c})}+2F_{20}^{(3\mathrm{s})}+F_{02}^{(3\mathrm{s})}\end{bmatrix}\cos(\omega\vartheta) + \begin{bmatrix}F_{11}^{(3\mathrm{s})}-F_{20}^{(3\mathrm{c})}-2F_{02}^{(3\mathrm{c})}\\ \frac{1}{2}F_{11}^{(3\mathrm{c})}-F_{20}^{(3\mathrm{s})}+F_{02}^{(3\mathrm{s})}\\ -F_{11}^{(3\mathrm{s})}-2F_{20}^{(3\mathrm{c})}-F_{02}^{(3\mathrm{c})}\end{bmatrix}\sin(\omega\vartheta)\right)\\ &\quad - \frac{1}{4\omega}\begin{bmatrix}0\\ F_{20}^{(3-)}-F_{02}^{(3-)}\\ 2F_{11}^{(3-)}\end{bmatrix} - \frac{1}{2}\begin{bmatrix}F_{20}^{(3-)}+F_{02}^{(3-)}\\ 0\\ F_{20}^{(3-)}+F_{02}^{(3-)}\end{bmatrix}\vartheta\,.\end{aligned} \tag{3.91}$$

The unknown constant vectors $H_0, H_1, H_2 \in \mathbb{R}^m$ are determined by the boundary condition

(3.90), which result in the linear non-homogeneous equation

$$\begin{bmatrix} \mathrm{L}+\mathrm{R} & 0 & 0 \\ 0 & \mathrm{L}+\mathrm{R}\cos(2\omega) & 2\omega\mathrm{I}+\mathrm{R}\sin(2\omega) \\ 0 & -\big(2\omega\mathrm{I}+\mathrm{R}\sin(2\omega)\big) & \mathrm{L}+\mathrm{R}\cos(2\omega) \end{bmatrix} \begin{bmatrix} H_0 \\ H_1 \\ H_2 \end{bmatrix}$$
$$= \frac{1}{6\omega} \begin{bmatrix} (\mathrm{L}+\mathrm{R}\cos\omega)\big(-3F_{20}^{(3\mathrm{s})}-3F_{02}^{(3\mathrm{s})}\big)+(\omega\mathrm{I}+\mathrm{R}\sin\omega)\big(-3F_{20}^{(3\mathrm{c})}-3F_{02}^{(3\mathrm{c})}\big) \\ (\mathrm{L}+\mathrm{R}\cos\omega)\big(-2F_{11}^{(3\mathrm{c})}+F_{20}^{(3\mathrm{s})}-F_{02}^{(3\mathrm{s})}\big)+(\omega\mathrm{I}+\mathrm{R}\sin\omega)\big(2F_{11}^{(3\mathrm{s})}+F_{20}^{(3\mathrm{c})}-F_{02}^{(3\mathrm{c})}\big) \\ (\mathrm{L}+\mathrm{R}\cos\omega)\big(F_{11}^{(3\mathrm{s})}+2F_{20}^{(3\mathrm{c})}-2F_{02}^{(3\mathrm{c})}\big)+(\omega\mathrm{I}+\mathrm{R}\sin\omega)\big(F_{11}^{(3\mathrm{c})}-2F_{20}^{(3\mathrm{s})}+2F_{02}^{(3\mathrm{s})}\big) \end{bmatrix}$$
$$- \frac{1}{4\omega} \begin{bmatrix} 2\omega\big(F_{20}^{(3)}+F_{02}^{(3)}\big)+2\omega(\mathrm{I}+\mathrm{R})\big(F_{20}^{(3-)}+F_{02}^{(3-)}\big)-(\mathrm{L}+\mathrm{R})F_{11}^{(3-)} \\ 2\omega\big(F_{20}^{(3)}-F_{02}^{(3)}\big)+(\mathrm{L}+\mathrm{R})F_{11}^{(3-)} \\ 2\omega F_{11}^{(3)}-(\mathrm{L}+\mathrm{R})\big(F_{20}^{(3-)}-F_{02}^{(3-)}\big) \end{bmatrix}. \tag{3.92}$$

Since $(\mathrm{L}+\mathrm{R})$ is singular for systems with translational symmetry, the first (decoupled) group of non-homogeneous equations for H_0 may look as thought they are not solvable. However, the non-homogeneous term on the right-hand side belongs to the image space of the coefficient matrix $(\mathrm{L}+\mathrm{R})$, and this will result in a solution that is satisfactory for the centre manifold calculation; see Section 3.3. Again, this issue is related to the translational symmetry in the system. If the reduction of the OpDE (3.49) were not carried out to the reduced OpDE (3.69) with respect to the relevant zero characteristic root, then the first (decoupled) group of (3.92) would lead to contradiction, and the centre manifold calculation could not be continued.

By having the solution of (3.92), we can reconstruct the approximate equation of the centre manifold via (3.87) and (3.91). Then calculating only the components $w(0)$ and $w(-1)$, and substituting them into the first two scalar equations of (3.86), we obtain the following equations that describe the flow restricted onto the two-dimensional centre manifold:

$$\begin{bmatrix} \dot{z}_1 \\ \dot{z}_2 \end{bmatrix} = \begin{bmatrix} 0 & \omega \\ -\omega & 0 \end{bmatrix} \begin{bmatrix} z_1 \\ z_2 \end{bmatrix} + \begin{bmatrix} \sum_{j,k\geq 0}^{j+k=2,3} f_{jk}^{(1)} z_1^j z_2^k \\ \sum_{j,k\geq 0}^{j+k=2,3} f_{jk}^{(2)} z_1^j z_2^k \end{bmatrix} + \begin{bmatrix} \sum_{j,k\geq 0}^{j+k=3} g_{jk}^{(1)} z_1^j z_2^k \\ \sum_{j,k\geq 0}^{j+k=3} g_{jk}^{(2)} z_1^j z_2^k \end{bmatrix}. \tag{3.93}$$

We note that the coefficients $f_{jk}^{(1)}$ and $f_{jk}^{(2)}$ of the second-order terms are not changed by the

centre manifold reduction. The so-called Poincaré-Lyapunov constant in the Poincaré normal form of (3.93) can be determined by the Bautin formula

$$\begin{aligned}\Delta = \frac{1}{8}\Bigg(\frac{1}{\omega}\Big((f_{20}^{(1)}+f_{02}^{(1)})(-f_{11}^{(1)}+f_{20}^{(2)}-f_{02}^{(2)})+(f_{20}^{(2)}+f_{02}^{(2)})(f_{20}^{(1)}-f_{02}^{(1)}+f_{11}^{(2)})\Big)\\ +\Big(3f_{30}^{(1)}+f_{12}^{(1)}+f_{21}^{(2)}+3f_{03}^{(2)}\Big)+\Big(3g_{30}^{(1)}+g_{12}^{(1)}+g_{21}^{(2)}+3g_{03}^{(2)}\Big)\Bigg),\end{aligned} \tag{3.94}$$

see [47, 105]. It shows the type of bifurcation and approximate amplitude of the limit-cycle oscillations. The bifurcation is supercritical (subcritical) if $\Delta < 0$ ($\Delta > 0$), and the amplitude of the stable (unstable) oscillations is expressed by

$$A = \sqrt{-\frac{1}{\Delta}\mathrm{Re}\frac{\mathrm{d}\lambda_1(\eta_{\mathrm{cr}})}{\mathrm{d}\eta}(\eta-\eta_{\mathrm{cr}})}\,. \tag{3.95}$$

Thus the first Fourier term of the oscillation on the centre manifold is

$$\begin{bmatrix} z_1(t) \\ z_2(t) \end{bmatrix} = A \begin{bmatrix} \cos(\omega t) \\ -\sin(\omega t) \end{bmatrix}. \tag{3.96}$$

Since close to the critical bifurcation parameter η_{cr} we have $y_t(\vartheta) \approx z_1(t)s_1(\vartheta) + z_2(t)s_2(\vartheta)$, equation (3.96) yields

$$\begin{aligned} y(t) = y_t(0) &\approx z_1(t)s_1(0) + z_2(t)s_2(0) \\ &= A\big(s_1(0)\cos(\omega t) - s_2(0)\sin(\omega t)\big) \\ &= A\big(S_1\cos(\omega t) - S_2\sin(\omega t)\big)\,. \end{aligned} \tag{3.97}$$

We reduced the infinite-dimensional problem into the solution of the closed-form linear algebraic equations (3.59),(3.63),(3.66),(3.75),(3.79),(3.81), and (3.92). Thus, we are able to determine the quantities Δ (3.94) and A (3.95) in *any* dynamical system with a single delay and translational symmetry.

3.3 Application to the car-following model

Having developed a general theory of Hopf calculation in the presence of translational symmetry, we now turn our attention to applying this theory to the car-following model (1.23).

First, we write these equations in the operator differential equation (OpDE) form (3.49). Then the normal form calculations are carried out using the results of Section 3.2.2. Finally, an interpretation of the obtained results is given.

3.3.1 Car-following model in OpDE form

By considering the kinematic conditions (1.4) and substituting (1.5) into (1.23), we obtain

$$\begin{aligned} \ddot{x}_i(t) &= \alpha\big(\mathrm{V}\left(x_{i+1}(t-1)-x_i(t-1)\right)-\dot{x}_i(t)\big), \quad i=1,\dots,n-1\,,\\ \ddot{x}_n(t) &= \alpha\big(\mathrm{V}\left(x_1(t-1)-x_n(t-1)+L\right)-\dot{x}_n(t)\big)\,. \end{aligned} \tag{3.98}$$

Let us recall the definition (1.16)–(1.19) for the uniform flow equilibrium, that is,

$$x_i^{\mathrm{eq}}(t)=v^*\,t+x_i^*\,, \quad \Rightarrow \quad \dot{x}_i^{\mathrm{eq}}(t)\equiv v^*\,, \quad i=1,\dots,n\,, \tag{3.99}$$

where

$$x_{i+1}^*-x_i^*=x_1^*-x_n^*+L=L/n:=h^*, \quad i=1,\dots,n-1\,, \tag{3.100}$$

and

$$v^*=\mathrm{V}(h^*)<v^0\,. \tag{3.101}$$

Note that one of the constants x_i^* can be chosen arbitrarily due to the translational symmetry along the ring. Henceforth, we consider the average headway h^* as a bifurcation parameter, that is, according to the notation of Section 3.2, $\eta=h^*$.

Using definition (3.1) for the perturbation of the uniform flow equilibrium, i.e.,

$$x_i^{\mathrm{p}}(t)\colon=x_i(t)-(v^*t+x_i^*)\,, \quad i=1,\dots,n\,, \tag{3.102}$$

and the Taylor series expansion of the optimal velocity function $\mathrm{V}(h)$ about $h=h^*$ up to third order, we can eliminate the zero-order terms and obtain

$$\begin{aligned} \ddot{x}_i^{\mathrm{p}}(t) &= -\alpha\dot{x}_i^{\mathrm{p}}(t)+\alpha\sum_{k=1}^{3}b_k(h^*)\big(x_{i+1}^{\mathrm{p}}(t-1)-x_i^{\mathrm{p}}(t-1)\big)^k\,, \quad i=1,\dots,n-1\,,\\ \ddot{x}_n^{\mathrm{p}}(t) &= -\alpha\dot{x}_n^{\mathrm{p}}(t)+\alpha\sum_{k=1}^{3}b_k(h^*)\big(x_1^{\mathrm{p}}(t-1)-x_n^{\mathrm{p}}(t-1)\big)^k\,, \end{aligned} \tag{3.103}$$

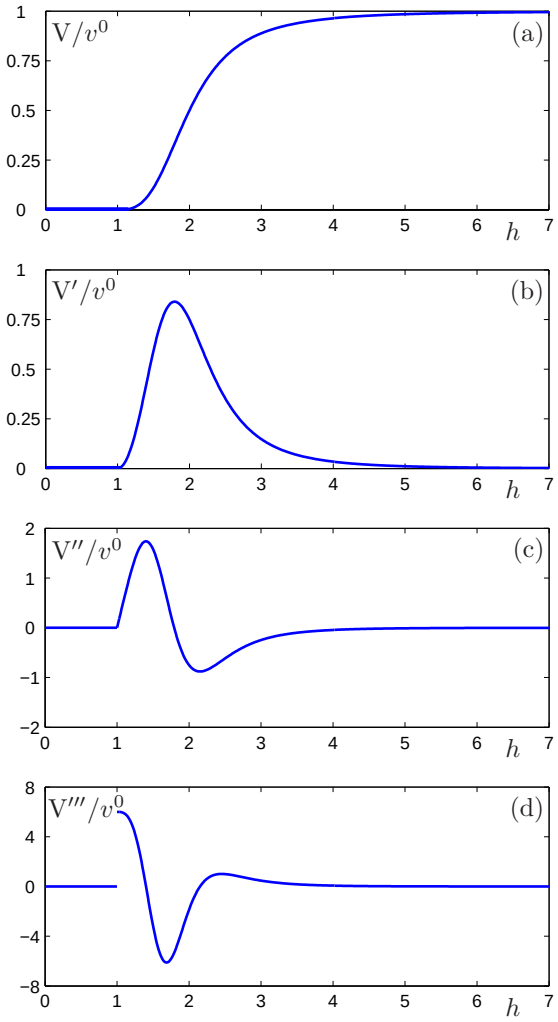

Fig. 3.3: The optimal velocity function (1.24) is shown in panel (a) and its derivatives are displayed in panels (b)–(d).

where

$$b_1(h^*) = \mathrm{V}'(h^*)\,, \quad b_2(h^*) = \frac{1}{2}\mathrm{V}''(h^*)\,, \quad \text{and} \quad b_3(h^*) = \frac{1}{6}\mathrm{V}'''(h^*)\,. \tag{3.104}$$

At a critical bifurcation parameter $h^*_{\rm cr}$ the derivatives take the values $b_{1\rm cr} = \mathrm{V}'(h^*_{\rm cr})$, $b_{2\rm cr} = \frac{1}{2}\mathrm{V}''(h^*_{\rm cr})$, and $b_{3\rm cr} = \frac{1}{6}\mathrm{V}'''(h^*_{\rm cr})$.

The optimal velocity function (1.24) for $s = 1$ is shown together with its first, second, and third derivatives in Fig. 3.3. Note that the analytical calculations presented in this section

are valid for *any* OV function $\mathrm{V}(h)$: it is not necessary to restrict ourselves to a concrete function in contrast to numerical simulation and numerical continuation approaches.

Introducing the notation

$$y_i(t) := \dot{x}_i^{\mathrm{p}}(t)\,, \quad y_{i+n}(t) := x_i^{\mathrm{p}}(t)\,, \quad i = 1, \dots, n\,, \tag{3.105}$$

equation (3.103) can be written as

$$\dot{y}(t) = \tilde{\mathrm{L}}(h^*)y(t) + \tilde{\mathrm{R}}(h^*)y(t-1) + \tilde{F}\big(y(t-1); h^*\big)\,, \tag{3.106}$$

where $y\colon \mathbb{R} \to \mathbb{R}^{2n}$. The matrices $\tilde{\mathrm{L}}, \tilde{\mathrm{R}}\colon \mathbb{R} \to \mathbb{R}^{2n\times 2n}$ and the near-zero analytic function $\tilde{F}\colon \mathbb{R}^{2n} \times \mathbb{R} \to \mathbb{R}^{2n}$ are defined by

$$\begin{aligned} \tilde{\mathrm{L}}(h^*) &\equiv \begin{bmatrix} -\alpha \mathrm{I} & 0 \\ \mathrm{I} & 0 \end{bmatrix}\,, \qquad \tilde{\mathrm{R}}(h^*) = \begin{bmatrix} 0 & -\alpha b_1(h^*)\mathrm{A} \\ 0 & 0 \end{bmatrix}\,, \\ \tilde{F}\big(y(t-1); h^*\big) &= \begin{bmatrix} \alpha b_2(h^*) F_2\big(y(t-1)\big) + \alpha b_3(h^*) F_3\big(y(t-1)\big) \\ 0 \end{bmatrix}\,. \end{aligned} \tag{3.107}$$

Here $\mathrm{I} \in \mathbb{R}^{n\times n}$ stands for the $n \times n$ identity matrix, while the matrix $\mathrm{A} \in \mathbb{R}^{n\times n}$ and the functions $F_2, F_3\colon \mathbb{R}^{2n} \to \mathbb{R}^n$ are defined by

$$\mathrm{A} = \begin{bmatrix} \ddots & \ddots & & \\ & 1 & -1 & \\ & & \ddots & \ddots \\ -1 & & & \ddots \end{bmatrix}\,, \quad F_k\big(y(t-1)\big) = \begin{bmatrix} \big(y_{n+2}(t-1) - y_{n+1}(t-1)\big)^k \\ \big(y_{n+3}(t-1) - y_{n+2}(t-1)\big)^k \\ \vdots \\ \big(y_{n+1}(t-1) - y_{2n}(t-1)\big)^k \end{bmatrix}\,, \quad k = 2, 3\,. \tag{3.108}$$

Equation (3.106) is in the from of (3.40), that is, here $m = 2n$. Although the function $\tilde{F}$ does not depend on $y(t)$, the general theory of Section 3.2 can be applied by leaving out the first argument of $\tilde{F}$ as shown below. Indeed, the trivial solution $y(t) \equiv 0$ of (3.106) corresponds to the uniform flow equilibrium (3.99) of the original system (3.98).

Since system (3.106) possesses a translational symmetry, the matrices $\tilde{\mathrm{L}}(h^*), \tilde{\mathrm{R}}(h^*)$ satisfy

$$\det\big(\tilde{\mathrm{L}}(h^*) + \tilde{\mathrm{R}}(h^*)\big) = 0\,, \tag{3.109}$$

that is, the Jacobian $\big(\tilde{\mathrm{L}}(h^*)+\tilde{\mathrm{R}}(h^*)\big)$ has a zero eigenvalue

$$\lambda_0(h^*)=0\,, \tag{3.110}$$

for any value of parameter h^*. Furthermore, the near-zero analytic function $\tilde{F}$ preserves this translational symmetry, that is,

$$\tilde{F}\big(y(t-1)+c;h^*\big)=\tilde{F}\big(y(t-1);h^*\big)\,, \tag{3.111}$$

for all $c\neq 0$ satisfying $\big(\tilde{\mathrm{L}}(h^*)+\tilde{\mathrm{R}}(h^*)\big)c=0$.

Now we recall formulae (3.8)–(3.12) determined in Section 3.1 but write them according to the notation and formalism of this section. Considering the linear part of (3.106), the general formula (3.44) leads to the characteristic equation

$$D\big(\lambda;b_1(h^*)\big)=\big(\lambda^2+\alpha\lambda+\alpha b_1(h^*)\mathrm{e}^{-\lambda}\big)^n-\big(\alpha b_1(h^*)\mathrm{e}^{-\lambda}\big)^n=0\,. \tag{3.112}$$

According to (3.109), the relevant zero eigenvalue (3.110) is one of the infinitely many characteristic exponents that satisfy (3.112). This exponent exists for any value of the parameter b_1, that is, for any value of the bifurcation parameter h^*.

At a bifurcation point defined by $b_1=b_{1\mathrm{cr}}$, i.e., by $h^*=h^*_{\mathrm{cr}}$, Hopf bifurcations may occur in the complementary part of the phase space spanned by the eigenspace of the zero exponent (3.110). Then there exists a complex conjugate pair of purely imaginary characteristic exponents

$$\lambda_{1,2}(h^*_{\mathrm{cr}})=\pm\mathrm{i}\omega\,,\quad \omega\in\mathbb{R}^+\,, \tag{3.113}$$

which satisfies (3.112) and the corresponding Hopf boundaries are described by

$$\begin{aligned} b_{1\mathrm{cr}}&=\frac{\omega}{2\cos(\omega-\frac{k\pi}{n})\sin(\frac{k\pi}{n})}\,,\\ \alpha&=-\omega\cot(\omega-\tfrac{k\pi}{n})\,, \end{aligned} \tag{3.114}$$

which can be transformed into

$$\begin{aligned} \cos\omega&=\frac{\omega}{2b_{1\mathrm{cr}}}\left(\frac{\omega}{\alpha}+\cot(\tfrac{k\pi}{n})\right)\,,\\ \sin\omega&=\frac{\omega}{2b_{1\mathrm{cr}}}\left(1-\frac{\omega}{\alpha}\cot(\tfrac{k\pi}{n})\right)\,, \end{aligned} \tag{3.115}$$

yielding

$$\frac{4b_{1\mathrm{cr}}^2}{\omega^2}\sin^2(\tfrac{k\pi}{n}) = 1 + \frac{\omega^2}{\alpha^2}\,. \tag{3.116}$$

The wave numbers are $k = 1, \ldots, n/2$ (for even n) and $k = 1, \ldots (n-1)/2$ (for odd n). Furthermore, for each k the resulting frequency is bounded so that $\omega \in (0, \frac{k\pi}{n})$.

With the help of the identity

$$\frac{\big(1 + \mathrm{i}\cot(\frac{k\pi}{n})\big)^{n-1}}{\big(1 - \mathrm{i}\cot(\frac{k\pi}{n})\big)^{n-1}} = \frac{1 - \mathrm{i}\cot(\frac{k\pi}{n})}{1 + \mathrm{i}\cot(\frac{k\pi}{n})}\,, \tag{3.117}$$

we can calculate the necessary condition for Hopf bifurcation as the parameter b_1 is varied:

$$\mathrm{Re}\left(\frac{\mathrm{d}\lambda_1(b_{1\mathrm{cr}})}{\mathrm{d}b_1}\right) = \mathrm{Re}\left(-\frac{\partial D(\lambda_1; b_{1\mathrm{cr}})}{\partial b_1}\left(\frac{\partial D(\lambda_1; b_{1\mathrm{cr}})}{\partial \lambda}\right)^{-1}\right) = \mathcal{E}\frac{1}{b_{1\mathrm{cr}}}\left(\omega^2 + \alpha^2 + \alpha\right) > 0\,, \tag{3.118}$$

where

$$\mathcal{E} = \left(\left(\tfrac{\alpha}{\omega} - \omega\right)^2 + \left(2 + \alpha\right)^2\right)^{-1}\,. \tag{3.119}$$

Since (3.118) is always positive this Hopf condition is always satisfied. Now, using the chain rule and definition (3.104), condition (3.118) can be calculated further as the average headway h^* is varied to give

$$\mathrm{Re}\left(\lambda_1'(h_{\mathrm{cr}}^*)\right) = \mathrm{Re}\left(\frac{\mathrm{d}\lambda_1(b_{1\mathrm{cr}})}{\mathrm{d}b_1}\,b_1'(h_{\mathrm{cr}}^*)\right) = \mathcal{E}\frac{2b_{2\mathrm{cr}}}{b_{1\mathrm{cr}}}\left(\omega^2 + \alpha^2 + \alpha\right) \neq 0\,. \tag{3.120}$$

This condition is fulfilled if and only if $b_{2\mathrm{cr}} \neq 0$, which is usually satisfied except at some special points. For example, the function $\mathrm{V}''(h)$ shown in Fig. 3.3(c) becomes zero at a single point over the interval $h \in (1, \infty)$. Notice that $\mathrm{V}''(h)$ is zero for $h \in [0, 1]$ and for $h \to \infty$, but the critical headway h_{cr} never takes these values for $\alpha > 0$.

For the critical bifurcation parameter h_{cr}^*, the delay differential equation (3.106) takes the form of (3.47) so that the matrices $\mathrm{L}, \mathrm{R} \in \mathbb{R}^{2n\times 2n}$, and the near-zero nonlinear function $F\colon \mathbb{R}^{2n} \to \mathbb{R}^{2n}$ are given by

$$\mathrm{L} = \tilde{\mathrm{L}}(h_{\mathrm{cr}}^*)\,, \quad \mathrm{R} = \tilde{\mathrm{R}}(h_{\mathrm{cr}}^*)\,, \quad \text{and} \quad F\big(y(t-1)\big) = \tilde{F}\big(y(t-1); h_{\mathrm{cr}}^*\big)\,. \tag{3.121}$$

This can be rewritten in the operator differential equation (OpDE) form (3.49) so that the state variable is $y_t\colon \mathbb{R} \to \mathbb{X}_{\mathbb{R}^{2n}}$, and the linear and nonlinear operators $\mathcal{A}, \mathcal{F}\colon \mathbb{X}_{\mathbb{R}^{2n}} \to \mathbb{X}_{\mathbb{R}^{2n}}$ (3.50),(3.51) contain (3.121).

The translational symmetry conditions (3.109) and (3.111) are inherited, that is,

$$\det(\mathrm{L} + \mathrm{R}) = 0\,, \tag{3.122}$$

and

$$F\big(y(t-1)+c\big) = F\big(y(t-1)\big) \quad \Leftrightarrow \quad \mathcal{F}(y_t + c) = \mathcal{F}(y_t)\,, \tag{3.123}$$

for all $c \neq 0$ satisfying $(\mathrm{L} + \mathrm{R})c = 0$.

3.3.2 Normal form calculations of the car-following model

Following the steps of the normal form calculation in Section 3.2.2 the criticality of the Hopf bifurcations can be determined in our car-following model. In order to do this we only have to solve the algebraic equations (3.59),(3.63),(3.66),(3.75),(3.79),(3.81), and (3.92).

By solving equation (3.59) one finds that

$$S_0 = p \begin{bmatrix} 0 \\ E \end{bmatrix}\,, \tag{3.124}$$

where each component of the vector $E \in \mathbb{R}^n$ is equal to 1. Here $p \in \mathbb{R}$ is a scalar that can be chosen freely, in particular, we choose

$$p = 1\,. \tag{3.125}$$

The solution of (3.63) is written as

$$N_0 = \hat{p} \begin{bmatrix} E \\ \alpha E \end{bmatrix}\,. \tag{3.126}$$

However, $\hat{p} \in \mathbb{R}$ is not free, but is determined by the normality condition (3.66) which gives

$$\hat{p} = \frac{1}{n\alpha}\,. \tag{3.127}$$

By considering $\mathcal{F}(\phi)(0) = F(\phi(-1))$ given by (3.51), and using the expressions (3.107), (3.108) and (3.121), and the eigenvectors (3.124) and (3.126), we obtain

$$N_0^* \mathcal{F}(y_t^-)(0) S_0 = N_0^* F\big(y(t-1)\big) S_0 = \frac{1}{n} \sum_{k=2,3} \left(b_{\mathrm{kcr}} \sum_{i=1}^{n} \big(y_{n+i+1}(t-1) - y_{n+i}(t-1)\big)^k \right) \begin{bmatrix} 0 \\ E \end{bmatrix}, \tag{3.128}$$

which appears in the nonlinear operator $\mathcal{F}^-$ (3.70),(3.71) of the reduced OpDE (3.69). Note that in (3.128) the definition $y_{2n+1} := y_{n+1}$ is applied.

Using (3.115) for the Hopf boundary, the $4n$-dimensional equation (3.75) leads to

$$\left.\begin{aligned} S_{2,i} &= \omega S_{1,n+i} \\ S_{2,n+i} &= -\frac{1}{\omega} S_{1,i} \end{aligned}\right\} \quad \text{for} \quad i = 1, \ldots, n\,, \tag{3.129}$$

and to the $2n$-dimensional equation

$$\begin{bmatrix} -\frac{1}{\omega}\cot(\frac{k\pi}{n})\mathrm{A} & \mathrm{B} \\ \mathrm{B} & \frac{1}{\omega}\cot(\frac{k\pi}{n})\mathrm{A} \end{bmatrix} S_1 = 0\,, \tag{3.130}$$

where $\mathrm{A} \in \mathbb{R}^{n\times n}$ is defined by (3.108) and $\mathrm{B} \in \mathbb{R}^{n\times n}$ is given by

$$\mathrm{B} = \begin{bmatrix} \ddots & \ddots & & \\ & 1 & 1 & \\ & & \ddots & \ddots \\ 1 & & & \ddots \end{bmatrix}. \tag{3.131}$$

Solving (3.130) one may obtain

$$S_1 = u \begin{bmatrix} C \\ \frac{1}{\omega} S \end{bmatrix} + v \begin{bmatrix} S \\ -\frac{1}{\omega} C \end{bmatrix}, \quad S_2 = u \begin{bmatrix} S \\ -\frac{1}{\omega} C \end{bmatrix} - v \begin{bmatrix} C \\ \frac{1}{\omega} S \end{bmatrix}, \tag{3.132}$$

where the scalar parameters u and v can be chosen arbitrarily and the vectors $C, S \in \mathbb{R}^n$ are

$$C = \begin{bmatrix} \cos(\frac{2k\pi}{n}1) \\ \cos(\frac{2k\pi}{n}2) \\ \vdots \\ \cos(\frac{2k\pi}{n}n) \end{bmatrix}, \quad S = \begin{bmatrix} \sin(\frac{2k\pi}{n}1) \\ \sin(\frac{2k\pi}{n}2) \\ \vdots \\ \sin(\frac{2k\pi}{n}n) \end{bmatrix}, \tag{3.133}$$

with the wave number k used in (3.114)–(3.116). The cyclic permutation of the components in C and S results in further vectors S_1 and S_2 that still satisfy (3.75). This result corresponds to the $\mathbb{Z}^n$ symmetry of the system, that is, all the cars have the same dynamic characteristics. Choosing $u = 1$ and $v = 0$ yields

$$S_1 = \begin{bmatrix} C \\ \frac{1}{\omega} S \end{bmatrix}, \quad S_2 = \begin{bmatrix} S \\ -\frac{1}{\omega} C \end{bmatrix}. \tag{3.134}$$

Notice that $S_1 + \mathrm{i}S_2 = P$, given by (3.13).

The application of (3.115) simplifies the $4n$-dimensional equation (3.79) and leads to

$$\left.\begin{aligned} N_{1,n+i} &= \alpha N_{1,i} + \omega N_{2,i} \\ N_{2,n+i} &= -\omega N_{1,i} + \alpha N_{2,i} \end{aligned}\right\} \quad \text{for} \quad i = 1, \ldots, n\,, \tag{3.135}$$

and to the $2n$-dimensional equation

$$\begin{bmatrix} -\cot(\frac{k\pi}{n})\mathrm{A} & \mathrm{B} \\ \mathrm{B} & \cot(\frac{k\pi}{n})\mathrm{A} \end{bmatrix} N_{\cup} = 0\,, \tag{3.136}$$

where $N_{\cup} \in \mathbb{R}^{2n}$ is defined by

$$\left.\begin{aligned} N_{\cup,i} &= N_{1,i} \\ N_{\cup,n+i} &= N_{2,i} \end{aligned}\right\} \quad \text{for} \quad i = 1, \ldots, n\,. \tag{3.137}$$

The solution of (3.136) can be written as

$$N_{\cup} = \hat{u} \begin{bmatrix} C \\ S \end{bmatrix} + \hat{v} \begin{bmatrix} S \\ -C \end{bmatrix}, \tag{3.138}$$

which results in

$$N_1 = \hat{u} \begin{bmatrix} C \\ \alpha C + \omega S \end{bmatrix} + \hat{v} \begin{bmatrix} S \\ \alpha S - \omega C \end{bmatrix}, \quad N_2 = \hat{u} \begin{bmatrix} S \\ \alpha S - \omega C \end{bmatrix} - \hat{v} \begin{bmatrix} C \\ \alpha C + \omega S \end{bmatrix}. \tag{3.139}$$

The scalar parameters $\hat{u}$ and $\hat{v}$ are determined by the orthonormality condition (3.81). Substituting (3.115),(3.134), and (3.139) into this condition and using the second-order trigonometric identities (A.4)–(A.6) of the Appendix, we obtain

$$\frac{n}{2} \begin{bmatrix} 2+\alpha & \frac{\alpha}{\omega} - \omega \\ -\left(\frac{\alpha}{\omega} - \omega\right) & 2+\alpha \end{bmatrix} \begin{bmatrix} \hat{u} \\ \hat{v} \end{bmatrix} = \begin{bmatrix} 1 \\ 0 \end{bmatrix}, \tag{3.140}$$

with the solution

$$\begin{bmatrix} \hat{u} \\ \hat{v} \end{bmatrix} = \mathcal{E}\frac{2}{n}\begin{bmatrix} 2+\alpha \\ \frac{\alpha}{\omega}-\omega \end{bmatrix}, \tag{3.141}$$

where $\mathcal{E}$ is defined by (3.119). The substitution of (3.141) into (3.139) gives

$$N_1 = \mathcal{E}\frac{2}{n}\begin{bmatrix} (2+\alpha)C + \big(\frac{\alpha}{\omega}-\omega\big)S \\ (\alpha^2+\alpha+\omega^2)C + \big(\frac{\alpha^2}{\omega}+2\,\omega\big)S \end{bmatrix}, \quad N_2 = \mathcal{E}\frac{2}{n}\begin{bmatrix} (2+\alpha)S - \big(\frac{\alpha}{\omega}-\omega\big)C \\ (\alpha^2+\alpha+\omega^2)S - \big(\frac{\alpha^2}{\omega}+2\,\omega\big)C \end{bmatrix}. \tag{3.142}$$

In our case $\mathrm{R}S_0 = N_1^* S_0 = N_2^* S_0 = 0$, therefore (3.84) provides

$$q_1 = q_2 = 0\,. \tag{3.143}$$

Thus, considering (3.85) and (3.86) the translational symmetry only enters through the terms with coefficients $F_{jk}^{(3-)}$, so that the terms with coefficients $F_{jk}^{(3)}$ and $F_{jk}^{(3-)}$ refer to the structure of the modified nonlinear operator $\mathcal{F}^-$ (3.70),(3.71). Using the third- and fourth-order trigonometric identities (A.7)–(A.15) of the Appendix, we can calculate the coefficients in (3.86) for wave numbers $k \neq n/2$, $k \neq n/3$, and $k \neq n/4$ in the form

$$\begin{aligned}
f_{jk}^{(1)} &= f_{jk}^{(2)} = 0\,, \quad \text{for} \quad j+k=2\,,\\
f_{30}^{(1)} &= f_{12}^{(1)} = f_{21}^{(2)} = f_{03}^{(2)} = \mathcal{E}\tfrac{3\alpha b_{3\mathrm{cr}}}{4(b_{1\mathrm{cr}})^3}\,\tfrac{\alpha}{\omega}\big(1+\tfrac{\omega^2}{\alpha^2}\big)\big(\omega+\tfrac{\omega}{\alpha}+\tfrac{\omega^3}{\alpha^2}\big)\,,\\
f_{21}^{(1)} &= f_{03}^{(1)} = -f_{30}^{(2)} = -f_{12}^{(2)} = \mathcal{E}\tfrac{3\alpha b_{3\mathrm{cr}}}{4(b_{1\mathrm{cr}})^3}\,\tfrac{\alpha}{\omega}\big(1+\tfrac{\omega^2}{\alpha^2}\big)\big(1+2\tfrac{\omega^2}{\alpha^2}\big)\,,\\
F_{jk}^{(1l)} &= F_{jk}^{(2l)} = 0\,,\\
F_{10}^{(1r)} &= \mathcal{E}\tfrac{2b_{2\mathrm{cr}}}{n(b_{1\mathrm{cr}})^2}\mathrm{R}^*\begin{bmatrix} \big(3+\alpha-\frac{\omega^2}{\alpha}\big)\widetilde{C} + \big(\frac{\alpha}{\omega}-2\omega-2\frac{\omega}{\alpha}\big)\widetilde{S} + \big(1+\alpha+\frac{\omega^2}{\alpha}\big)E \\ 0 \end{bmatrix},\\
F_{01}^{(1r)} &= \mathcal{E}\tfrac{2b_{2\mathrm{cr}}}{n(b_{1\mathrm{cr}})^2}\mathrm{R}^*\begin{bmatrix} -\big(\frac{\alpha}{\omega}-2\omega-2\frac{\omega}{\alpha}\big)\widetilde{C} + \big(3+\alpha-\frac{\omega^2}{\alpha}\big)\widetilde{S} + \big(\frac{\alpha}{\omega}+2\frac{\omega}{\alpha}\big)E \\ 0 \end{bmatrix},\\
F_{10}^{(2r)} &= \mathcal{E}\tfrac{2b_{2\mathrm{cr}}}{n(b_{1\mathrm{cr}})^2}\mathrm{R}^*\begin{bmatrix} -\big(\frac{\alpha}{\omega}-2\omega-2\frac{\omega}{\alpha}\big)\widetilde{C} + \big(3+\alpha-\frac{\omega^2}{\alpha}\big)\widetilde{S} - \big(\frac{\alpha}{\omega}+2\frac{\omega}{\alpha}\big)E \\ 0 \end{bmatrix},\\
F_{01}^{(2r)} &= \mathcal{E}\tfrac{2b_{2\mathrm{cr}}}{n(b_{1\mathrm{cr}})^2}\mathrm{R}^*\begin{bmatrix} -\big(3+\alpha-\frac{\omega^2}{\alpha}\big)\widetilde{C} - \big(\frac{\alpha}{\omega}-2\omega-2\frac{\omega}{\alpha}\big)\widetilde{S} + \big(1+\alpha+\frac{\omega^2}{\alpha}\big)E \\ 0 \end{bmatrix},\\
F_{jk}^{(3\mathrm{c})} &= F_{jk}^{(3\mathrm{s})} = 0\,,
\end{aligned} \tag{3.144}$$

$$
\begin{aligned}
F_{20}^{(3-)} &= F_{02}^{(3-)} = -\tfrac{b_{2\mathrm{cr}}}{(b_{1\mathrm{cr}})^2}\big(1+\tfrac{\omega^2}{\alpha^2}\big)\begin{bmatrix}0\\ E\end{bmatrix}, \\
F_{11}^{(3-)} &= 0\,, \\
F_{20}^{(3)} &= \tfrac{b_{2\mathrm{cr}}}{(b_{1\mathrm{cr}})^2}\begin{bmatrix}\big(1-\tfrac{\omega^2}{\alpha^2}\big)\widetilde{C}-2\tfrac{\omega}{\alpha}\widetilde{S}+\big(1+\tfrac{\omega^2}{\alpha^2}\big)E\\ 0\end{bmatrix}, \\
F_{11}^{(3)} &= \tfrac{2b_{2\mathrm{cr}}}{(b_{1\mathrm{cr}})^2}\begin{bmatrix}2\tfrac{\omega}{\alpha}\widetilde{C}+\big(1-\tfrac{\omega^2}{\alpha^2}\big)\widetilde{S}\\ 0\end{bmatrix}, \\
F_{02}^{(3)} &= \tfrac{b_{2\mathrm{cr}}}{(b_{1\mathrm{cr}})^2}\begin{bmatrix}-\big(1-\tfrac{\omega^2}{\alpha^2}\big)\widetilde{C}+2\tfrac{\omega}{\alpha}\widetilde{S}+\big(1+\tfrac{\omega^2}{\alpha^2}\big)E\\ 0\end{bmatrix},
\end{aligned}
$$

where we use the vectors $\widetilde{C}, \widetilde{S} \in \mathbb{R}^n$ defined by

$$
\widetilde{C} = \begin{bmatrix}\cos(\frac{4k\pi}{n}1)\\ \cos(\frac{4k\pi}{n}2)\\ \vdots\\ \cos(\frac{4k\pi}{n}n)\end{bmatrix}, \quad \widetilde{S} = \begin{bmatrix}\sin(\frac{4k\pi}{n}1)\\ \sin(\frac{4k\pi}{n}2)\\ \vdots\\ \sin(\frac{4k\pi}{n}n)\end{bmatrix}. \tag{3.145}
$$

Note that the cases $k = n/2$, $k = n/3$, and $k = n/4$ result in different formulae for the above coefficients, but the final Poincaré-Lyapunov constant will have the same formula as in the case of general wave number k. The detailed calculation of these 'resonant' cases is not presented here.

According to (3.144) $F_{jk}^{(3\mathrm{c})} = F_{jk}^{(3\mathrm{s})} = 0$ and one can show that

$$
\mathrm{R}\big(F_{20}^{(3-)} + F_{02}^{(3-)}\big) = 0\,, \quad (\mathrm{L}+\mathrm{R})F_{11}^{(3-)} = 0\,, \quad (\mathrm{L}+\mathrm{R})\big(F_{20}^{(3-)} - F_{02}^{(3-)}\big) = 0\,. \tag{3.146}
$$

Substituting these expressions into (3.92) the vectors $H_0, H_1, H_2 \in \mathbb{R}^{2n}$ satisfy

$$
\begin{bmatrix}\mathrm{L}+\mathrm{R} & 0 & 0\\ 0 & \mathrm{L}+\mathrm{R}\cos(2\omega) & 2\omega\mathrm{I}+\mathrm{R}\sin(2\omega)\\ 0 & -\big(2\omega\mathrm{I}+\mathrm{R}\sin(2\omega)\big) & \mathrm{L}+\mathrm{R}\cos(2\omega)\end{bmatrix}\begin{bmatrix}H_0\\ H_1\\ H_2\end{bmatrix} = -\frac{1}{2}\begin{bmatrix}F_{20}^{(3)}+F_{02}^{(3)}+F_{20}^{(3-)}+F_{02}^{(3-)}\\ F_{20}^{(3)}-F_{02}^{(3)}\\ F_{11}^{(3)}\end{bmatrix}. \tag{3.147}
$$

The $2n$-dimensional equation for H_0 is decoupled from the $4n$-dimensional equation for H_1, H_2 in (3.147). Note that since $(\mathrm{L}+\mathrm{R})$ is singular due to the translational symmetry

(3.122), the non-homogeneous equation for H_0 in (3.147) may seem not to be solvable. However, its right-hand side belongs to the image space of the coefficient matrix (L + R) due to the translational symmetry induced terms $F_{jk}^{(3-)}$. Without these extra terms, that is, without the elimination of the translational symmetry, the equation for H_0 would be unsolvable. Here we obtain the solution

$$H_0 = \tfrac{b_{2\mathrm{cr}}}{(b_{1\mathrm{cr}})^2}\big(1+\tfrac{\omega^2}{\alpha^2}\big)\begin{bmatrix} E \\ \kappa E \end{bmatrix}, \tag{3.148}$$

with the undetermined parameter κ. Note that even κ is unknown this solution is sufficient since only the quantities $H_{0,n+i+1} - H_{0,n+i} = 0$ are used in the calculations below.

At the same time, the non-homogeneous equation for H_1, H_2 in (3.147) is not effected by the vectors $F_{jk}^{(3-)}$. Using (3.115) this $4n$-dimensional equation leads to

$$\left.\begin{aligned} H_{1,i} &= -2\omega H_{2,n+i} \\ H_{2,i} &= 2\omega H_{1,n+i} \end{aligned}\right\} \quad \text{for} \quad i = 1,\dots,n\,, \tag{3.149}$$

and to the $2n$-dimensional equation

$$\begin{bmatrix} \mu\sin^2(\frac{k\pi}{n})\,\mathrm{I} - \cos(\frac{2k\pi}{n})\mathrm{A} & \nu\sin^2(\frac{k\pi}{n})\,\mathrm{I} - \sin(\frac{2k\pi}{n})\mathrm{A} \\ -\big(\nu\sin^2(\frac{k\pi}{n})\,\mathrm{I} - \sin(\frac{2k\pi}{n})\mathrm{A}\big) & \mu\sin^2(\frac{k\pi}{n})\,\mathrm{I} - \cos(\frac{2k\pi}{n})\mathrm{A} \end{bmatrix} H_\cup = -\tfrac{4b_{2\mathrm{cr}}}{\omega^2 b_{1\mathrm{cr}}}\sin^2(\tfrac{k\pi}{n})\begin{bmatrix} \widetilde{C} \\ \widetilde{S} \end{bmatrix}, \tag{3.150}$$

where the vector $H_\cup \in \mathbb{R}^{2n}$ is defined by

$$\left.\begin{aligned} H_{\cup,i} &= H_{1,n+i} \\ H_{\cup,n+i} &= H_{2,n+i} \end{aligned}\right\} \quad \text{for} \quad i = 1,\dots,n\,, \tag{3.151}$$

and

$$\mu = \frac{-\frac{16b_{1\mathrm{cr}}}{\alpha}\frac{\omega^2}{\alpha^2}}{\big(1+\frac{\omega^2}{\alpha^2}\big)^2}\,, \quad \nu = \frac{\frac{8b_{1\mathrm{cr}}}{\omega}\big(1+3\frac{\omega^2}{\alpha^2}\big)}{\big(1+\frac{\omega^2}{\alpha^2}\big)^2}\,. \tag{3.152}$$

The solution of (3.150) is given by

$$H_\cup = \frac{-\frac{4b_{2\mathrm{cr}}}{\omega^2 b_{1\mathrm{cr}}}}{\big(\nu - 4\cot(\frac{k\pi}{n})\big)^2 + \mu^2}\left(\mu\begin{bmatrix} \widetilde{C} \\ \widetilde{S} \end{bmatrix} + \big(\nu - 4\cot(\tfrac{k\pi}{n})\big)\begin{bmatrix} -\widetilde{S} \\ \widetilde{C} \end{bmatrix}\right), \tag{3.153}$$

which provides

$$
\begin{aligned}
H_1 &= \frac{\frac{4b_{2\mathrm{cr}}}{\omega^2 b_{1\mathrm{cr}}}}{\big(\nu - 4\cot(\frac{k\pi}{n})\big)^2 + \mu^2} \left(\big(\nu - 4\cot(\tfrac{k\pi}{n})\big) \begin{bmatrix} 2\omega\widetilde{C} \\ \widetilde{S} \end{bmatrix} + \mu \begin{bmatrix} 2\omega\widetilde{S} \\ -\widetilde{C} \end{bmatrix} \right) , \\
H_2 &= \frac{\frac{4b_{2\mathrm{cr}}}{\omega^2 b_{1\mathrm{cr}}}}{\big(\nu - 4\cot(\frac{k\pi}{n})\big)^2 + \mu^2} \left(\big(\nu - 4\cot(\tfrac{k\pi}{n})\big) \begin{bmatrix} 2\omega\widetilde{S} \\ -\widetilde{C} \end{bmatrix} - \mu \begin{bmatrix} 2\omega\widetilde{C} \\ \widetilde{S} \end{bmatrix} \right) .
\end{aligned}
\tag{3.154}
$$

Now, using these in (3.87) and (3.91) we can calculate $w(-1)$. Substituting $w(-1)$ into the first two equations of (3.86), we obtain the form (3.93) where the coefficients $f_{jk}^{(1)}$ and $f_{jk}^{(2)}$ have already been determined by (3.144), while the coefficients

$$
\begin{aligned}
g_{30}^{(1)} &= g_{12}^{(1)} = g_{21}^{(2)} = g_{03}^{(2)} \\
&= \frac{\mathcal{E}\frac{2\alpha(b_{2\mathrm{cr}})^2}{(b_{1\mathrm{cr}})^4}\cot(\frac{k\pi}{n})}{\big(\nu - 4\cot(\frac{k\pi}{n})\big)^2 + \mu^2} \frac{\alpha}{\omega}\big(1 + \tfrac{\omega^2}{\alpha^2}\big) \Big(\big(\nu - 4\cot(\tfrac{k\pi}{n})\big)\big(\omega + \tfrac{\omega}{\alpha} + \tfrac{\omega^3}{\alpha^2}\big) + \mu\big(1 + 2\tfrac{\omega^2}{\alpha^2}\big) \Big) , \\
g_{21}^{(1)} &= g_{03}^{(1)} = -g_{30}^{(2)} = -g_{12}^{(2)} \\
&= \frac{\mathcal{E}\frac{2\alpha(b_{2\mathrm{cr}})^2}{(b_{1\mathrm{cr}})^4}\cot(\frac{k\pi}{n})}{\big(\nu - 4\cot(\frac{k\pi}{n})\big)^2 + \mu^2} \frac{\alpha}{\omega}\big(1 + \tfrac{\omega^2}{\alpha^2}\big) \Big(\big(\nu - 4\cot(\tfrac{k\pi}{n})\big)\big(1 + 2\tfrac{\omega^2}{\alpha^2}\big) - \mu\big(\omega + \tfrac{\omega}{\alpha} + \tfrac{\omega^3}{\alpha^2}\big) \Big) ,
\end{aligned}
\tag{3.155}
$$

originate in the terms involving $w(-1)$. The trigonometric identities (A.4)–(A.15) of the Appendix has been used to determine (3.155). Note that $w(0)$ also appears in the first two equations of (3.86) but in our case its coefficients are all zeros, i.e., $F_{jk}^{(1l)} = F_{jk}^{(2l)} = 0$ (see (3.144)). The Poincaré-Lyapunov constant is determined by the Bautin formula (3.94), which provides

$$
\begin{aligned}
\Delta &= \mathcal{E}\tfrac{\alpha}{4(b_{1\mathrm{cr}})^3} \tfrac{\alpha}{\omega}\big(1 + \tfrac{\omega^2}{\alpha^2}\big)\big(\omega + \tfrac{\omega}{\alpha} + \tfrac{\omega^3}{\alpha^2}\big) \\
&\quad \times \frac{1}{2} \left(6b_{3\mathrm{cr}} + \frac{(2b_{2\mathrm{cr}})^2}{b_{1\mathrm{cr}}} \frac{4\cot(\frac{k\pi}{n})}{\big(\nu - 4\cot(\frac{k\pi}{n})\big)^2 + \mu^2} \left(\nu - 4\cot(\tfrac{k\pi}{n}) + \mu \frac{1 + 2\frac{\omega^2}{\alpha^2}}{\omega + \frac{\omega}{\alpha} + \frac{\omega^3}{\alpha^2}} \right) \right) .
\end{aligned}
\tag{3.156}
$$

The bifurcation is supercritical for negative and subcritical for positive values of Δ. However in order to decide its sign further analysis is required.

3.3.3 Analysis and interpretation of results

We now investigate (3.156) in order to determine its sign. We found that $\Delta > 0$ is always true when $\frac{k}{n} \ll 1$ which is the case for real traffic situations (many vehicles n with a few waves k). This can be proven as is detailed below.

The first part of the expression (3.156) of Δ in front of the parenthesis is always positive since $\mathcal{E}, b_{1\mathrm{cr}}, \alpha, \omega > 0$. Within the parenthesis in (3.156), the first term is positive since (3.114) implies $b_{1\mathrm{cr}} = \mathrm{V}'(h^*_{\mathrm{cr}}) < 1/2$, which yields critical average headway values h^*_{cr} such that $6b_{3\mathrm{cr}} = \mathrm{V}'''(h^*_{\mathrm{cr}}) > 0$; see Fig. 3.3(b) and (d). The second term in the parenthesis in (3.156) contains the ratio of two complicated expressions, which, by using (3.114) and (3.152), can be rearranged in the form

$$\begin{aligned}
&4\cot(\tfrac{k\pi}{n})\Big(\nu - 4\cot(\tfrac{k\pi}{n}) + \mu\frac{1+2\frac{\omega^2}{\alpha^2}}{\omega+\frac{\omega}{\alpha}+\frac{\omega^3}{\alpha^2}}\Big)\\
&= \big(4\cot(\tfrac{k\pi}{n})\big)^2\Big(\frac{\big(1+\frac{\omega^2}{\alpha^2}\big)\big(\omega+\frac{\omega}{\alpha}+3\frac{\omega^3}{\alpha^2}\big)-4\frac{\omega^5}{\alpha^5}}{\big(\cos\omega-\frac{\omega}{\alpha}\sin\omega\big)\big(1+\frac{\omega^2}{\alpha^2}\big)\big(\omega+\frac{\omega}{\alpha}+\frac{\omega^3}{\alpha^2}\big)}-1\Big)\\
&:= \big(4\cot(\tfrac{k\pi}{n})\big)^2\mathcal{N}(\omega,\alpha)\,,
\end{aligned} \tag{3.157}$$

and

$$\begin{aligned}
&\big(\nu-4\cot(\tfrac{k\pi}{n})\big)^2+\mu^2\\
&= \big(4\cot(\tfrac{k\pi}{n})\big)^2\Big(\frac{\big(1+\frac{\omega^2}{\alpha^2}\big)\big(1+4\frac{\omega^2}{\alpha^2}\big)-2\big(\cos\omega-\frac{\omega}{\alpha}\sin\omega\big)\big(1+3\frac{\omega^2}{\alpha^2}\big)}{\big(\cos\omega-\frac{\omega}{\alpha}\sin\omega\big)^2\big(1+\frac{\omega^2}{\alpha^2}\big)}+1\Big)\\
&:= \big(4\cot(\tfrac{k\pi}{n})\big)^2\mathcal{D}(\omega,\alpha) > 0\,.
\end{aligned} \tag{3.158}$$

Since (3.158) is always positive, the sign of (3.157) is crucial for deciding the overall sign of Δ. According to (3.114) we have $\omega \in (0, \frac{k\pi}{n})$, that is, the realistic case $\frac{k}{n} \ll 1$ implies the oscillation frequency $\omega \ll 1$.

Fig. 3.4(a) shows the numerator $\mathcal{N}(\omega,\alpha)$ for some values of α. One can observe that $\mathcal{N}(\omega,\alpha) > 0$ for $\omega \ll 1$. Note that if $\alpha \to 0$ then $\mathcal{N}(\omega,\alpha)$ may become negative (see Fig. 3.4(a) for $\alpha = 0.5$), but this is a physically unrealistic case where drivers intend to reach their desired speed v^0 extremely slowly.

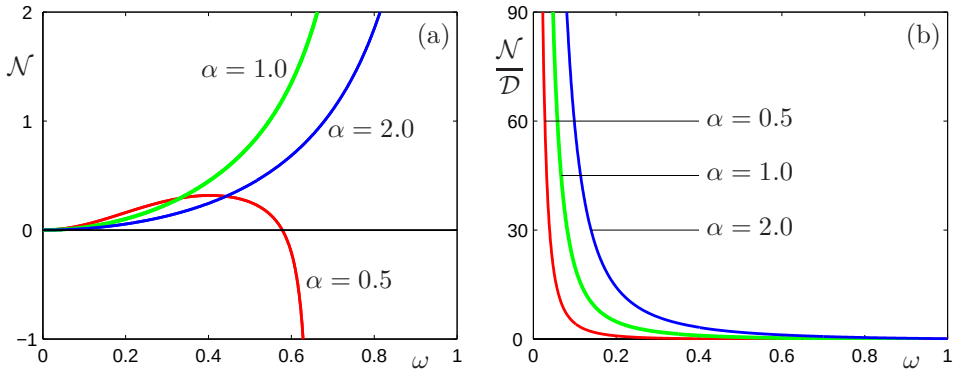

Fig. 3.4: Quantities defined by (3.157) and (3.158) as a function of the frequency ω, for representative values of the parameter α. In panel (a) the numerator $\mathcal{N}(\omega, \alpha)$ is depicted, while panel (b) shows the ratio $\mathcal{N}(\omega, \alpha)/\mathcal{D}(\omega, \alpha)$.

Moreover, the ratio of (3.157) and (3.158), $\mathcal{N}(\omega, \alpha)/\mathcal{D}(\omega, \alpha)$, is not only positive for $\omega \ll 1$ but also $\mathcal{N}(\omega, \alpha)/\mathcal{D}(\omega, \alpha) \to \infty$ when $\omega \to 0$ (i.e., when $n \to \infty$) as shown in Fig. 3.4(b). This feature provides robustness for subcriticality. Note that subcriticality also occurs for optimal velocity functions different from (1.24), e.g., for (1.25) and (1.26).

According to the general expression (3.95), by using definition (3.104), formulae (3.116) and (3.120), and expressions (3.156)–(3.158), the amplitude v_{amp} of the unstable oscillations is obtained in the form

$$\begin{aligned} v_{\text{amp}} &= \sqrt{-\frac{\text{Re}\left(\lambda_1'(h_{\text{cr}}^*)\right)}{\Delta}(h^* - h_{\text{cr}}^*)} \\ &= \frac{\omega}{\sin(\frac{k\pi}{n})} \sqrt{-\frac{2\text{V}''(h_{\text{cr}}^*)}{\text{V}'''(h_{\text{cr}}^*) + \frac{\left(\text{V}''(h_{\text{cr}}^*)\right)^2}{\text{V}'(h_{\text{cr}}^*)}\frac{\mathcal{N}(\omega,\alpha)}{\mathcal{D}(\omega,\alpha)}}(h^* - h_{\text{cr}}^*)}\,. \end{aligned} \tag{3.159}$$

Note that zero reaction time delay results in $\mathcal{N}(\omega, \alpha)/\mathcal{D}(\omega, \alpha) \equiv -1$ as shown in [39]. In that case subcriticality appears only for extremely high values of the desired speed v^0 when the term $6b_{3\text{cr}}$ becomes greater than $(2b_{2\text{cr}})^2/b_{1\text{cr}}$ at the critical points (of the non-delayed model). Consequently, the presence of the drivers' reaction time delay has an essential role in the robustness of the subcritical nature of the Hopf bifurcation. This subcriticalty explains how traffic waves can be formed when the uniform flow equilibrium is stable. Large perturbations

may not decay but rather push the system 'outside' the unstable periodic solution.

In correspondence with (3.97) the unstable periodic motion can be written as

$$y(t) = v_{\text{amp}}\big(S_1 \cos(\omega t) - S_2 \sin(\omega t)\big)\,, \tag{3.160}$$

where the vectors S_1 and S_2 are given in (3.134). Substituting these vectors into (3.160) and using definitions (3.102) and (3.105), one can determine the velocity

$$\dot{x}_i(t) = v^* + \dot{x}_i^{\text{p}}(t) = v^* + v_{\text{amp}} \cos\big(\tfrac{2\pi k}{n} i + \omega t\big)\,, \quad i = 1, \ldots, n\,. \tag{3.161}$$

(Compare (3.161) with (3.15) but note that the linear analysis in Section 3.1 did not provide v_{amp}.) Formula (3.161) describes a wave travelling opposite to the vehicle flow with spatial wave number k (i.e., with spatial wavelength $L/k = h^* n/k$), and the corresponding wave speed is given by (3.18).

In order to check the reliability of the Poincaré-Lyapunov constant (3.156) and the amplitude estimation (3.159), we compare these analytical results with those obtained by numerical continuation techniques with the package DDE-BIFTOOL [36]. (More detailed continuation results can be found in Chapter 4).

Fig. 3.5 demonstrates the subcriticality for $n = 9$ cars. The horizontal axis corresponds to the uniform flow equilibrium, that is, stable for small and large values of h^* (shown by green solid line) but unstable for intermediate values of h^* (shown by red dashed line). This corresponds to (3.10),(3.114) and to the horizontal cross section of Fig. 3.2(f) at $\alpha = 1.0$. The Hopf bifurcations are marked by blue stars ($*$). The branches of the analytically calculated unstable periodic motions with amplitudo (3.159) are shown by red dashed curves. The gray curves show the numerical continuation results obtained by DDE-BIFTOOL. Gray solid curves represent stable oscillations while gray dashed curves represent unstable ones. The fold bifurcation points are marked by gray crosses ($\times$).

The comparison of the analytical and numerical results shows that the analytical approximation of the unstable oscillations is quantitatively reliable in the vicinity of the Hopf bifurcation points. However, the size of this neighbourhood is not provided by the analytical

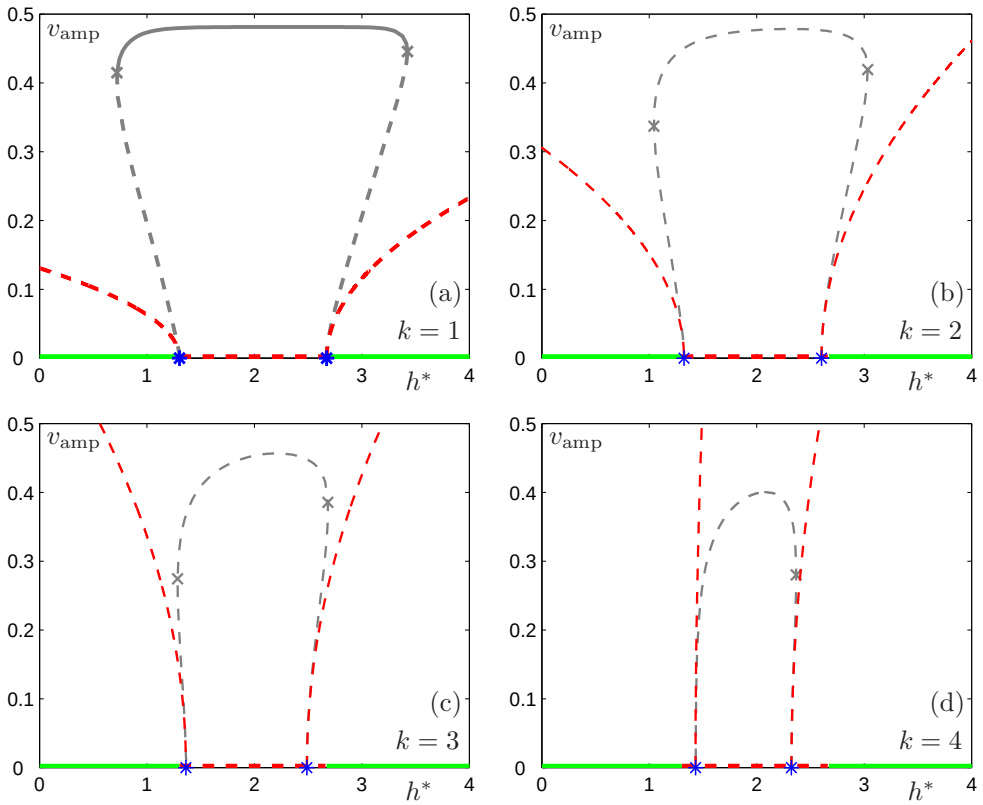

Fig. 3.5: The amplitude v_{amp} of velocity oscillations as a function of the average headway parameter h^* in case of $n = 9$ cars, for wave numbers $k = 1$ (a), $k = 2$ (b), $k = 3$ (c), and $k = 4$ (d); the desired speed is $v^0 = 1.0$ and the sensitivity is $\alpha = 1.0$. The horizontal axis ($v_{\text{amp}} \equiv 0$) represents the uniform flow equilibrium. The analytical results are coloured: green solid and red dashed curves represent stable and unstable branches, respectively, and blue stars ($*$) stand for Hopf bifurcations. Gray curves correspond to numerical continuation results: solid and dashed curves refer to stable and unstable states and gray crosses ($\times$) represent fold bifurcations.

approach. Qualitatively we obtain the correct behaviour up to the fold bifurcation points, but those bifurcations cannot be detected by the method above. To explore the full nonlinear behaviour of the system we use continuation techniques in Chapter 4.

We found that the Hopf bifurcations are all robustly subcritical for any wave number k (except for large $\frac{k}{n} \simeq 1/2$; see Fig. 3.5(d)). Note that analytical and numerical results agree better as the wave number k is increased because the oscillations become more harmonic.

For wave number $k = 1$ the oscillation branch becomes stable between the two fold bifur-

cation points; see Fig. 3.5(a). The corresponding *stop-and-go oscillations* include travelling with low velocity (practically zero) and travelling with high velocity (close to the desired speed v^0). Wide regions of bistability can be observed between the Hopf and the fold bifurcation points on both sides of the unstable equilibrium. In such domains, for a perturbation 'smaller' than the unstable oscillation, the system approaches the uniform flow equilibrium. If a larger perturbation is applied then the system develops a spatial *stop-and-go wave* which propagates against the traffic flow. In reality these large perturbations might be caused, for example, by a slower vehicle (such us a lorry) changing lanes.

As was mentioned in Section 3.1, the wave numbers $k > 1$ are related to Hopf bifurcations in the parameter region where the uniform flow equilibrium is already unstable. This also means that the corresponding oscillations for $k > 1$ are unstable independently of the criticality of these Hopf bifurcations; see Fig. 3.5(b)–(d). Also the oscillation branch remains unstable between the fold bifurcation points. Thus, the only stable oscillating state is the stop-and-go motion for $k = 1$, but several unstable solutions co-exist.

In the analytical calculation we used a third degree approximation of the nonlinearities which gives the correct subcritical behaviour and consequently the possibility of bistability. However, this approximation is not able to find fold bifurcations of periodic solutions and the consequent stable oscillations. To find this global behaviour, one needs to investigate the full nonlinear dynamics by using numerical continuation techniques.

Chapter 4

Numerical bifurcation analysis

In the previous chapter we examined how the uniform flow equilibrium (1.16),(1.18) can lose its stability through Hopf bifurcations when parameters are changed. A detailed study of the Hopf curves was given in Section 3.1. In Section 3.3, the stability and amplitude of the resulting periodic solutions were also determined close to the Hopf bifurcation points. We are now interested in what happens to the branches of periodic solutions far from the Hopf bifurcation points, i.e., in the global dynamics of the system (1.6),(1.23).

The global dynamics of the optimal velocity model (1.23) was probed by numerical simulation in [29]. In contrast, we use numerical continuation techniques to perform a bifurcation analysis of this model. This methodology enables us to calculate efficiently branches of periodic solutions (corresponding to traffic jams) far from the uniform flow equilibrium, and to classify regions of parameter space where the equilibrium is stable yet co-exists with other non-trivial stable solutions. In such bistable regions of parameter space, the choice of initial conditions determines which traffic behaviour is selected as time $t \to \infty$.

The basic idea is to find a bifurcation (in our case the Hopf bifurcation of the uniform flow equilibrium) and then follow or continue the bifurcating solution (in our case the periodic solution) as a parameter is changed (in our case the average headway). While it is not as straightforward as numerical simulation, numerical continuation is a powerful tool in that

it allows one to map out the dynamics of a system in a systematic and efficient way. This approach is well established for systems modelled by ODEs and has been applied successfully in many application areas; see, e.g., [47, 73] as entry points to the extensive literature. The non-delayed model (1.13) has recently been investigated by Berg and Wilson [19], and by Gasser *et al.* [39] with the help of the continuation the package AUTO [32].

In this work, dealing with a system with delay results in additional technical difficulties, due to the fact that the phase space of a DDE is infinite dimensional. For example, as described in Sections 2.2 and 3.2.2 the linearizations around steady states and oscillating solutions are infinite-dimensional operators (rather than matrices for the finite-dimensional ODE-case). This means that standard continuation software for ODEs, such as AUTO [32], cannot be used. However, recently, the package DDE-BIFTOOL, which works under Matlab, was developed by Engelborghs *et al.* [35, 36]; see Section 2.4 for details. This software uses truncated matrices of appropriate sizes instead of infinite-dimensional operators, and is able to find and follow equilibria and oscillating solutions of DDEs, even when they are unstable. Further, it allows one to detect local bifurcations, where a solution changes its stability. For example, in our model we are able to find the Hopf bifurcation (where small amplitude oscillations are born) and the fold bifurcation of oscillating solutions (when two oscillating solutions of different stabilities merge and disappear). Note that in contrast to AUTO, DDE-BIFTOOL has not yet been used extensively in applications; its principal use so far has been in the study of semiconductor laser systems; see Green & Krauskopf [43] and Haegeman *et al.* [48].

The structure of this chapter is as follows. In Section 4.1 we display the branches of periodic solutions as a function of the average headway parameter h^* for several fixed values of the other parameters, namely the sensitivity α, the desired speed v^0, and the number of cars n. In Section 4.2 we examine the structure of periodic orbits at particular points on the computed branches. Finally, in Section 4.3 we present two-dimensional bifurcation diagrams in the headway-sensitivity (h^*, α) plane, for different fixed values of v^0 and n, thus representing the dynamics in a concise way. In such diagrams regions of phenomena such as

co-existence, collision and stopping are indicated. The material presented in this chapter is contained in the articles [85, 88, 89].

4.1 One-parameter continuation of periodic solutions

In this section we follow branches of oscillating solutions and detect bifurcations when using the average headway h^* as the bifurcation parameter. During this branch-following, the values of the parameters α, v^0, and n are fixed. We indicate the dependence of the dynamics on α, v^0, and n by performing the continuation analysis for a small collection of representative values. We investigate the dynamics using the smooth optimal velocity function (1.24) with fixed scaling parameter $s = 1$ (blue solid curve in Fig. 1.6). Note that only quantitative, not qualitative changes are caused by changing s. Furthermore, to avoid the singularities due to the translational symmetry we use the constraint (1.15) to define the headway h_n of the nth car with the headways h_i, $i = 1, \ldots, n-1$ of the other vehicles according to

$$h_n(t) = L - \sum_{i=1}^{n-1} h_i(t)\,. \tag{4.1}$$

Thus we reduce the number of equations to $2n-1$ in the studied delayed system (1.6),(1.23).

Throughout, the bifurcating branches of oscillating solutions are represented by the amplitude of oscillation of the vehicles' velocities

$$v_{\text{amp}} = \big(\max_t v(t) - \min_t v(t)\big)/2\,. \tag{4.2}$$

In such pictures the horizontal axis is the average headway h^* and the vertical axis displays the solution norm defined by (4.2). For the uniform flow equilibria we have $v_{\text{amp}} = 0$, since $v(t) \equiv \max_t v(t) \equiv \min_t v(t)$ according to (1.16). Note that for the periodic solutions v_{amp} is the same for each car. This is a direct consequence of the $\mathbb{Z}_n$ symmetry of the system (i.e., each driver has the same characteristics), which implies that

$$\begin{aligned} v_i(t) &= v_{i+1}\big(t - \tfrac{k}{n}T_{\text{p}}\big)\,, \quad h_i(t) = h_{i+1}\big(t - \tfrac{k}{n}T_{\text{p}}\big)\,, \quad i = 1, \ldots, n-1 \\ v_n(t) &= v_1\big(t - \tfrac{k}{n}T_{\text{p}}\big)\,, \qquad h_n(t) = h_1\big(t - \tfrac{k}{n}T_{\text{p}}\big)\,, \end{aligned} \tag{4.3}$$

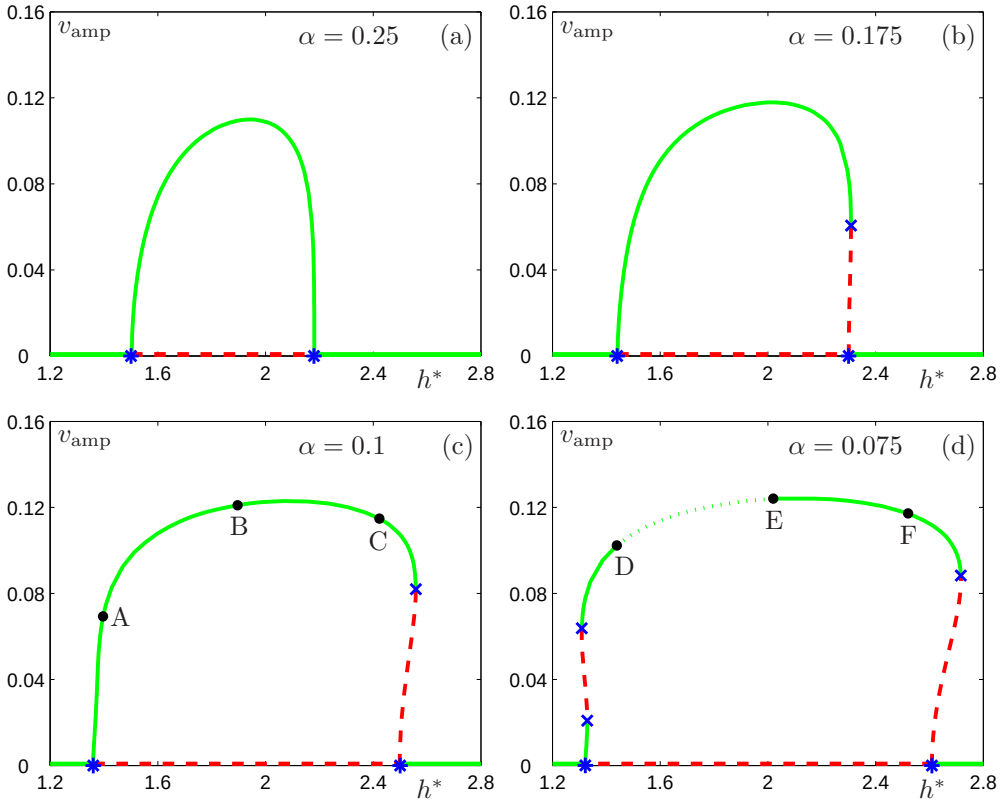

Fig. 4.1: The amplitude $v_{\rm amp}$ of velocity oscillations as a function of the average headway parameter h^* for $v^0 = 0.35$ in the case of $n = 3$ cars. The horizontal axis represents the equilibrium state. Green solid curves denote stable, and red dashed curves denote unstable states; the dotted curve represents the collision region. Hopf bifurcations are depicted as blue stars ($*$) and fold bifurcations as blue crosses ($\times$). The value of α is given in each panel (a)–(d).

for the periodic solutions, where $T_{\rm p}$ is the period. In other words, it is sufficient to plot the profile of, say, the first car; the profiles for all other cars are simply time-shifted copies as it was expressed by (3.15) and (3.161) for the weakly nonlinear oscillations. Note that in the case of k waves on the ring the time $k\,T_{\rm p}$ is smaller than the time needed for driving around the circular road, since the waves move in the upstream direction (against the flow of traffic).

The continuation results are shown in Figs. 4.1–4.5, where green solid curves denote stable solutions whereas red dashed curves denote unstable solutions. (Dotted sections of the green curves correspond to collision of vehicles as explained in detail in Section 4.2.) Hopf bifurcations of the uniform flow equilibrium are denoted by blue stars ($*$), and fold

bifurcations of the periodic solution are denoted by blue crosses (x). The branch of equilibria is unstable between the two outermost Hopf bifurcation points, in accordance with the results of Section 3.1.

As mentioned above, we use h^* as the bifurcation parameter and continue the branches of periodic orbits for different fixed values of the other parameters α, v^0, and n. Firstly, the investigation is restricted to the unrealistic setting of $n = 3$ cars for proof-of-concept purposes and qualitative changes to the branches are studied as α and v^0 are changed. Then we fix α and v^0 and study the trends for increasing numbers of cars n.

Let us consider the case $n = 3$ and first concentrate on the continuation results when the parameter α is changed and we fix $v^0 = 0.35$. This value gives qualitatively the stability behaviour shown in Fig. 3.1(b). For large values of α the two Hopf bifurcations are supercritical, as shown in Fig. 4.1(a). The computation of the bifurcating periodic solution shows a stable oscillation branch above the unstable part of the equilibrium. We remark that the unstable regime of the equilibrium disappears for very large α (see Fig. 3.1(b)): the two Hopf bifurcation points coalesce and disappear, leaving the equilibrium stable for all h^*.

As we decrease α, the right Hopf point becomes subcritical, i.e., the right-hand side of the branch of oscillating solutions becomes unstable. Where the stable and unstable parts meet, a fold bifurcation takes place (marked by blue cross (x)), as depicted in Fig. 4.1(b). Hence, a bistable regime appears to the right of the right-most Hopf point, which means that in the initial value problem, solutions tend either to the equilibrium or to the oscillatory state, depending on the initial condition. When decreasing α further, the branch of oscillating solutions grows, as is visualised in Fig. 4.1(c), and the bistable regime becomes wider.

As we reduce α further, an unstable section appears on the left-hand side of the branch of oscillating solutions (new dashed section) bounded by two fold bifurcations. This results in a second bistable regime in the parameter h^*, where two different stable oscillations co-exist, one with a smaller and one with a larger amplitude. As α is decreased further, the lower fold point tends to the left Hopf point, but does not reach it even when α is close to zero.

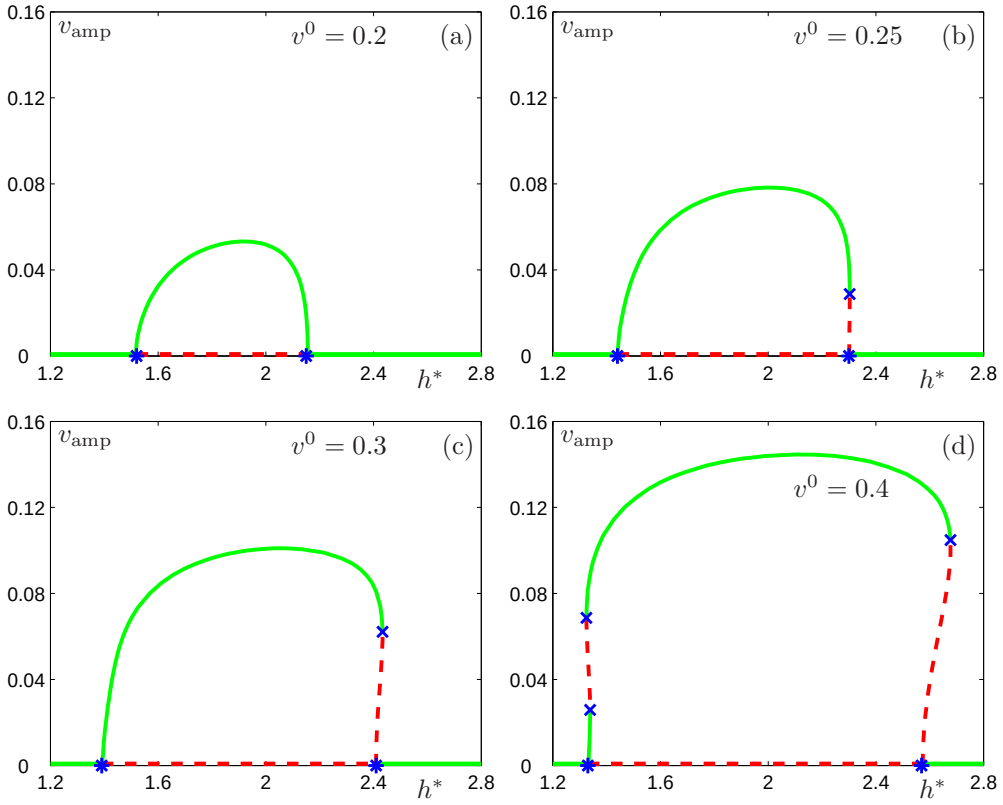

Fig. 4.2: The amplitude v_{amp} of velocity oscillations as a function of the average headway parameter h^* for $\alpha = 0.1$ in the case of $n = 3$ cars. The horizontal axis represents the equilibrium state. Green solid curves denote stable, and red dashed curves denote unstable states. Hopf bifurcations are depicted as blue stars ($*$) and fold bifurcations as blue crosses ($\times$). The value of v^0 is given in each panel (a)–(d).

The height of the branch of oscillating solutions changes roughly proportionally with v^0, because drivers want to reach the desired speed even during oscillations. Fixing $\alpha = 0.1$ and changing v^0, we obtain a series of bifurcation diagrams shown in Fig. 4.2. When increasing v^0, we observe the same qualitative changes as in Fig. 4.1. In fact, a high desired speed, (possibly corresponding to a high speed limit), can cause the onset of oscillations, independently of changes in other parameters.

Now we present the results for increased values of the desired speed $v^0 = 1.0$ to discover a different type of bifurcation behaviour. This value of v^0 gives qualitatively the stability behaviour as shown in Fig. 3.1(c), i.e., linear instability cannot be avoided by increasing α.

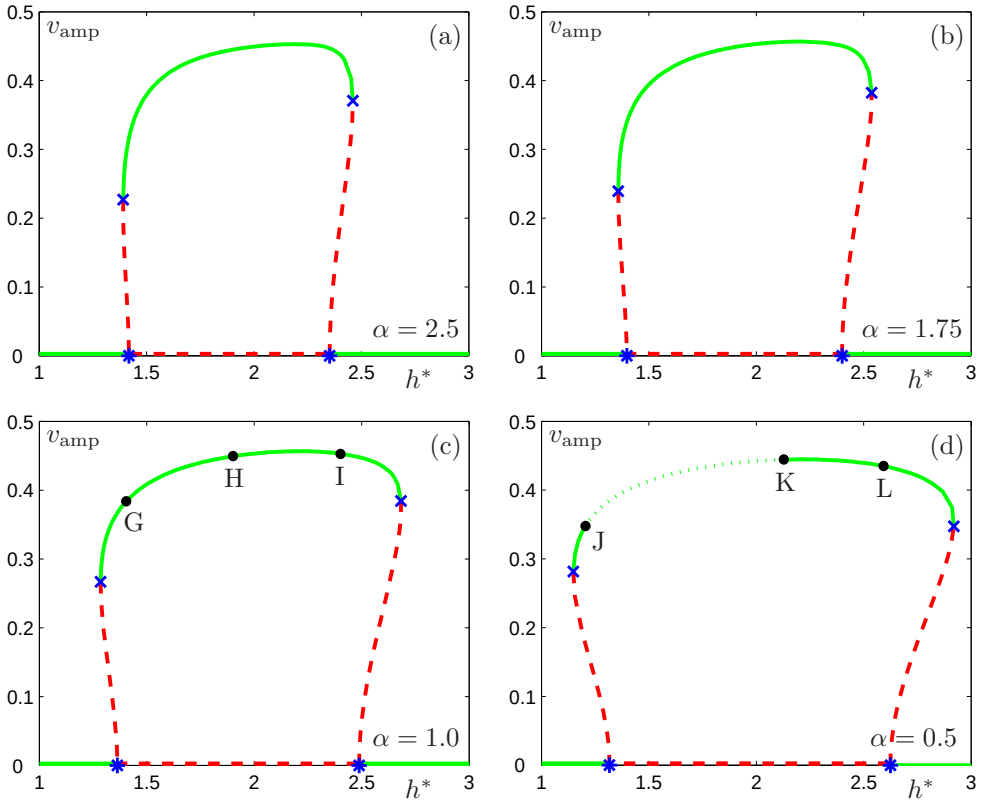

Fig. 4.3: The amplitude v_{amp} of velocity oscillations as a function of the average headway parameter h^* for $v^0 = 1.0$ in the case of $n = 3$ cars. The horizontal axis represents the equilibrium state. Green solid curves denote stable, and red dashed curves denote unstable states; the dotted curve represents the collision region. Hopf bifurcations are depicted as blue stars ($*$) and fold bifurcations as blue crosses ($\times$). The value of α is given in each panel (a)–(d).

If we change α for this value of v^0, then the plots shown in Fig. 4.3 are obtained. On both sides of the branch of oscillating solutions, the same type of bistability appears, namely an unstable section of the branch of oscillating solutions between a fold and a subcritical Hopf bifurcation. This behaviour is robust, that is, it does not change qualitatively when α is tuned, but the size of the bistability region increases by decreasing α.

Our aim is now to extend the results to larger n, and in particular to draw out the trends which may emerge as n is increased towards numbers that are more representative of real traffic situations. For simplicity we fix $\alpha = 1.0$ and $v^0 = 1.0$ throughout.

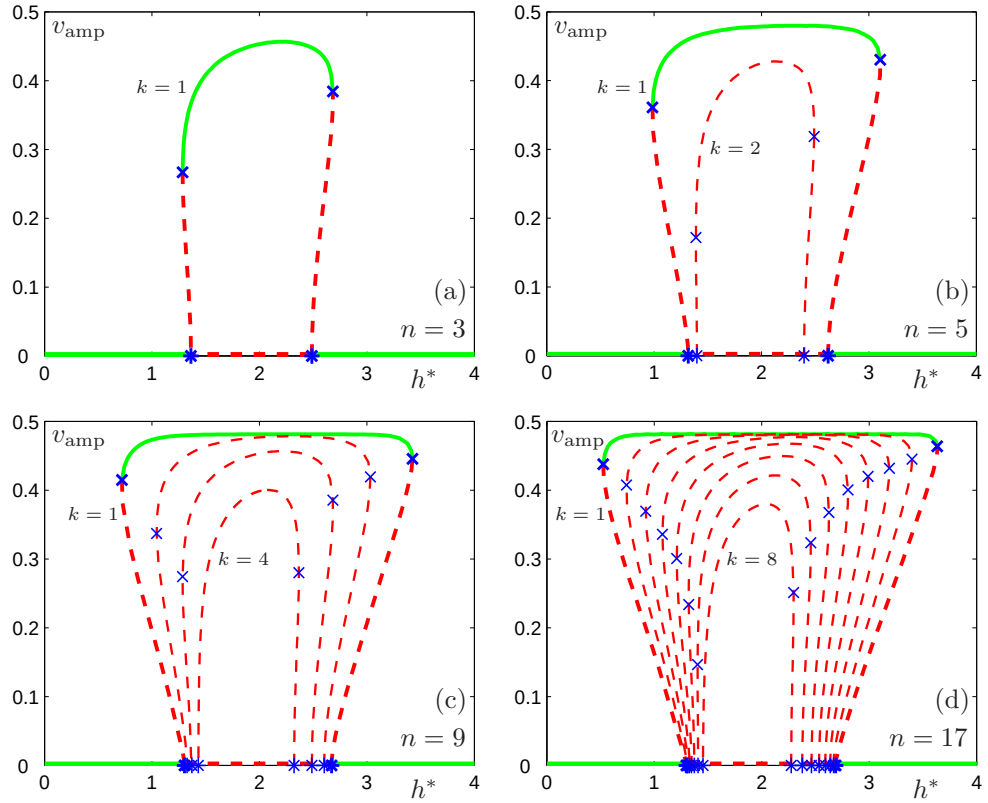

Fig. 4.4: The amplitude v_{amp} of velocity oscillations as a function of the average headway parameter h^* for $n = 3$ (a), $n = 5$ (b), $n = 9$ (c), and $n = 17$ cars (d); the desired speed is $v^0 = 1.0$ and the sensitivity is $\alpha = 1.0$. Stable states are represented by green solid curves, while unstable states by red dashed curves. Hopf bifurcations are depicted as blue stars ($*$) and fold bifurcations as blue crosses ($\times$).

The one-parameter continuation results are presented in Fig. 4.4 for $n = 3$, $n = 5$, $n = 9$, and $n = 17$ cars. Note that for simplicity we consider only odd numbers of cars. For even numbers of cars the situation is rather similar although there are some differences even at the level of linear stability, as is described in Section 3.1.2. Indeed the uniform flow equilibrium is stable for large and small values of h^* in accordance with Fig. 3.2(f). The branches of periodic solutions connect the subcritical Hopf bifurcation points and they are strictly ordered so that the branch for $k = 1$ is the outermost and the branch for $k = (n - 1)/2$ is the innermost. The only non-trivial stable solutions are those 'at the top' of the $k = 1$ branch, between the fold bifurcation points.

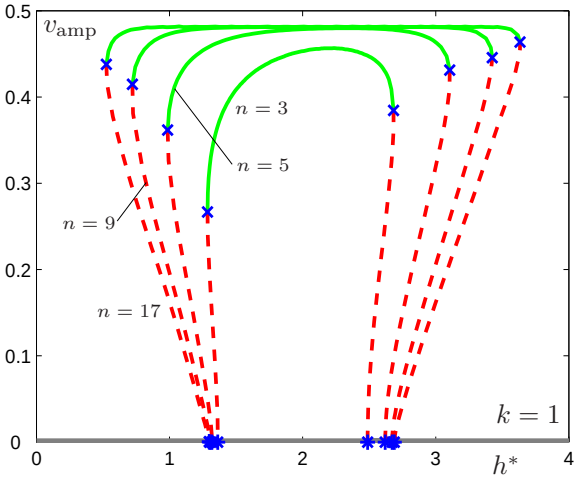

Fig. 4.5: The $k = 1$ branches from Fig. 4.4 of periodic solutions for $n = 3$, $n = 5$, $n = 9$, and $n = 17$ cars. Stable states are represented by green solid curves, while unstable states by red dashed curves. Hopf bifurcations are depicted as blue stars ($*$) and fold bifurcations as blue crosses ($\times$).

Images similar to Fig. 4.4 can be found in [39] for the OV model [15] without delay. However, in our case, the Hopf bifurcations are robustly subcritical due to the delay, which was proven using normal form calculations in Section 3.3.3. Consequently, the branches for different k are much more pronounced and there are wide regions of bistability (for $k = 1$) and co-existence (for $k > 1$). This bistable behavior for $k = 1$ was also found in a first-order delayed model [58].

Note that there appear to be two types of convergence on the level of the one-parameter bifurcation diagrams. Firstly, Fig. 4.4 is partial evidence that, as n gets larger and larger, the branch for any fixed $k > 1$ converges, in the pseudonorm defined by (4.2), to the $k = 1$ branch. Consequently, one might conclude that for $k = k^* > 1$ and n/k^* sufficiently large, the $k = k^*$ and $k = 1$ branches have significant structural features in common. Secondly, as is illustrated in Fig. 4.5, it appears that, as n is increased (through $n = 3, 5, 9, 17$), the $k = 1$ branch tends to a limit curve. This limiting behaviour is indicative of travelling wave dynamics, since the system, in the large n limit, does not 'feel' (over intermediate time scales) that it is subject to periodic boundary conditions.

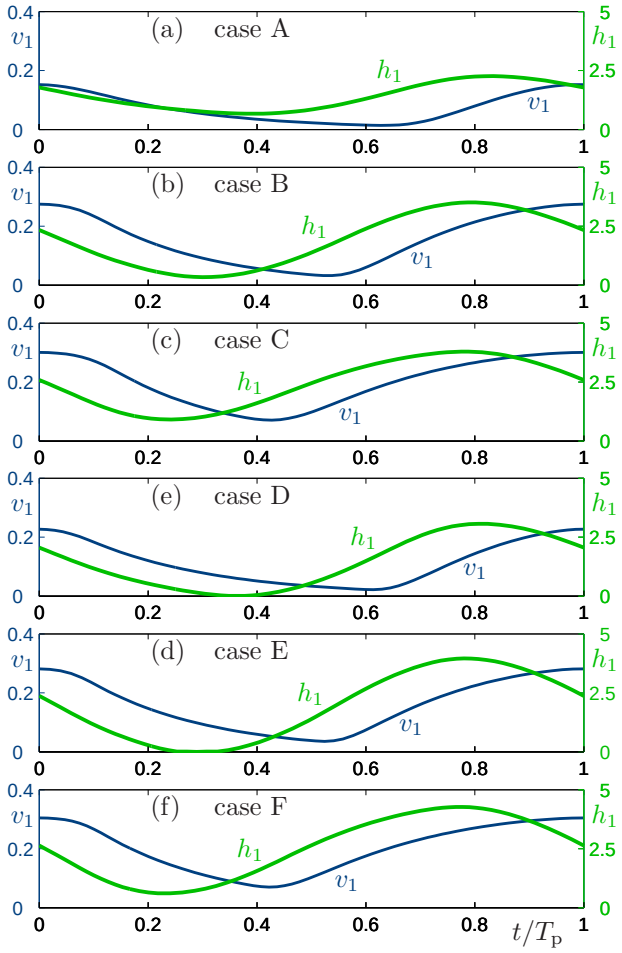

Fig. 4.6: Oscillations of the velocity v_1 of the first car over one period are shown in dark blue to the scale on the left; oscillations of the headway h_1 of the first car over one period are shown in green to the scale on the right. Cases A–F correspond to the marks in Fig. 4.1.

4.2 Time plots and structure of periodic solutions

We now consider how the features of the one-parameter bifurcation diagrams manifest themselves in the profiles of the associated oscillations. We examine the effects of changes in parameters first in the case study of $n = 3$ vehicles, and we introduce of the phenomena of collision and stopping. Then we study how the structure of the oscillations changes as the number of cars n is increased and *stop-fronts* and *go-fronts* are formed.

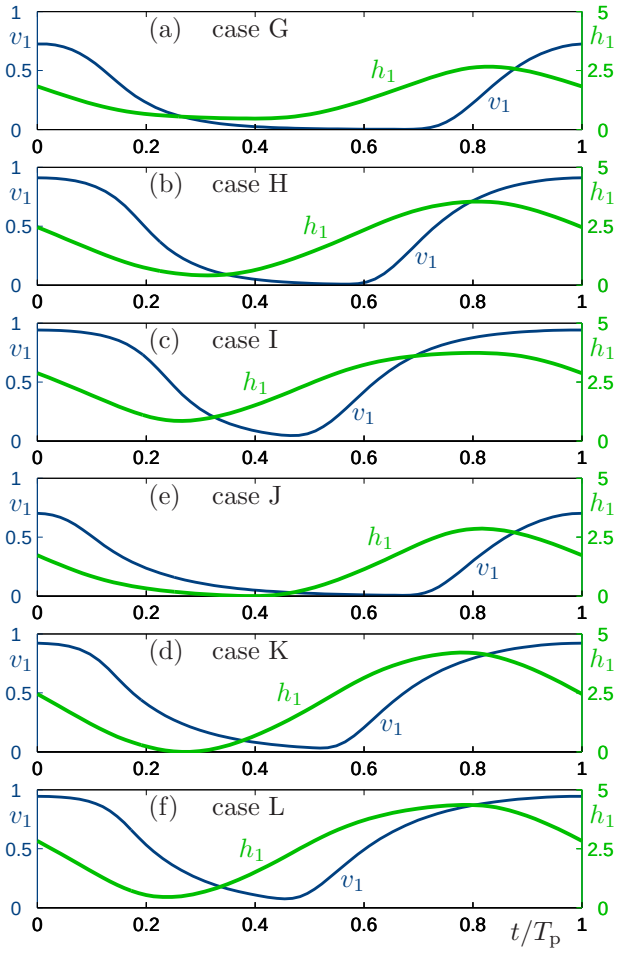

Fig. 4.7: Oscillations of the velocity v_1 of the first car over one period are shown in dark blue to the scale on the left; oscillations of the headway h_1 of the first car over one period are shown in green to the scale on the right. Cases G–L correspond to the marks in Fig. 4.3.

We marked some points A–C on the branch in Fig. 4.1(c), D–F on the branch in Fig. 4.1(d), G–I on the branch in Fig. 4.3(c), and J–L on the branch in Fig. 4.3(d), and we now display the associated time profiles in Fig. 4.6(a)–(c), in Fig. 4.6(d)–(f), in Fig. 4.7(a)–(c), and in Fig. 4.7(d)–(f), respectively. We show the velocity v_1 (dark blue curve) and the headway h_1 (green curve) of the first car over one oscillation period so that the velocity takes its maximum at $t = 0$. (The plots are the same for all cars by symmetry, except for a time shift as given by (4.3).)

First we consider the time profiles shown in Fig. 4.6(a)–(c) which correspond to the marked points A–C on the oscillation branch in Fig. 4.1(c). In case A vehicles nearly stop, and in case C the maximum speed is close to the desired speed $v^0 = 0.35$. Otherwise, there is no qualitative change between cases A–C. In addition, one can see that the oscillations of the headway are more harmonic than those of the velocity, that is, they are quite well approximated by the first term of the Fourier expansion.

An important qualitative difference for larger v^0 is that vehicles come very close to a stop ($v_i \simeq 0$) in one section of there period, see time profiles Fig. 4.7(a)–(c), corresponding to the marked points G–I on the oscillation branch in Fig. 4.3(c). In fact, model (1.23) is such that zero velocity cannot be attained in finite time (the decay of the velocity is exponential). However, loosely speaking, the 'stopping section' is the largest in case G, is smaller in case H, and disappears in case I. Furthermore, in case H the maximum speed nearly reaches the desired speed $v^0 = 1.0$. The collective motion of the system is a *stop-and-go* traffic jam: the congestion consisting of standing vehicles propagates upstream along the ring, because cars leave the jammed region at the front and enter at the back. Note that in the case of $n = 3$ cars, this jam is not pronounced, but the qualitative features of the oscillations are exactly the same as in the many-car case. As can be seen below for larger numbers of cars, this near-stopping motion is a typical system behaviour.

A noticeable phenomenon in Fig. 4.1(d) and in Fig. 4.3(d) is that the headway crosses zero during its oscillation along the dotted section of the oscillating branch, i.e., cars 'move through one another', which may be interpreted as collision. When the headway becomes negative the model is clearly unphysical. However, to investigate this unphysical behaviour, we simply extend the definition (1.24) of the OV function for negative headways by setting $\mathrm{V}(h) :\equiv 0$ for $h < 0$. As mentioned above, we marked some points D–F on the branch of oscillating solutions in Fig. 4.3(d) and we display the respective oscillations of the velocity and the headway in Fig. 4.6(d)–(f). One can see in case D that the vehicles nearly stop and in case F that they nearly reach the maximum speed $v^0 = 0.35$. Furthermore, in cases D and E cars 'touch each other', because these points are on the edge of the collision region as shown

in Fig. 4.1(d). Reducing α further, this collision section becomes larger and finally covers the entire stable part of the branch. Similar behaviour can be examined in Fig. 4.7(d)–(f) which belong to the points marked J–L on the oscillation branch in Fig. 4.3(d). In particular, in case J stopping and collision take place together.

Our main interest is now how the structure of the above oscillations changes for larger numbers of cars. In Fig. 4.8 we present the oscillation profile of the $k = 1$ periodic solution for $n = 3$, $n = 5$, $n = 9$, and $n = 17$ cars. This figure is for $h^* = 2.1$; c.f., Fig. 4.5. Plotted are the velocity v_1 and the headway h_1 of the first car, where we chose the maximum of v_1 to be at $t = 0$ again. In Fig. 4.8 all panels are drawn to the same scale so that the panel width is that of the period of the oscillation T_p for $n = 17$. The red dashed lines indicate one period for $n = 9$, $n = 5$, and $n = 3$ in panels (b), (c), and (d), respectively. The profile for $k = 1$ corresponds to a situation where the cars have (practically) zero velocity for part of the oscillation. Fig. 4.8 indicates that there is a convergence of the profiles with increasing n: the oscillation develops fronts that connect the region with (practically) zero velocity to a plateau with an (almost) constant maximal velocity. Similarly, the headway develops two regions with almost constant (small or large) headways. We distinguish between *stop-fronts* that connect a high velocity to an almost zero velocity, and *go-fronts* that connect an almost zero velocity to a high velocity. Both types of fronts appear to tend to a limit shape as n is increased; this is why we plotted all profiles in Fig. 4.8 on the same time-scale.

In Fig. 4.9 we consider how the structure of the oscillations depends on the wave number k. We now fix $n = 17$ and consider $h^* = 2.1$ again; c.f., Fig. 4.4(d). The time-scale of all plots is similar to that of Fig. 4.8, in this case all panels have a width corresponding to the period T_p of the $k = 1$ oscillation. As k decreases one notices again that the fronts between different plateaux appear to converge in profile: the main difference between the cases is the length of the plateaux. Note the contrast between Fig. 4.8 and Fig. 4.9: in Fig. 4.8 we fix $k = 1$ and increase n, whereas in Fig. 4.9 we fix a quite large value of $n = 17$ and increase k.

The period of oscillations satisfies

$$T_\mathrm{p} \simeq C\,\frac{n}{k}\,, \tag{4.4}$$

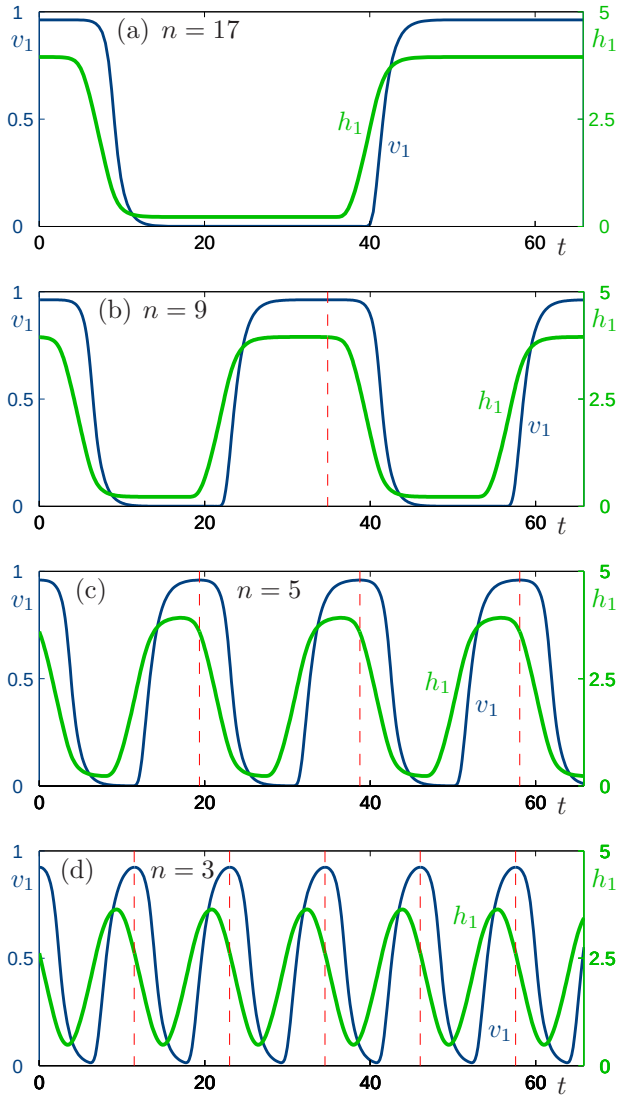

Fig. 4.8: Oscillation profiles for wave number $k = 1$ and for $n = 17$ (a), $n = 9$ (b), $n = 5$ (c), and $n = 3$ cars (d); the desired speed is $v^0 = 1.0$, the sensitivity is $\alpha = 1.0$, and the average headway is $h^* = 2.1$. The velocity v_1 of the first car is shown in dark blue to the scale on the left; the headway h_1 of the first car is shown in green to the scale on the right. All panels are shown on the scale of one period of $T_\mathrm{p} \simeq 65.8171$ for $n = 17$; the other periods of $T_\mathrm{p} \simeq 34.8447$ for $n = 9$, $T_\mathrm{p} \simeq 19.3540$ for $n = 5$, and $T_\mathrm{p} \simeq 11.5445$ for $n = 3$ are indicated by red dashed vertical lines. Notice the convergence of the stop-fronts and go-fronts, that is, the sections of the orbits that connect the plateaux approach a fixed profile as n is increased.

for a constant C that depends on the parameters h^*, α, and v^0; and which is represented in Fig. 4.8 and in Fig. 4.9 with the help of the red vertical dashed lines. This means that the

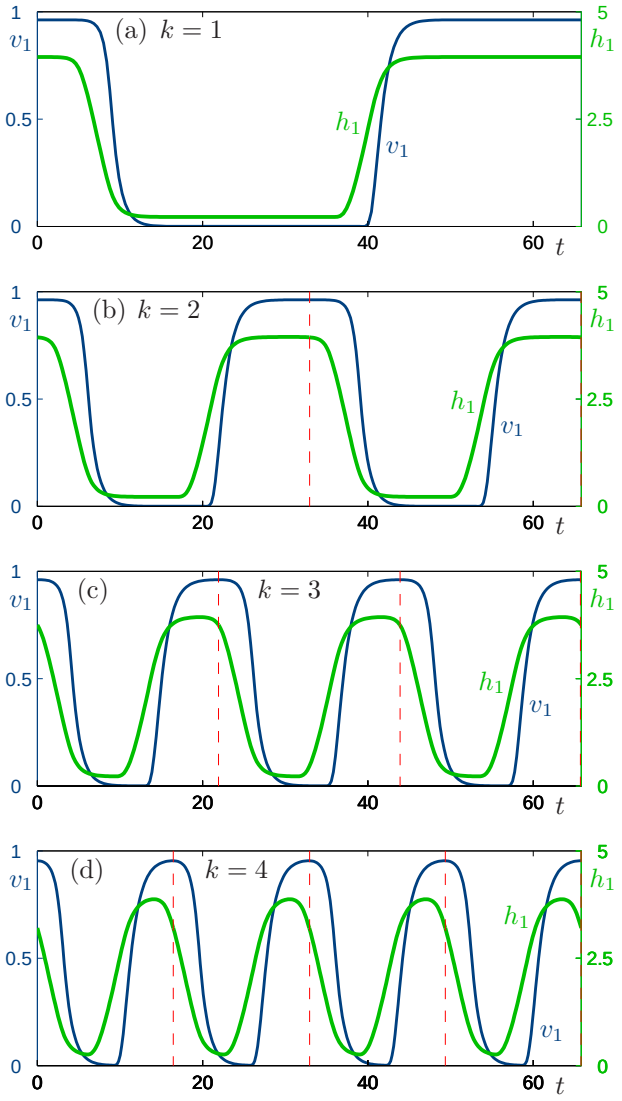

Fig. 4.9: Oscillation profiles for $n = 17$ and for wave numbers $k = 1$ (a), $k = 2$ (b), $k = 3$ (c), and $k = 4$ (d); the desired speed is $v^0 = 1.0$, the sensitivity is $\alpha = 1.0$, and the average headway is $h^* = 2.1$. The velocity v_1 of the first car is shown in dark blue to the scale on the left; the headway h_1 of the first car is shown in green to the scale on the right. All panels are shown on the scale of one period of $T_\mathrm{p} \simeq 65.8171$ for $k = 1$; the other periods of $T_\mathrm{p} \simeq 32.908$ for $k = 2$, $T_\mathrm{p} \simeq 21.9379$ for $k = 3$, and $T_\mathrm{p} \simeq 16.4403$ for $k = 4$ are indicated by red dashed vertical lines. Notice the convergence of the stop-fronts and go-fronts, that is, the sections of the orbits that connect the plateaux have approximately the same structure for small k.

strongly nonlinear oscillations preserve the spatial wave motion described by (3.161). It can also be checked that the period of oscillation does not change significantly along the oscillation

branches, so the wave speed (3.18) computed at the linear level is a good approximation even at the nonlinear level.

For large n/k, we have shown that the stop-fronts and go-fronts have a limiting structure. This result indicates that we have recovered fronts that are close to travelling wave solutions in the case of open boundaries, and that only feel each other weakly since the number of vehicles ($\sim n/k$) between structures is large. The dynamics of these fronts are investigated in detail in Chapter 5.

4.3 Two-dimensional bifurcation diagrams

In this section we use two-dimensional bifurcation diagrams to summarise how the qualitative behaviour depends on the problem parameters, namely the average headway h^*, the sensitivity α, the desired speed v^0, and the number of cars n. In Section 3.1.2 we presented similar diagrams (Figs. 3.1 and 3.2) which were concerned only about the linear dynamics of the system around equilibrium (1.16),(1.18). The information concerning the global dynamics was presented in Section 4.1 by plotting the amplitude of the oscillations as a function of the control parameter h^* for different fixed values of α, v^0, and n; and in Section 4.2 by showing the the structure of oscillations at different points along these branches.

We now present the global dynamics in a more concise way as two-dimensional bifurcation diagrams in the (h^*, α) plane for fixed v^0 and n. Specifically, we show solid curves of Hopf bifurcations, red dashed curves of fold bifurcations of oscillating solutions, gray curves of first collision, and dotted curves of first stopping. These curves divide the (h^*, α) plane into regions of qualitatively different behaviour. In this representation, the diagrams we showed earlier in Section 4.1 correspond to horizontal cross sections with fixed values of α.

The Hopf bifurcation curves are the only curves that can be computed directly with DDE-BIFTOOL, but in our case these are given analytically by (3.10). Fold bifurcations can only be detected by this software, and the fold curves found here were found by a script

that detects a suitable number of individual fold points for (about 50) different values of the parameter α. In a similar approach, the collision curve was found by detecting points where the headway h_1 of the oscillating solution first crosses zero. Similarly, the stopping curve was found by detecting when the velocity v_1 first becomes (approximately) zero; in practice we used the criterion that $v_1 < 0.01$ because the velocity never actually attains zero (it decays exponentially). As before, we first concentrate on the proof-of-concept case of $n = 3$ cars where by investigating the dynamics in the (h^*, α) plane for different values of v^0 allows us to describe the dynamics of the system in the complete parameter space. Then we fix the desired speed as $v^0 = 1.0$ and investigate the changes in the (h^*, α) plane by increasing the numbers of cars n.

In Fig. 4.10 the (h^*, α) bifurcation diagram is shown for $n = 3$ cars for three representative values of v^0, namely for 0.35, 0.65, and 1.0. We now discuss the results of this figure in some detail. For $v^0 = 0.35$, shown in Fig. 4.10(a), the Hopf bifurcation curve is one single curve as in Fig. 3.1(b) (the top of the curve is not visible in the chosen window of α). The outer blue shaded area corresponds to the stable uniform flow solution as before. The fold bifurcation curves of the periodic solution are situated on the right-hand side of the right Hopf curve and on both sides of the left Hopf curve. The fold curve on the right starts at a degenerate Hopf point DH_r and approaches the h^* axis as shown. Above DH_r the Hopf bifurcation is supercritical and below DH_r it is subcritical. The region between the Hopf and the fold curve is thus identified as a region of bistability, where the equilibrium and a stable periodic solution co-exist. On the left-hand side, the Hopf bifurcation is always supercritical and the bistability appears via a cusp bifurcation where two fold curves are born; see the inset of Fig. 4.10(a). The two fold curves end approximately at the points $(0, 0.0167)$ and $(1, 0)$. The region between the two fold curves is a region of bistability. The Hopf curve divides this region into two subregions, in which the one on the left corresponds to the co-existence of an equilibrium and a stable oscillating solution, while the very small region on the right corresponds to the co-existence of two stable oscillating solutions; c.f. Fig. 4.1(d). For $v^0 = 0.35$ there is no stopping motion, but we find the gray curve of the first collision cutting across the bifurcation diagram. In the gray shaded domain below this curve collisions

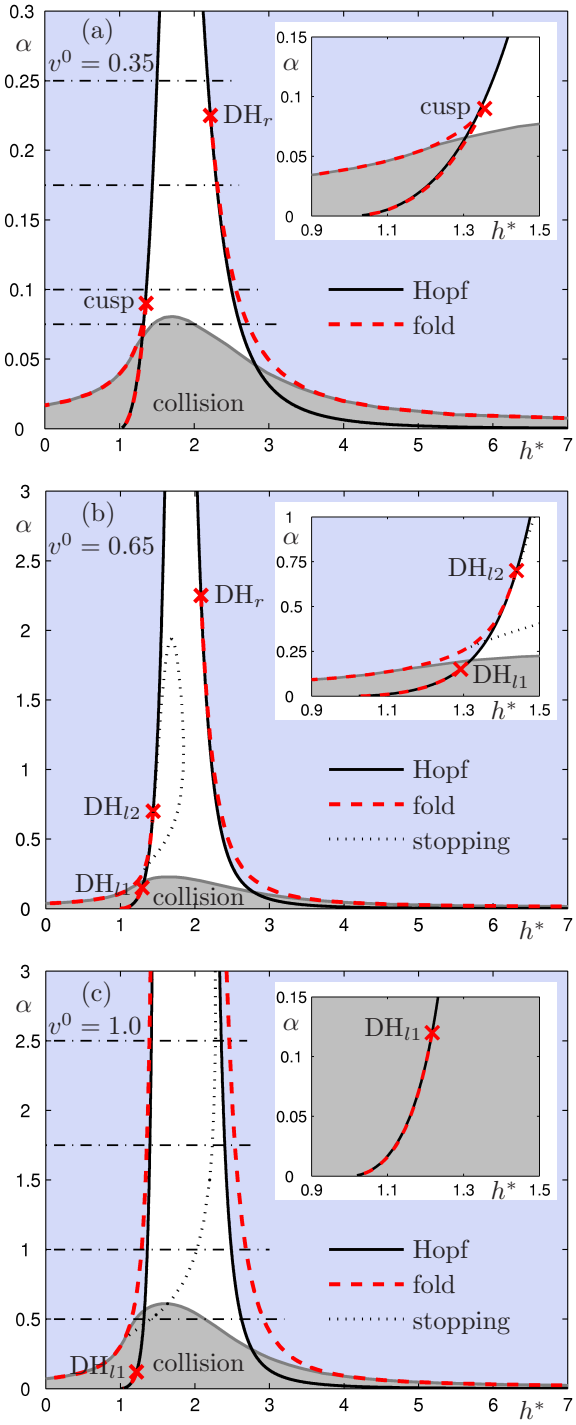

Fig. 4.10: Two-dimensional bifurcation diagrams in the (h^*, α) plane for $n = 3$ cars for different values of v^0 as indicated. At points denoted by red crosses (x) the Hopf bifurcation is degenerate. The horizontal dashed-dotted lines in panels (a) and (c) correspond to the values of α used in Figs. 4.1 and 4.3, respectively.

occur, which means that there are no collisions for $\alpha \gtrsim 0.0805$. The individual panels of Fig. 4.1 correspond to horizontal cross sections through Fig. 4.10(a) at the indicated values of α. In particular, Fig. 4.1(d) features collisions for values of h^* from the section between the two intersection points with the collision curve. This section becomes larger as α is decreased further. Where the collision manifold reaches the fold curve, collisions occur over the entire branch of stable oscillating solutions.

For $v^0 = 0.65$, shown in Fig. 4.10(b), the bifurcation diagram is qualitatively the same as for $v^0 = 0.35$ except for two differences. Firstly, the cusp point is gone and two degenerate Hopf points DH_{l1} and DH_{l2} are now the end points of the two fold curves on the left. (This change happens for a specific value of v^0 when the cusp point reaches the Hopf curve at $\alpha \simeq 0.4$.) The Hopf bifurcation is subcritical between these two degenerate Hopf points and supercritical otherwise. Co-existing stable oscillating solutions exist only in the tiny region between the Hopf curve and the fold curve below DH_{l1} (on the right side of the Hopf curve). In the much larger region between the other fold curve and the Hopf curve below DH_{l2} (on the left side of the Hopf curve), there is co-existence between the stable equilibrium and stable oscillations. The collision domain is qualitatively the same but it is now a bit larger; its top is at $\alpha \simeq 0.227$. The other new feature is the existence of near-stopping motion on the domain bounded by the left fold curve and the dotted stopping curve. The curve of near-stopping, defined as $v_1 = 0.01$, appears to start at the point DH_{l2} and connect to a point on the left-most fold curve.

For $v^0 = 1.0$, shown in Fig. 4.10(c), there are now two vertical asymptotes for the two Hopf curves, as in Fig. 3.1(c), meaning that the unstable area is now unbounded in α. Compared with the situation for $v^0 = 0.65$, the points DH_{l2} and DH_r move up in α and out of our window, 'dragging' the associated curves with them. In fact, these points have disappeared so that the fold curves and the stopping curve also now have vertical asymptotes. (We found that all vertical asymptotes develop for $v^0 \simeq 0.7198$.) In other words, Fig. 4.10(c) is qualitatively the same as Fig. 4.10(b) for, say, $\alpha \lesssim 0.7$. Notice how the stopping region is now much larger. Furthermore, the collision domain is also much larger; its top is at $\alpha \simeq 0.61$.

The indicated horizontal cross sections correspond to the panels of Fig. 4.3.

When considering different values of the scaling parameter s, the only qualitative change is that the cusp point may be below the collision curve. For the OV functions $V_{B4}(h)$ (1.25) or $V_S(h)$ (1.26), one can obtain similar branches of oscillating solutions as above, although the dynamics may be non-smooth and thus DDE-BIFTOOL may run into difficulties.

Our aim is now to show the general trends in the qualitative dynamics in the (h^*, α) plane as n is increased towards numbers that are more representative of real traffic situations. To simplify matters, we fix $v^0 = 1.0$. Note that choosing larger values of v^0 does not change the linear stability diagram qualitatively; see Section 3.1.2. In particular, we find regions of parameter space where a stable periodic solution with $k = 1$ traffic jam co-exists with unstable periodic solutions corresponding to $k > 1$ evenly spaced traffic jams.

Since continuation studies with DDE-BIFTOOL are quite intensive in terms of CPU time and memory, the bifurcation analysis for very large numbers of cars is unfeasible. We found that the case of $n = 9$ cars is a good compromise: it is sufficiently general to showcase all phenomena in the bifurcation diagram while still being small enough to allow for a full bifurcation analysis.

In Fig. 4.11 we present three bifurcation diagrams in the (h^*, α) plane for $n = 3$, $n = 5$, and $n = 9$ cars. We now describe the common qualitative features of these two-parameter bifurcation diagrams and then give particular details for each of the cases.

Firstly, the linear theory of Section 3.1 gives explicit curves in the (h^*, α) plane where the uniform flow equilibrium loses stability via a Hopf bifurcation that gives rise to oscillations with wave number $k = 1$. These Hopf bifurcation curves are shown in Fig. 4.11 as bold solid curves and the blue shaded areas indicate where the uniform flow equilibrium is stable. For $n > 3$ cars there is a further set of admissible wave numbers $k = 2, \ldots, (n-1)/2$. (To reduce the number of special cases, we consider only the n odd case.) The linear theory gives explicit curves on which further Hopf bifurcations of the (already unstable) uniform flow equilibrium occur (i.e., other complex conjugate pairs of characteristic exponents, corresponding to a

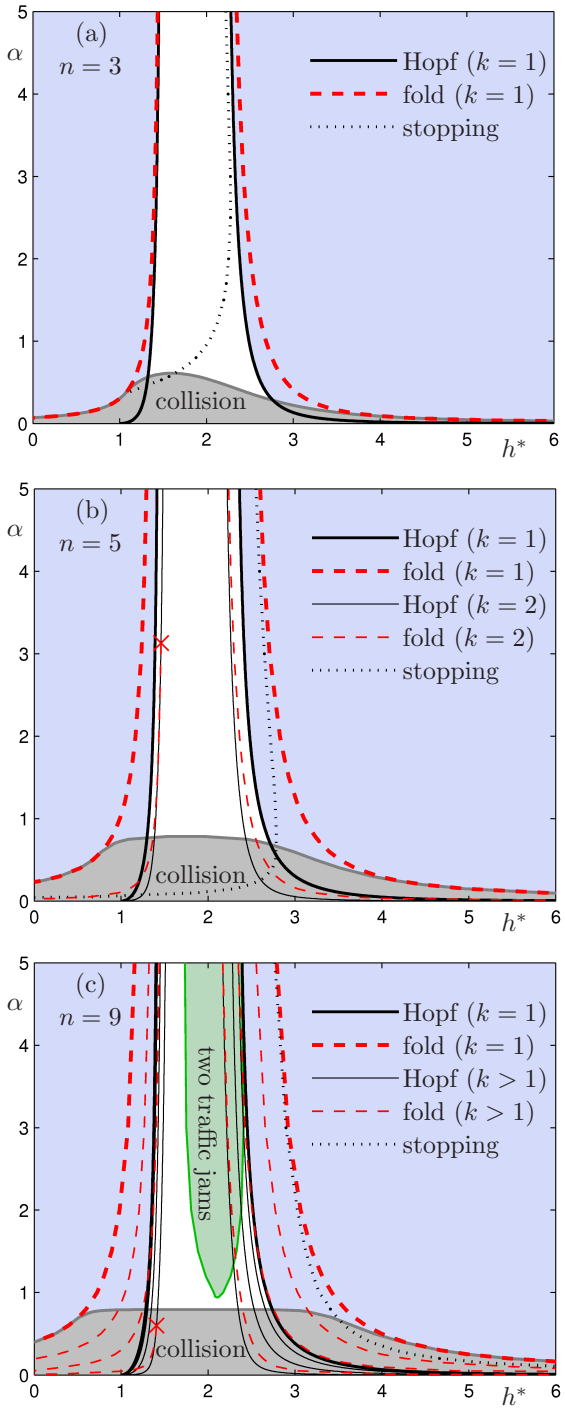

Fig. 4.11: Two-dimensional bifurcation diagrams in the (h^*, α) plane for $n = 3$ (a), $n = 5$ (b), and $n = 9$ cars (c) for desired speed $v^0 = 1.0$. At points denoted by red crosses (x) the Hopf bifurcation is degenerate. In panel (c) the region of two traffic jams is defined by the condition $\max|\mu| \leq 1.01$ for the largest Floquet multiplier of periodic solutions for $k = 2$.

mode with wave number k, cross into the right-half complex plane). These curves are shown in Fig. 4.11(b) and (c) as thin solid curves.

The Hopf curves are nested in strict order so that the $k = 1$ curves are the outermost and the $k = (n-1)/2$ curves are the innermost. Further, for the chosen value $v^0 = 1.0$, the Hopf bifurcation curves all possess vertical asymptotes in the (h^*, α) plane as in Fig. 3.2(f), that is, the unstable domains are unbounded in α.

If one examines the Floquet multipliers of the unstable bifurcating branches in the vicinity of the Hopf bifurcation point, one finds $2k-1$ multipliers outside the unit circle (one real multiplier and $k-1$ complex conjugate pairs); see Section 5.2. Furthermore, each branch of unstable periodic solutions usually undergoes a fold bifurcation as shown in Fig. 4.4, where the real unstable Floquet multiplier crosses the unit circle inwards at 1. Consequently the $k = 1$ branch becomes stable at this bifurcation, but the $k > 1$ branches remain unstable as they still have $2(k-1)$ Floquet multipliers outside the unit circle.

The fold bifurcation curves are shown in Fig. 4.11 as red dashed curves and the curves for $k = 1$ are emphasized in bold. The Hopf curve for a particular k is nested inside the fold curve for the same k, and the fold curves themselves are nested in strict order so that the outermost curves belong to $k = 1$ while the innermost curves belong to $k = (n-1)/2$. Further, most of the fold curves have vertical asymptotes meaning that the Hopf bifurcation remains subcritical even as $\alpha \to \infty$. However, in some cases the fold curve ends at a degenerate Hopf point, i.e., at a point where the Hopf bifurcation changes from subcritical to supercritical as α is increased: these points are marked by red crosses (×) in Fig. 4.11(b) and (c). For any given n, degenerate Hopf points have only been observed to occur for the largest possible wave number, which corresponds to the analytical results obtained in Section 3.3.3. Note that in the vicinity of the point $(1, 0)$ one might examine similar bistability as presented in Fig. 4.10(c) even for $n > 3$. Nevertheless, the corresponding domains of parameter space are so tiny that it seems sensible to neglect this effect. That is why these domains are not depicted in Fig. 4.11.

Inside the fold curve for $k = 1$, there exists a stable periodic solution, as detailed for $n = 3$. Therefore, in the parameter domain sandwiched between the fold and Hopf curves for $k = 1$, the stable periodic solution co-exists with the stable uniform flow equilibrium and an unstable periodic solution. In other words, there is bistability in this region. When one carries out an initial value simulation, the precise choice of initial data will select which of the two stable solutions is observed as $t \to \infty$.

If we enter the parameter domain sandwiched between the fold and Hopf curves for $k > 1$, then the only change is in the number of co-existing unstable solutions, and it is not yet clear what this implies for the dynamics. For $k_1 < k_2$, there is no general principle as to whether the Hopf curve for k_1 is inside/outside the fold curve for k_2, so there is a wide range of possibilities for the combinations of co-existing unstable solutions.

We now describe tendencies of the three extra features that we have added in the two-parameter diagrams of Fig. 4.11. We illustrated the stopping behaviour by adding a dotted curve which, when crossed from right to left results in the minimum velocity of the stable $k = 1$ branch falling below 0.01. When n increases, the dotted curve appears to converge to the right-hand $k = 1$ fold curve. Thus it seems that cars always come close to stopping if n is chosen sufficiently large.

The gray curve in Fig. 4.11 indicates where the the headway first becomes zero on the $k = 1$ stable solution branch. Consequently, we can say that the model is definitely unphysical in the gray shaded domain below this curve. The section of the gray curve, which connects the $k = 1$ fold curves, appears to converge to a horizontal line as n increases. Consequently, it appears that, in the large n limit, there is a critical α below which the model is unphysical. However, this conclusion is only partial: above the gray curve there are most likely solutions with plausible initial data which involve collisions as part of their transient behaviour, even though their long-term dynamics is well behaved.

The most important extra feature, which is discussed in detail in Section 5.2, is the green shaded domain in the middle of Fig. 4.11(c). This shading indicates that the largest Floquet

multiplier of the (unstable) $k = 2$ branch has modulus less than 1.01. Consequently, in this region, solutions with initial data chosen sufficiently close to the $k = 2$ unstable periodic solution remain close to that solution for a long time. Therefore, although simulations indicate that the generic $t \to \infty$ behaviour is convergent either to the uniform flow equilibrium or to the stable $k = 1$ branch, richer possibilities may be observed over intermediately long time scales.

While the continuation approach taken here limits n to relatively small values, Figs. 4.8 and 4.9 still clearly suggest a convergence of the $k = 1$ solution to some limiting shape as $n \to \infty$, as well as a convergence of the oscillations for other wave numbers to that for $k = 1$ as $n/k \to \infty$. As we will see in the next section, this has important consequences in terms of the structure of transient traffic jams. Note that identifying the mathematical limit and, in particular, the exact scaling of the fronts, remains an interesting challenge beyond the bifurcation study presented here.

Chapter 5

Transient behavior of traffic waves

In Chapter 4 the periodic solutions of system (1.6),(1.23) were investigated and it was shown that for large numbers of cars, there are stop-fronts and go-fronts that connect plateaux of high and low velocities. These fronts correspond to the entry and exit points of traffic jams. However, the periodic solutions that we found are unstable for wave numbers $k > 1$. Nevertheless, these unstable solutions influence the long time dynamics of the system and this chapter is concerned with an analysis of the consequent transient effects.

Firstly, in Section 5.1 we give an overview of the long-time macroscopic dynamics of stop-and-go waves under ring-road boundary conditions. Then in Section 5.2 the Floquet multipliers of periodic orbits are investigated in order to determine the 'degree' of stability of these orbits and to suggest time scales over which motions are repelled from them. This analysis is used to give a linearized explanation of the relative motion of traffic jams, and these motions are investigated further by numerical simulation in Section 5.3. The material presented in this chapter was published in [85].

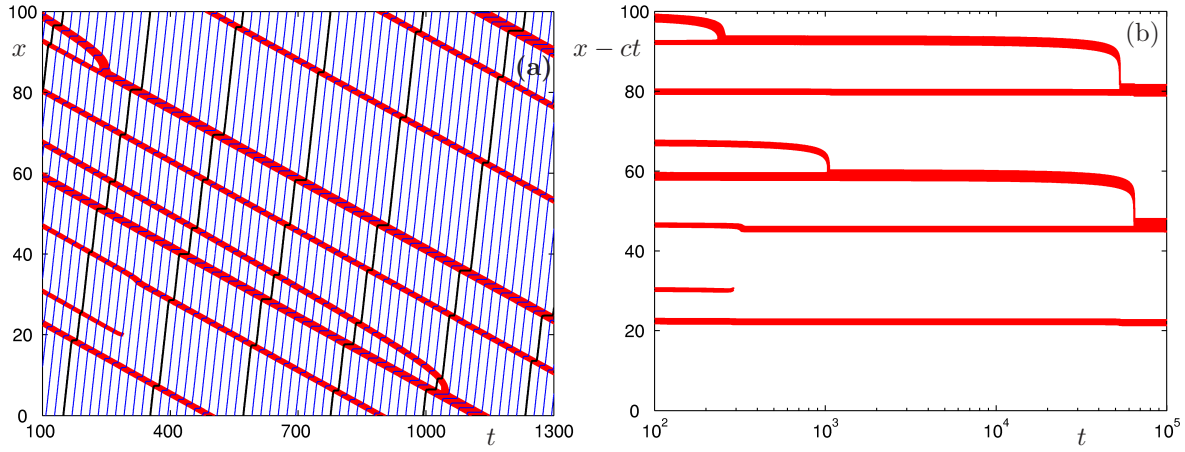

Fig. 5.1: Long time evolution of stop-and-go waves detected when vehicles' velocities are less than $v^0/3$. Panel (a) shows a spatio-temporal plot of the ring-road, where, due to the periodic boundary conditions, the boundaries $x \equiv 0$ and $x \equiv L = 100$ are equivalent. Red curves show backward travelling waves. The trajectories of every fifth forward travelling vehicle are shown by blue curves (the trajectory of the first vehicle is emphasized in black). In the spatio-temporal plot of panel (b), the relative positions of waves are shown for long time scales, so that the constant speed motion ct is eliminated. The corresponding parameters are $n = 50$, $v^0 = 1.0$, $\alpha = 1.0$, $h^* = 2.0$, and $c = -0.0579$.

5.1 Overview of traffic dynamics over long time scales

Traffic jams correspond to regions in space in which vehicles' velocities (i.e., the gradient of their space-time trajectories) is small; see Fig. 5.1(a). As observed by many other authors (see, e.g., [53]), for appropriate parameters and initial data, traffic organizes into regions of free flowing traffic divided by traffic jams which propagate at about the same speed to each other in the opposite direction to the traffic flow. The question is how such traffic patterns evolve.

For large numbers of cars, of particular interest is the interplay between propagating traffic jams (Fig. 5.1(a)) and perfectly periodic solutions (Fig. 4.9). To understand these traffic patterns one needs to consider the dynamics of a single vehicle as it drives repeatedly around the circuit; see, e.g., the black trajectories in Fig. 5.1(a). The velocity plateaus at a high value, meets a stop-front in which the vehicle decelerates into a traffic jam, plateaus at a low value, and then passes through a go-front as it returns to free flow conditions. Since

the stop-fronts and go-fronts propagate at about the same speed upstream, the motion of the vehicle is approximately periodic in time because it encounters the same traffic pattern for each circuit, albeit shifted according to the wave speed. The solutions shown in Fig. 4.9 are perfectly periodic and also possess stop-fronts and go-fronts that connect the high and low velocity plateaux. Our belief is that the approximately periodic solutions lie on slow manifolds that connect the various periodic solutions. Although, these manifolds are fully nonlinear objects, a first step is to understand their structure at the linear level, in the neighbourhood of perfectly periodic solutions.

The traffic jams in Fig. 5.1(a) are called stop-and-go waves, although we should emphasize that each traffic jam is strictly speaking a pair of fronts with similar speeds, separated by a low-velocity plateau. By eliminating the approximately constant speed of propagation ct of the fronts, their relative dynamics can be explored as shown in Fig. 5.1(b). To bring out the relevant features, a logarithmic scale is used along the horizontal axis. For intermediately long time scales the relative motion of traffic jams is slow, however rapid merges and dispersions can be observed from time to time. The key point to note is that different traffic jams have similar speeds (that is, their relative speed is close to zero) and therefore they may co-exist over intermediately long time scales. However, as $t \to \infty$ traffic jams have a tendency to merge or to disperse. For generic choices of initial data, numerical simulation indicates that only a single traffic jam persists as $t \to \infty$.

5.2 Floquet multipliers and eigendirections

In this section we investigate the periodic solutions of Chapter 4 in further detail. Firstly, Floquet multipliers are computed to investigate stability. Then with the help of the corresponding eigenvectors, possible front motions are revealed. As explained in Section 2.2, the periodic solutions are unstable when there exists a Floquet multiplier outside the unit circle. However, when the largest 'unstable' Floquet multiplier is close to the unit circle, the system is only weakly unstable in that it can stay in the vicinity of the periodic solution for a long

time. More precisely, using the Floquet multiplier μ one can define the Floquet exponent ν by

$$\mu = \mathrm{e}^{\nu T_\mathrm{p}}\,, \tag{5.1}$$

the real part of which given by

$$\mathrm{Re}\nu = \frac{\ln|\mu|}{T_\mathrm{p}}\,. \tag{5.2}$$

Indeed,

$$\mathrm{Re}\nu \simeq \frac{|\mu|-1}{T_\mathrm{p}}\,, \quad \text{for} \quad |\mu| \simeq 1\,. \tag{5.3}$$

Assuming that there is a Floquet multiplier $|\mu| >\simeq 1$, the 'distance' from the periodic orbit grows like $\mathrm{e}^{\mathrm{Re}\nu\, t}$, and thus, the time spent in the vicinity of the weakly unstable periodic solution scales like $1/\mathrm{Re}\nu \simeq T_\mathrm{p}/(|\mu|-1)$.

By computing Floquet multipliers of periodic orbits we thus show that the periodic solutions with wave numbers $k > 1$ are only weakly unstable. Furthermore, the corresponding unstable eigendirections show that the mechanism of destabilization is via front dynamics. Both the Floquet multiplier and mode shape calculations that we perform are achieved with the numerical continuation software DDE-BIFTOOL [36, 44]. We find that the largest Floquet multiplier μ has a scaling of $|\mu| - 1 \sim \exp(-q\, n/k)$, $q > 0$. This analysis indicates that our periodic solutions' fronts correspond to travelling wave solutions when the boundaries are open, but on the loop interact weakly via their exponential decaying tails (in a similar manner to meta-stable front dynamics for the Allen-Cahn equation; see [23, 24]). We show that the eigendirections correspond to relative front motion: either one stop-and-go pair catching up another stop-and-go pair (merging of traffic jams), or the stop-and-go fronts of a single jam colliding so as to disperse it.

We now look more closely at the stability properties of the different periodic solutions. In Fig. 5.2 the modulus $|\mu|$ of the corresponding leading Floquet multipliers are depicted as a function of the headway h^* in the representative case of $n = 9$ cars for the wave numbers $k = 1, 2, 3, 4$. Recall from Section 2.2 that for periodic solutions of DDEs the infinitely many Floquet multipliers have the origin in the complex plane as their only accumulation point; all Floquet multipliers that are not shown in Fig. 5.2 have modulus less than one for all

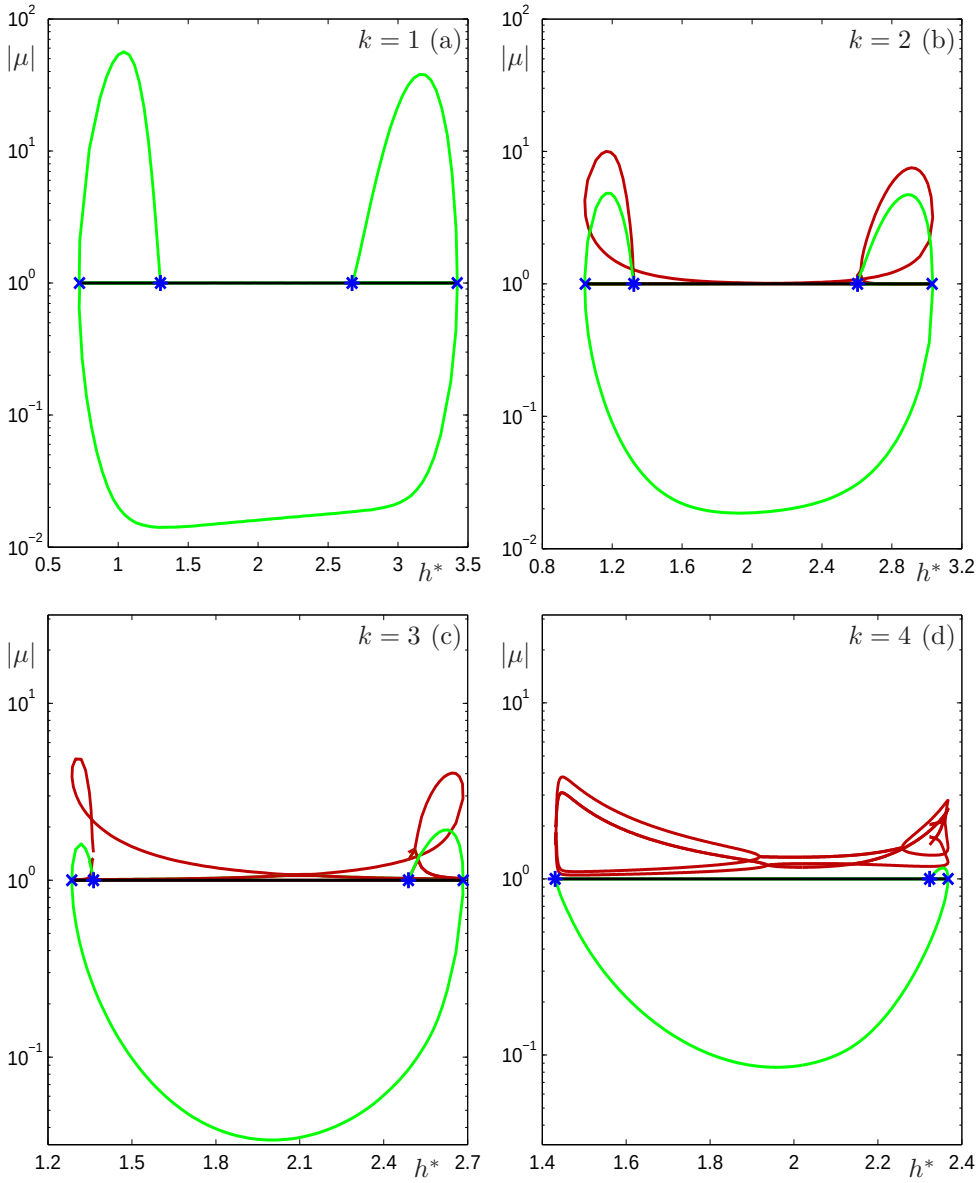

Fig. 5.2: Modulus $|\mu|$ of the leading Floquet multipliers as a function of the average headway h^* in the case of $n = 9$ cars for wave numbers $k = 1$ (a), $k = 2$ (b), $k = 3$ (c), and $k = 4$ (d). This figure corresponds to the branches of periodic solutions shown in Fig. 4.4(c); we have $v^0 = 1.0$ and $\alpha = 1.0$. Hopf and fold bifurcation points are denoted by blue stars ($*$) and blue crosses ($\times$), respectively.

values of h^*. The leading Floquet multipliers were computed with DDE-BIFTOOL as part of the stability analysis along the branches shown in Fig. 4.4(c). To bring out the features, we use a logarithmic scale along the vertical axis. For any k, at the Hopf bifurcation points

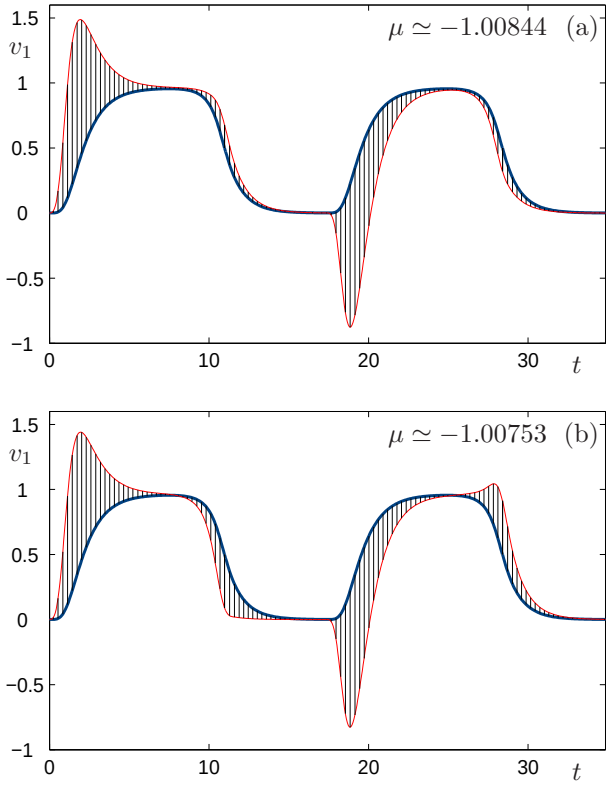

Fig. 5.3: Eigendirections in the form of a direction fields plotted over twice the period of the periodic solution as projections onto the velocity v_1 of the first car. The red curves show the corresponding modulated solutions. Panel (a) for $\mu \simeq -1.00844$ corresponds to merging of traffic jams as shown in Fig. 5.5, while panel (b) for $\mu \simeq -1.00753$ corresponds to dispersion of one of the traffic jams as depicted in Fig. 5.6. The parameters are $n = 9$, $k = 2$, $v^0 = 1.0$, $\alpha = 1.0$, and $h^* = 2.1$.

there are two Floquet multipliers at 1 and another $(k-1)$ complex conjugate pairs of Floquet multipliers outside the unit circle. One multiplier (green curve) moves outside the unit circle at the subcritical Hopf bifurcations (blue stars (∗)) and then crosses into the unit circle at the fold bifurcations (blue crosses (×)). Similarly, the other leading multipliers for $k > 1$ appear outside the unit circle at their subcritical Hopf bifurcations, but then stay outside the unit circle over the entire range of h^*. Thus in particular, Fig. 5.2 shows that all periodic orbits are unstable for $k > 1$. For even k we observe that one of the complex conjugate pairs of Floquet multipliers may come together and produce two real Floquet multipliers. For n/k large enough this happens close to the Hopf bifurcation point.

However, Fig. 5.2(b) also shows that the oscillation for $k = 2$ is almost stable around the point $h^* = 2.1$; at this point the two unstable eigenvalues are real and negative, namely $\mu \simeq -1.00844$ and $\mu \simeq -1.00753$. By setting a threshold for $\max|\mu|$ one can quantify the 'almost-stability' of the periodic orbit for $k = 2$: inside the green shaded region in Fig. 4.11(c) we have that $\max|\mu| \leq 1.01$. While this bound is somewhat arbitrary, we found by numerical simulation that traffic jams corresponding to $k = 2$ periodic orbits exist in this parameter region for long periods of time; see Section 5.3 for more details on the connection between periodic solutions and traffic jams. More generally, there is a region around $h^* = 2.1$ where the unstable waves for any k are in the same sense 'least unstable'. Our numerical results indicate that this effect is more pronounced the larger the number of cars n.

The instability of a weakly periodic orbit is very small, but it is not 'spread evenly' around the periodic orbit. To show this we present in Fig. 5.3 the eigendirection associated with the two unstable Floquet multipliers $\mu \simeq -1.00844$ and $\mu \simeq -1.00753$ of the weakly unstable periodic orbit for $n = 9$ and $k = 2$. It is computed and represented by DDE-BIFTOOL in the form of a direction field that shows how a vector changes along the periodic orbit under the action of the variational equation [44]. We show the unstable direction with respect to the velocity profile of the first car. The Floquet multiplier measures the expansion (which is practically nonexistent in our case of Floquet multipliers that are almost 1 in magnitude) of a vector as the flow is followed along the periodic orbit. The data in Fig. 5.3 is plotted over two periods, because the most unstable Floquet multipliers are negative: thus the vectors forming the eigendirections only close up after two periods. In Fig. 5.3 only the vectors at the mesh points are shown and the red curve is the envelope of all vectors.

For both unstable Floquet multipliers the periodic orbit is most unstable near the fronts between the plateaux. This indicates that any eventual instability is due to the motion of the fronts. Notice the difference between the two cases in Fig. 5.3(a) and (b) in terms of the direction of motion of the stop-fronts. As we will see in the next section, front dynamics is responsible for merging or dispersing traffic jams.

We now show that we can extract from the bifurcation analysis the asymptotics of the

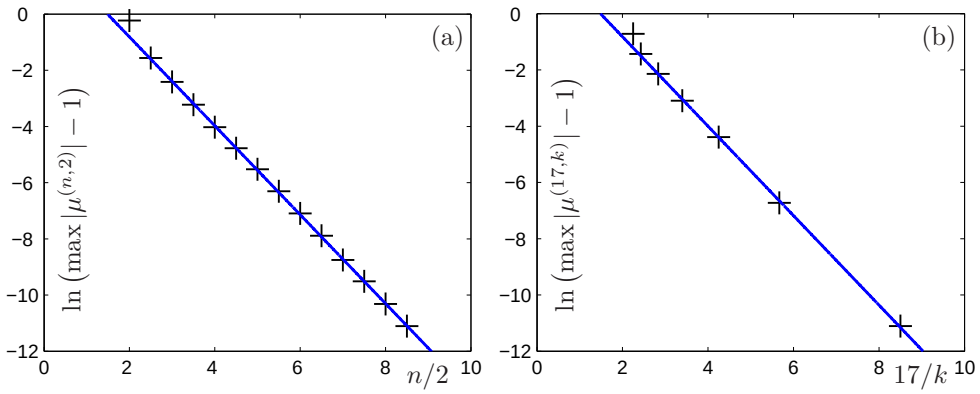

Fig. 5.4: The logarithm of the difference of the modulus of the largest Floquet multiplier from 1 as a function of n/k for the periodic solutions for $v^0 = 1.0$, $\alpha = 1.0$, and $h^* = 2.1$. Panel (a) shows a plot for fixed $k = 2$ and varying n, and panel (b) for fixed $n = 17$ and varying k. The blue curve is a least square fit (omitting the first data point); see also Table 5.1.

modulus $|\mu^{(n,k)}|$ of the largest Floquet multiplier, as a function of n and k. Different fronts interact via an overlap of their exponentially decaying tails. Consequently, we make the ansatz that there is an exponential relationship of the form

$$\max|\mu^{(n,k)}| - 1 = R\, e^{-q\frac{n}{k}}\,, \tag{5.4}$$

when n is large and k is small enough; c.f. [23, 24]. Clearly, in general the constants $q, R > 0$ depend on the parameters h^*, α, and v^0.

We test this ansatz in Fig. 5.4 where we plot $\max|\mu^{(n,k)}| - 1$ on a logarithmic scale as a function of n/k, where n varies for $k = 2$ in panel (a) and k varies for $n = 17$ in panel (b). In each panel the blue line is the least-square fit through all but the first data point, which we disregarded as exceptional in terms of the convergence effect for $n/k \to \infty$ that

Table 5.1: Least-square fitted constants appearing in (5.4) for the periodic solutions for $v^0 = 1.0$, $\alpha = 1.0$, and $h^* = 2.1$.

	$k = 2 \quad (n = 5, \ldots, 17)$	$n = 17 \quad (k = 2, \ldots, 7)$
q	1.5816 ± 0.0053	1.5901 ± 0.0121
$\ln R$	2.3522 ± 0.0308	2.3616 ± 0.0601

we are interested in. The resulting values of q and $\ln R$ for both cases are shown in Table 5.1. Together with the good fit of the blue lines in Fig. 5.4, this is numerical evidence that the largest Floquet multiplier scales (for fixed parameters) as given by (5.4). Note that the data presented in Fig. 5.4 constitutes the state of the art of what can be achieved with the standard DDE-BIFTOOL implementation on a single workstation.

5.3 Traffic jams as long transients

In this section we use numerical simulation to investigate the far from equilibrium front motions suggested by the analysis that linearizes about periodic orbits. The trajectory of each individual vehicle and the low-dimensional long-time dynamics of fronts (formed by the collective motions of vehicles) can be visualised in Fig. 5.5(a) and Fig. 5.6(a).

In our model, traffic jams are regions of the ring where cars travel with low velocity (e.g., regions for less than $v^0/3$ are shown in red in Fig. 5.5(a) and Fig. 5.6(a)). A traffic pattern consists of a finite number of traffic jams that all move with their own different (but typically similar) speeds upstream. Over long time scales, a traffic jam can disperse, or merge with another traffic jam. Hence, there is an evolution of the traffic pattern until a stable pattern has been reached.

Of importance is the relationship between a traffic pattern and the trajectory of an individual car. A stable traffic pattern corresponds to a stable periodic orbit for the motion of the cars. Hence, the only stable traffic pattern in our model is that corresponding to the stable oscillations for $k = 1$ when one traffic jam travels along the circular road. Similarly, if the pattern is nearly stable, a car almost has the same velocity and headway profile from round to round. In particular, unstable periodic orbits are related to unstable traffic patterns. As we will see now, weakly unstable periodic orbits give rise to traffic jams that can persist as long transients. The motion of the traffic jams is closely related to the motion of the fronts of the almost periodic dynamics of the cars.

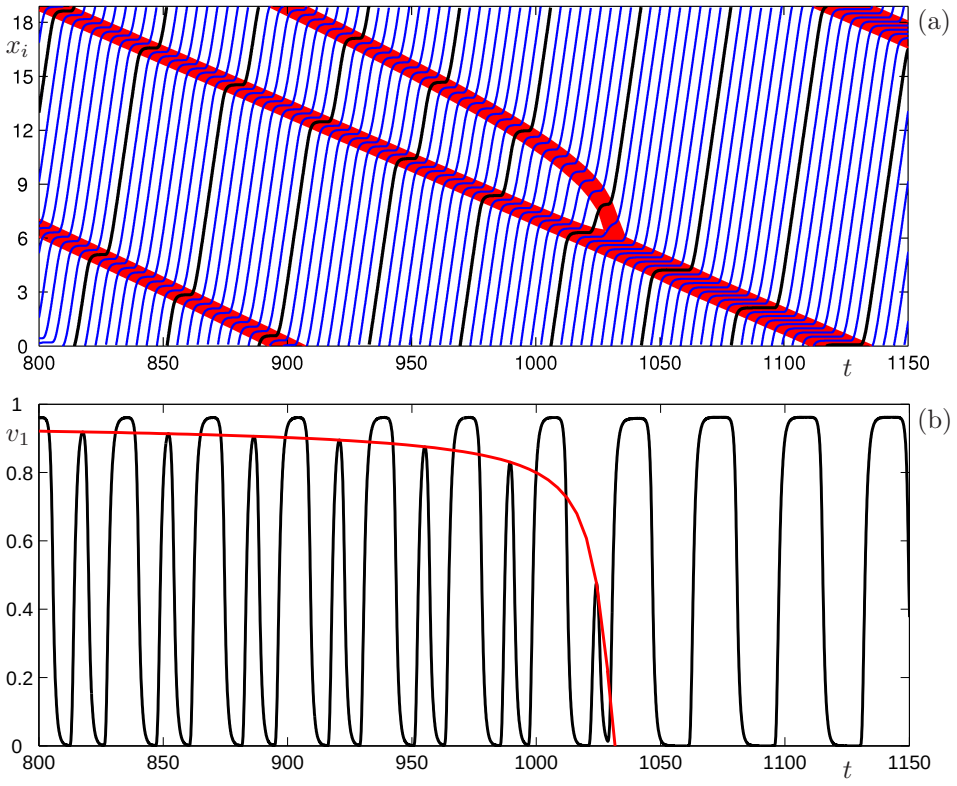

Fig. 5.5: Plot of the positions x_i of all $n = 9$ cars (a), and velocity v_1 of the first car (b), when two traffic jams merge. In panel (a), the trajectory of the first car is emphasized in black and traffic jams are indicated in red when the velocity drops below $v^0/3$. The motion of fronts corresponds to the modulated solution in Fig. 5.3(a). In panel (b), the red curve envelopes the maxima of velocities between the traffic jams. The other parameters are $v^0 = 1.0$, $\alpha = 1.0$, and $h^* = 2.1$.

When one starts an initial value simulation of the system from suitably random initial data, unstable waves form and will eventually die out. (Specifically, we start from equidistant cars with velocities chosen randomly and uniformly from $[0, v^0]$, and integrate the system with an explicit Euler method with time step 0.01.) As was mentioned in Section 5.2, already for $n = 9$ cars we find that waves for $k = 2$, corresponding to two traffic jams along the ring, may survive for considerable amounts of time. In other words, weakly unstable traffic jams appear as long transients. When they eventually disappear this can happen in one of two competing ways, which are shown in Figs. 5.5 and 5.6 respectively.

In the case shown in Fig. 5.5 a traffic jam catches up with another traffic jam and the two

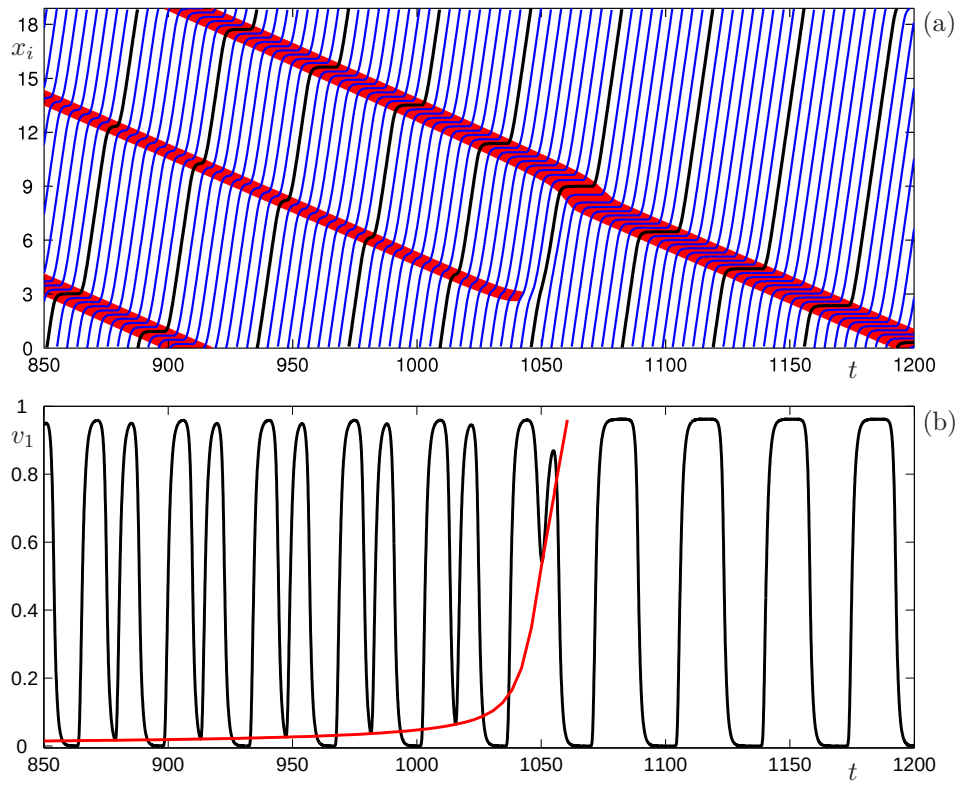

Fig. 5.6: Plot of the positions x_i of all $n = 9$ cars (a), and the velocity v_1 of the first car (b), when a traffic jam disperses. In panel (a), the trajectory of the first car is emphasized in black and traffic jams are indicated in red when the velocity drops below $v^0/3$. The motion of fronts corresponds to the modulated solution in Fig. 5.3(b). In panel (b), the red curve envelopes the minima of velocities in the dispersing traffic jam. The other parameters are $v^0 = 1.0$, $\alpha = 1.0$, and $h^* = 2.1$.

then merge. The positions of all vehicles are displayed in Fig. 5.5(a), which shows that the go-front of the first and the stop-front of the second traffic jam 'move towards one another' and are then annihilated. This behavior is indicative of an unstable eigendirection of the periodic orbit for $k = 2$ as shown in Fig. 5.3(a), where the stop-front and the go-front of a low-velocity plateau move in the same direction (along the periodic orbit). As a consequence of merging, the region between the two traffic jams of flowing traffic (large velocity) disappears. Fig. 5.5(b) shows the velocity profile of the first car. As the two traffic jams move closer together the maximum velocity between them decreases: the envelope of these maxima (red curve) diverges more and more from the maximum velocity elsewhere along the ring. Thus, the time until complete merging can be defined as the moment that this envelope reaches

zero velocity. The envelope actually describes the local maxima of the velocity for all cars; note that the velocity profiles of the other cars are very similar, but are not shifted copies, since the dynamics is not perfectly periodic.

In contrast, Fig. 5.6 shows a situation where a traffic jam fails to merge with another traffic jam, but rather disperses. As can be seen from the positions of cars plotted in Fig. 5.6(a), in this case, the stop-front and the go-front of one and the same traffic jam slowly 'move closer together'. Thus this traffic jam eventually disappears which has only a slight influence on the 'neighboring' traffic jam. This behaviour is associated with an unstable eigendirection of the $k = 2$ periodic orbit as shown in Fig. 5.3(b), where the stop-front and the go-front of a low-velocity plateau move in opposite directions (along the periodic orbit). The velocity profile of the first car is displayed in Fig. 5.6(b), showing that the minimum velocity in the dispersing traffic jam increases. This is again indicated by the envelope of these minima (red curve), which also describes the minima for all cars. This envelope diverges from being practically zero and complete dispersion is reached when it reaches the maximum velocity on the ring.

Note that the above investigation only explains the behaviour of the system close to the periodic solution, i.e., in the case when the fronts are close to parallel. The actual merging dynamics, however, is nonlinear and requires the full investigation of the nonlinear slow manifolds on which front dynamics occur. Nevertheless, as the wave number k is decreased, the distance of Floquet multipliers from the unit circle shows exponential decaying (according to formula (5.4) and Fig. 5.4) and the merging time shows exponential increasing (according to simulations like Fig. 5.1(b)). Our tentative hypothesis is that these exponential behaviours correspond to each other.

Chapter 6

Conclusion

Now we present a summary of the key results of the thesis, discuss some possible extensions, and present some open questions.

6.1 Summary of thesis

In this thesis we investigated the fundamental dynamics of highway traffic paying special attention to the effects due to the reaction time delay of drivers. We considered an optimal-velocity car-following model, posed on a ring (circular road), in which delay was included explicitly. The resulting system of autonomous delay differential equations was investigated by using the elements of analytical and numerical bifurcation theory. Thus we were able to study the qualitative changes of the nonlinear dynamics of the system as the parameters (the average headway, the sensitivity and the desired speed of drivers) were varied.

First, the linear stability of the uniform flow equilibrium was investigated. We showed that the system undergoes a sequence of Hopf bifurcations as the average headway is varied, and consequently oscillations with different frequencies can appear. These periodic solutions manifest themselves as upstream travelling waves with different wave numbers. The inclusion of delay results in qualitative changes in the stability diagrams: for large enough desired speed

the uniform flow equilibrium cannot be stabilised by increasing the sensitivity (in contrast to what happens in the non-delayed system, in which the reaction time of drivers is set to zero).

After eliminating the continuous translational symmetry along the ring road, normal form calculations were used to investigate the stability of the consequent oscillations in the vicinity of the Hopf bifurcation points. It was proved that these bifurcations are robustly subcritical due to the reaction time delay, that is, the oscillations and the corresponding travelling waves are unstable in the neighbourhood of the Hopf bifurcation points. This revealed the possibility that, if a subsequent fold bifurcation were to occur, then the stable uniform flow equilibrium might co-exist with stable oscillations giving a bistability in the system. Consequently, large enough perturbations, such as a truck pulling out of its lane, may trigger traffic jams even when the uniform flow is stable.

In order to investigate the oscillations and travelling waves at the fully nonlinear level (far from the Hopf bifurcation points), numerical continuation techniques were used. We followed branches of periodic solutions born at the Hopf bifurcation points by varying the average headway and we detected fold bifurcations and other qualitative changes (such us collision and stopping) along the branches. By performing these continuations for several different values of the sensitivity parameter, two-dimensional bifurcation diagrams were developed in which domains of bistability, co-existence, stopping, and collision were identified. As the number of cars was increased, we identified trends in the two-dimensional bifurcation diagrams as well as in the branches of periodic solutions.

Furthermore, detailed examination of the oscillation profiles revealed that for larger numbers of cars, stop-fronts and go-fronts develop that correspond to the entry and exit points of traffic jams. By studying the linear stability of periodic solutions and by applying numerical simulation, we also gained information about the relative motion of these fronts. A low-dimensional slow dynamics of fronts was discovered: they travel with approximately the same speed (hence with small relative speed) over long time scales until they annihilate or disperse.

6.2 Possibilities for future work

We were able to carry out the linear and the weakly nonlinear analysis for arbitrarily many vehicles. However, due to limitations in memory and CPU time, we were only able to perform numerical continuation up to about twenty cars. In order to extend this number up to at least hundreds of vehicles, new numerical methods must be brought to bear: e.g., by using the recent package [116].

Furthermore, the fully nonlinear analysis of the slow manifolds connecting the periodic solutions, discussed in Chapter 5, is another challenging area where manifold-continuation techniques may prove useful [44, 69]. Alternatively, the slow front dynamics might be explored via asymptotic analysis of PDE limits [120].

Note that the bifurcation methods used in this thesis could be applied to *any* car-following model. It would be interesting to investigate how higher fidelity car-following models behave with and without delay. For example, as a first step, one might include the effects of relative velocity as in [38] where the model

$$\dot{v}_i(t) = \alpha\big(h_i(t)\big)\Big(\mathrm{V}\big(h_i(t)\big) - v_i(t) + \dot{h}_i(t)\,\mathrm{W}\big(h_i(t)\big)\Big) \tag{6.1}$$

is considered with positive monotone increasing optimal velocity function $\mathrm{V}(h)$ and with positive monotone decreasing sensitivity functions $\alpha(h)$ and $\mathrm{W}(h)$. In the parenthesis on the right-hand side, the optimal velocity term is kept in its original form (see (1.13)), while the last term expresses that drivers try to match the velocity of the preceding vehicle more, the closer they are. Indeed, the reaction time delay may be included in this model too.

It is possible that the strict order of periodic branches is not satisfied for some parameter ranges so that they may intersect each other, providing more complicated dynamics. It is also an issue to change the boundary conditions since the interaction of fronts may be stronger/weaker for open boundary conditions, which is a more realistic setup for real-world traffic situations.

Nevertheless, it is in question whether the dynamics explored by the above methods is

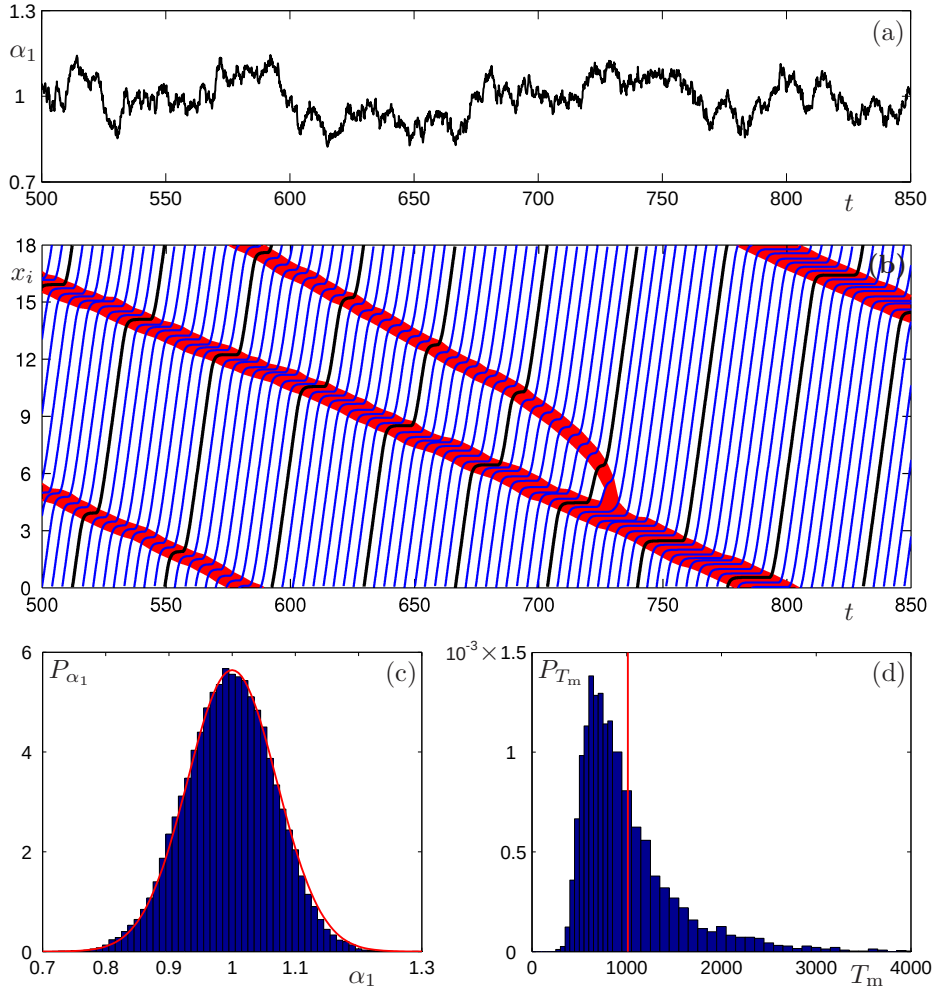

Fig. 6.1: Random walk of sensitivity α_1 of the first car (a), positions x_i of all $n = 9$ cars (b), distribution of sensitivity α_1 of the first car (c), and distribution of the merging time T_m (d), when two traffic jams merge in the presence of noise. In panel (b), the trajectory of the first car is emphasized in black and traffic jams are indicated in red when the velocity drops below $v^0/3$. In panel (c), the red curve is the analytical solution for the equilibrium distribution of the sensitivity. In panel (d), the red vertical line at $T_m = 1011.96$ shows the merging time in the deterministic case. The other parameters are $v^0 = 1.0$, $\alpha = 1.0$, $h^* = 2.0$, $\gamma = 0.1$, and $\kappa = 0.0316$.

robust. The inconsistent psychological behaviour of drivers and external disturbances such as weather and road unevenness indicate that one should include stochastic effects. To conclude this thesis we give brief details of some initial work in this area. Stochasticity might be modelled, for example, by assuming that the sensitivity parameter of each driver is subjected

to a random walk according to

$$\dot{\alpha}_i(t) = \gamma\big(\alpha - \alpha_i(t)\big) + \kappa\zeta_i(t)\,, \quad i = 1, \ldots, n\,, \tag{6.2}$$

where ζ_i is assumed to be white (uncorrelated) Gaussian noise, that is,

$$\overline{\zeta_i(t)} = 0\,, \quad \overline{\zeta_j(t)\zeta_k(s)} = \delta_{jk}\,\delta(t-s)\,. \tag{6.3}$$

Here the overbar stands for averaging, $1/\gamma$ is a relaxation time while κ gives the noise strength. One realization of this random walk of the sensitivity for a single vehicle is shown in Fig. 6.1(a) and the resulting distribution is represented by the histogram in Fig. 6.1(c). Note that here drivers are still considered to be identical in the sense that their α_i parameters fluctuate around the same mean value with the same variance according to the same distribution. An alternative (perhaps more realistic) approach might be for α_i to be sampled from different distributions so as to model different driver/vehicle classes. However, multi-class models must include interactions due to lane changes, and in that sense all of this analysis is limited.

Equation (6.2) is sometimes called Ornstein-Uhlenbeck process and the solution for the distribution of α_i can be obtained from the related Fokker-Planck equation; see [37]. In particular, the (stable) equilibrium distribution of α_i is given by

$$p^{\mathrm{eq}}(\alpha_i) = \sqrt{\frac{\gamma}{\kappa^2\pi}}\,\mathrm{e}^{-\frac{\gamma}{\kappa^2}(\alpha_i-\alpha)}\,, \quad i = 1, \ldots, n\,, \tag{6.4}$$

which is shown by the red curve in Fig. 6.1(c). By using this as an initial distribution for α_i the stochastic transients are eliminated.

Initial simulations show that the above noise effects do not destroy the qualitative dynamics of the merging and dispersing of traffic jams, but the front motions become noisy; compare Fig. 5.5(a) and Fig. 5.6(a) with Fig. 6.1(b). The preliminary results, displayed in Fig. 6.1(d), suggest that the most probable merging time T_{m} is smaller than in the deterministic case (red vertical line) but the merging time distribution has an exponential-like tail. According to the literature of passage-time distributions [83], this distribution suggests that on the top of the macroscopic nonlinear dynamics of the fronts there is a 'macroscopic' random walk, which originated from the 'microscopic' random walk of the sensitivity. We leave the further analysis of this effect and the search for more interesting features for the future.

Appendix A

Trigonometric identities

Let us consider the wave numbers $k = 1, \ldots, n/2$ (even n) or $k = 1, \ldots, (n-1)/2$ (odd n). We have

$$\sum_{i=1}^{n} \exp(\mathrm{i}\varrho \tfrac{2k\pi}{n} i) = \begin{cases} 0\,, & \text{if} \quad k \neq n/\varrho\,, \\ n\,, & \text{if} \quad k = n/\varrho\,, \end{cases} \tag{A.1}$$

where i is the imaginary unit, $i = 1, \ldots, n$, and $\rho = 1, \ldots, 4$. Therefore, the following identities can be proven.

In first order

$$\sum_{i=1}^{n} \cos(\tfrac{2k\pi}{n} i) = 0\,, \tag{A.2}$$

$$\sum_{i=1}^{n} \sin(\tfrac{2k\pi}{n} i) = 0\,. \tag{A.3}$$

In second order

$$\sum_{i=1}^{n} \cos^2(\tfrac{2k\pi}{n} i) = \begin{cases} n/2\,, & \text{if} \quad k \neq n/2\,, \\ n\,, & \text{if} \quad k = n/2\,, \end{cases} \tag{A.4}$$

$$\sum_{i=1}^{n} \sin^2(\tfrac{2k\pi}{n} i) = \begin{cases} n/2\,, & \text{if} \quad k \neq n/2\,, \\ 0\,, & \text{if} \quad k = n/2\,, \end{cases} \tag{A.5}$$

$$\sum_{i=1}^{n} \cos(\tfrac{2k\pi}{n} i) \sin(\tfrac{2k\pi}{n} i) = 0\,. \tag{A.6}$$

In third order

$$\sum_{i=1}^{n} \cos^3(\tfrac{2k\pi}{n} i) = \begin{cases} 0\,, & \text{if} \quad k \neq n/3\,, \\ n/4\,, & \text{if} \quad k = n/3\,, \end{cases} \tag{A.7}$$

$$\sum_{i=1}^{n} \sin^3(\tfrac{2k\pi}{n} i) = 0\,, \tag{A.8}$$

$$\sum_{i=1}^{n} \cos^2(\tfrac{2k\pi}{n} i) \sin(\tfrac{2k\pi}{n} i) = 0\,, \tag{A.9}$$

$$\sum_{i=1}^{n} \cos(\tfrac{2k\pi}{n} i) \sin^2(\tfrac{2k\pi}{n} i) = \begin{cases} 0\,, & \text{if} \quad k \neq n/3\,, \\ -n/4\,, & \text{if} \quad k = n/3\,. \end{cases} \tag{A.10}$$

In fourth order

$$\sum_{i=1}^{n} \cos^4(\tfrac{2k\pi}{n} i) = \begin{cases} 3n/8\,, & \text{if} \quad k \neq n/2 \quad \text{and} \quad k \neq n/4\,, \\ n\,, & \text{if} \quad k = n/2\,, \\ n/2\,, & \text{if} \quad k = n/4\,, \end{cases} \tag{A.11}$$

$$\sum_{i=1}^{n} \sin^4(\tfrac{2k\pi}{n} i) = \begin{cases} 3n/8\,, & \text{if} \quad k \neq n/2 \quad \text{and} \quad k \neq n/4\,, \\ 0\,, & \text{if} \quad k = n/2\,, \\ n/2\,, & \text{if} \quad k = n/4\,, \end{cases} \tag{A.12}$$

$$\sum_{i=1}^{n} \cos^3(\tfrac{2k\pi}{n} i) \sin(\tfrac{2k\pi}{n} i) = 0\,, \tag{A.13}$$

$$\sum_{i=1}^{n} \cos(\tfrac{2k\pi}{n} i) \sin^3(\tfrac{2k\pi}{n} i) = 0\,, \tag{A.14}$$

$$\sum_{i=1}^{n} \cos^2(\tfrac{2k\pi}{n} i) \sin^2(\tfrac{2k\pi}{n} i) = \begin{cases} n/8\,, & \text{if} \quad k \neq n/2 \quad \text{and} \quad k \neq n/4\,, \\ 0\,, & \text{if} \quad k = n/2\,, \\ 0\,, & \text{if} \quad k = n/4\,. \end{cases} \tag{A.15}$$

Bibliography

Technical references on traffic

[1] Active Traffic Management, Highways Agency, United Kingdom. http://www.highways.gov.uk/knowledge/tcc/atm/index.htm.

[2] Britain's nightmare roads. 22 April 2002. *BBC, 4×4 Reports*, http://news.bbc.co.uk/1/hi/programmes/4x4_reports/britain_in_a_jam/1938177.stm.

[3] Highways Agency. http://www.highways.gov.uk.

[4] Lab studying science behind traffic patterns. 5 August 1999. *Washington Post*, http://www.washingtonpost.com/wp-srv/national/daily/aug99/traffic05.htm.

[5] M25 Motorway. http://en.wikipedia.org/wiki/M25_motorway.

[6] Micro-simulation tools. http://www.microsimulation.drfox.org.uk/tools.html.

[7] MIDAS, Motorway Incident Detection and Automatic Signalling. http://en.wikipedia.org/wiki/Motorway_Incident_Detection_and_Automatic_Signalling.

[8] Ramp Metering. http://en.wikipedia.org/wiki/Ramp_meter.

[9] Ramp Metering, Highways Agency, United Kingdom. http://www.highways.gov.uk/aboutus/corpdocs/10_year_plan/rampmet/index.htm.

[10] Road File 2004, RAC Foundation. http://www.racfoundation.org/content/category/38/31/.

[11] Study ranks July 4 vacation bottlenecks. 30 June 2005. *CNN*, http://edition.cnn.com/2005/TRAVEL/06/29/vacation.bottlenecks.

[12] Traffic: Invisible shockwaves that put you in a jam. 15 June 2003. *The Sunday Times, Driving*, http://www.timesonline.co.uk/article/0,,2105-712316,00.html.

[13] Transport Ten Year Plan 2000, Department for Transport, United Kingdom Government. http://www.dft.gov.uk/stellent/groups/dft_about/documents/page/dft_about_503944.hcsp.

Scientific references

[14] M. Bando, K. Hasebe, K. Nakanishi, and A. Nakayama. Analysis of optimal velocity model with explicit delay. *Physical Review E*, 58(5):5429–5435, 1998.

[15] M. Bando, K. Hasebe, A. Nakayama, A. Shibata, and Y. Sugiyama. Dynamical model of traffic congestion and numerical simulation. *Physical Review E*, 51(2):1035–1042, 1995.

[16] S. Benzoni-Gavage and R. M. Colombo. An n-populations model for traffic flow. *European Journal of Applied Mathematics*, 14(5):587–612, 2003.

[17] P. Berg. *Optimal-Velocity Models of Motorway Traffic*. PhD thesis, School of Mathematics, University of Bristol, 2001.

[18] P. Berg, A. D. Mason, and A. W. Woods. Continuum approach to car-following models. *Physical Review E*, 61(2):1056–1066, 2000.

[19] P. Berg and R. E. Wilson. Bifurcation analysis of meta-stability and waves of the OV model. In S. P. Hoogendoorn, S. Luding, P. H. L. Bovy, M. Schreckenberg, and D. E. Wolf, editors, *Traffic and Granular Flow '03*, pages 247–252. Springer-Verlag, Berlin, 2005.

[20] P. Berg and A. W. Woods. On-ramp simulations and solitary waves of a car-following model. *Physical Review E*, 64(3):035602, 2001.

[21] S. A. Campbell and J. Bélair. Analytical and symbolically-assisted investigations of Hopf bifurcations in delay-differential equations. *Canadian Applied Mathematics Quarterly*, 3(2):137–154, 1995.

[22] S. A. Campbell, Y. Yuan, and S. D. Bungay. Equivariant Hopf bifurcation in a ring of identical cells with delayed coupling. *Nonlinearity*, 18(6):2827–2846, 2005.

[23] J. Carr and R. L. Pego. Metastable patterns in solutions of $u_t = \epsilon^2 u_{xx} - f(u)$. *Communications on Pure and Applied Mathematics*, 42(5):523–576, 1989.

[24] J. Carr and R. L. Pego. Invariant manifolds for metastable patterns in $u_t = \epsilon^2 u_{xx} - f(u)$. *Proceedings of the Royal Society of Edinburgh A*, 116(1-2):133–160, 1990.

[25] R. E. Chandler, R. Herman, and E. W. Montroll. Traffic dynamics: studies in car following. *Operations Research*, 6(2):164–184, 1958.

[26] C. F. Daganzo. A behavioral theory of multi-lane traffic flow. Part I: Long homogeneous freeway sections. *Transportation Research B*, 36(2):131–158, 2002.

[27] C. F. Daganzo. A behavioral theory of multi-lane traffic flow. Part II: Merges and the onset of congestion. *Transportation Research B*, 36(2):159–169, 2002.

[28] L. C. Davis. Comment on "Analysis of optimal velocity model with explicit delay". *Physical Review E*, 66(3):038101, 2002.

[29] L. C. Davis. Modification of the optimal velocity traffic model to include delay due to driver reaction time. *Physica A*, 319:557–567, 2003.

[30] L. C. Davis. Multilane simulations of traffic phases. *Physical Review E*, 69(1):016108, 2004.

[31] O. Diekmann, S. A. van Gils, S. M. Verduyn Lunel, and H. O. Walther. *Delay Equations: Functional-, Complex-, and Nonlinear Analysis*, volume 110 of *Applied Mathematical Sciences*. Springer-Verlag, New York, 1995.

[32] E. J. Doedel, A. R. Champneys, T. F. Fairgrieve, Yu. A. Kuznetsov, B. Sandstede, and X. Wang. AUTO97: Continuation and bifurcation software for ordinary differential equations. Technical report, Department of Computer Science, Concordia University, Montreal, Canada, 1997. `http://indy.cs.concordia.ca/auto/`.

[33] L. C. Edie. Car-following and steady-state theory for noncongested traffic. *Operations Research*, 9(1):66–76, 1961.

[34] K. Engelborghs, T. Luzyanina, K. J. In't Hout, and D. Roose. Collocation methods for the computation of periodic solutions of delay differential equations. *SIAM Journal on Scientific Computing*, 22(5):1593–1609, 2000.

[35] K. Engelborghs, T. Luzyanina, and D. Roose. Numerical bifurcation analysis of delay differential equations using DDE-BIFTOOL. *ACM Transactions on Mathematical Software*, 28(1):1–21, 2002.

[36] K. Engelborghs, T. Luzyanina, and G. Samaey. DDE-BIFTOOL v. 2.00: A Matlab package for bifurcation analysis of delay differential equations. Technical Report TW-330, Department of Computer Science, Katholieke Universiteit Leuven, Belgium, 2001. `http://www.cs.kuleuven.ac.be/~koen/delay/ddebiftool.shtml`.

[37] S. R. Finch. Ornstein-Uhlenbeck process, Tutorial. 2004. `http://pauillac.inria.fr/algo/csolve/ou.pdf`.

[38] I. Gasser, T. Seidel, G. Sirito, and B. Werner. Bifurcation analysis of a class of 'car-following' traffic models II: Variable reaction times and aggressive drivers. to appear in *Transport Theory and Statistical Physics*, 2005. `http://www.math.uni-hamburg.de/math/research/preprints/hbama.html`.

[39] I. Gasser, G. Sirito, and B. Werner. Bifurcation analysis of a class of 'car-following' traffic models. *Physica D*, 197(3-4):222–241, 2004.

[40] D. C. Gazis, R. Herman, and R. B. Potts. Car-following theory of steady-state traffic flow. *Operations Research*, 7(4):499–505, 1959.

[41] D. C. Gazis, R. Herman, and R. W. Rothery. Nonlinear follow-the-leader models of traffic flow. *Operations Research*, 9(4):545–567, 1961.

[42] P. G. Gipps. A behaviourial car-following model for computer simulation. *Transportation Research B*, 15(2):105–111, 1981.

[43] K. Green and B. Krauskopf. Global bifurcations and bistability at the locking boundaries of a semiconductor laser with phase-conjugate feedback. *Physical Review E*, 66(1):016220, 2002.

[44] K. Green, B. Krauskopf, and K. Engelborghs. One-dimensional unstable eigenfunction and manifold computations in delay differential equations. *Journal of Computational Physics*, 197(1):86–98, 2004.

[45] K. Green, B. Krauskopf, and G. Samaey. A two-parameter study of the locking region of a semiconductor laser subject to phase-conjugate feedback. *SIAM Journal on Applied Dynamical Systems*, 2(2):254–276, 2003.

[46] J. M. Greenberg, A. Klar, and M. Rascle. Congestion on multilane highways. *SIAM Journal on Applied Mathematics*, 63(3):818–833, 2003.

[47] J. Guckenheimer and P. Holmes. *Nonlinear Oscillations, Dynamical Systems, and Bifurcations of Vector Fields*, volume 42 of *Applied Mathematical Sciences*. Springer-Verlag, New York, 3rd edition, 1997.

[48] B. Haegeman, K. Engelborghs, D. Roose, D. Pieroux, and T. Erneux. Stability and rupture of bifurcation bridges in semiconductor lasers subject to optical feedback. *Physical Review E*, 66:046216, 2002.

[49] J. K. Hale, L. T. Magelhães, and W. M. Oliva. *Dynamics in Infinite Dimensions*, volume 47 of *Applied Mathematical Sciences*. Springer-Verlag, New York, 2nd edition, 2002.

[50] J. K. Hale and S. M. Verduyn Lunel. *Introduction to Functional Differential Equations*, volume 99 of *Applied Mathematical Sciences*. Springer-Verlag, New York, 1993.

[51] B. D. Hassard, N. D. Kazarinoff, and Y.-H. Wan. *Theory and Applications of Hopf Bifurcation*, volume 41 of *London Mathematical Society Lecture Note Series*. Cambridge University Press, Cambridge, 1981.

[52] D. Helbing. Theoretical foundation of macroscopic traffic models. *Physica A*, 219(3-4):375–390, 1995.

[53] D. Helbing. Traffic and related self-driven many-particle systems. *Reviews of Modern Physics*, 73(4):1067–1141, 2001.

[54] D. Helbing and B. Tilch. Generalized force model of traffic dynamics. *Physical Review E*, 58(1):133–138, 1998.

[55] R. Herman, E. W. Montroll, R. B. Potts, and R. W. Rothery. Traffic dynamics: analysis of stability in car following. *Operations Research*, 7(1):86–106, 1959.

[56] N. O. Hodas and A. Jagota. Microscopic modeling of multi-lane highway traffic flow. *American Journal of Physics*, 71(12):1247–1256, 2003.

[57] E. N. Holland. A generalized stability criterion for motorway traffic. *Transportation Research B*, 32(2):141–154, 1998.

[58] Y. Igarashi, K. Itoh, K. Nakanishi, K. Ogura, and K. Yokokawa. Bifurcation phenomena in the optimal velocity model for traffic flow. *Physical Review E*, 64(4):047102, 2001.

[59] T. Insperger and G. Stépán. Updated semi-discretization method for periodic delay-differential equations with discrete delay. *International Journal for Numerical Methods in Engineering*, 61(1):117–141, 2004.

[60] W. Just. On the eigenvalue spectrum for time-delayed Floquet problems. *Physica D*, 142(1-2):153–165, 2000.

[61] T. Kalmár-Nagy, G. Stépán, and F. C. Moon. Subcritical Hopf bifurcation in the delay equation model for machine tool vibrations. *Nonlinear Dynamics*, 26(2):121–142, 2001.

[62] B. S. Kerner. Experimental features of self-organization in traffic flow. *Physical Review Letters*, 81(17):3797–3800, 1998.

[63] B. S. Kerner. The physics of traffic. *Physics World*, (August):25–30, 1999.

[64] B. S. Kerner and S. L. Klenov. A microscopic model for phase transitions in traffic flow. *Journal of Physics A*, 35(3):L31–L43, 2002.

[65] B. S. Kerner and P. Konhäuser. Cluster effect in initially homogeneous traffic flow. *Physical Review E*, 48(4):R2335–R2338, 1993.

[66] B. S. Kerner and H. Rehborn. Experimental properties of phase transitions in traffic flow. *Physical Review Letters*, 79(20):4030–4033, 1997.

[67] V. B. Kolmanovskii and A. D. Myshkis. *Introduction to the Theory and Applications of Functional Differential Equations*, volume 463 of *Mathematics and Its Applications*. Kluwer Academic Publishers, London, 1999.

[68] V. B. Kolmanovskii and V. R. Nosov. *Stability of Functional Differential Equations*, volume 180 of *Mathematics in Science and Engineering*. Academic Press, Inc., London, 1986.

[69] B. Krauskopf and K. Green. Computing unstable manifolds of periodic orbits in delay differential equations. *Journal of Computational Physics*, 186(1):230–249, 2003.

[70] S. Krauss, P. Wagner, and C. Gawron. Continuous limit of the Nagel-Schreckenberg model. *Physical Review E*, 54(4):3707–3712, 1996.

[71] T. Krisztin. Convergence of solutions of a nonlinear integro-differential equation arising in compartmental systems. *Acta Scientiarum Mathematicarum*, 47(3-4):471–485, 1984.

[72] R. D. Kühne. Macroscopic freeway model for dense traffic – Stop-start waves and incident detection. In J. Volmuller and R. Hamerslag, editors, *Proceedings of the Ninth International Symposium on Transportation and Traffic Theory*, pages 21–42. VNU Science Press, Utrecht, The Netherlands, 1984.

[73] Yu. A. Kuznetsov. *Elements of Applied Bifurcation Theory*, volume 112 of *Applied Mathematical Sciences*. Springer-Verlag, New York, 2nd edition, 1998.

[74] H. K. Lee, H.-W. Lee, and D. Kim. Macroscopic traffic models from microscopic car-following models. *Physical Review E*, 64(5):056126, 2001.

[75] H. Lenz, C. K. Wagner, and R. Sollacher. Multi-anticipative car-following model. *The European Physical Journal B*, 7(2):331–335, 1999.

[76] M. J. Lighthill and G. B. Whitham. On kinematic waves II: A theory of traffic flow on long crowded roads. *Proceedings of the Royal Society of London A*, 229(1178):317–345, 1955.

[77] D. J. Low and P. S. Addison. A nonlinear temporal headway model of traffic dynamics. *Nonlinear Dynamics*, 16(2):127–151, 1998.

[78] I. Lubashevsky, R. Mahnke, P. Wagner, and S. Kalenkov. Long-lived states in synchronized traffic flow: Empirical prompt and dynamical trap model. *Physical Review E*, 66(1):016117, 2002.

[79] A. D. Mason and A. W. Woods. Car-following model of multispecies systems of road traffic. *Physical Review E*, 55(3):2203–2214, 1997.

[80] T. Nagatani. Traffic behaviour in mixture of different vehicles. *Physica A*, 284(1-4):405–420, 2000.

[81] K. Nagel and M. Schreckenberg. A cellular automaton model for freeway traffic. *Journal de Physique I*, 12(2):2221–2229, 1992.

[82] G. F. Newell. Nonlinear effects in the dynamics of car following. *Operations Research*, 9(2):209–229, 1961.

[83] S. H. Noskowicz and I. Goldhirsch. First-passage-time distribution in a random walk. *Physical Review A*, 42(4):2047–2064, 1990.

[84] G. Orosz. Hopf bifurcation calculations in delayed systems. *Periodica Polytechnica*, 48(2):189–200, 2004.

[85] G. Orosz, B. Krauskopf, and R. E. Wilson. Bifurcations and multiple traffic jams in a car-following model with reaction-time delay. *Physica D*, 211(3-4):277–293, 2005.

[86] G. Orosz and G. Stépán. Hopf bifurcation calculations in delayed systems with translational symmetry. *Journal of Nonlinear Science*, 14(6):505–528, 2004.

[87] G. Orosz and G. Stépán. Subcritical Hopf bifurcations in a car-following model with reaction-time delay. submitted to *Proceedings of the Royal Society of London A*, 2005. `http://www.enm.bris.ac.uk/anm/preprints/2005r17.html`.

[88] G. Orosz, R. E. Wilson, and B. Krauskopf. Bifurcations in a car-following model with delay. In W. Michiels and D. Roose, editors, *Fifth IFAC Workshop on Time-Delay Systems*. International Federation of Automatic Control (IFAC), Leuven, Belgium, 2004.

[89] G. Orosz, R. E. Wilson, and B. Krauskopf. Global bifurcation investigation of an optimal velocity traffic model with driver reaction time. *Physical Review E*, 70(2):026207, 2004.

[90] H. J. Payne. FREFLO: A macroscopic simulation model for freeway traffic. *Transportation Research Record*, 722:68–77, 1979.

[91] L. A. Pipes. Car following models and the fundamental diagram of road traffic. *Transportation Research*, 1(1):21–29, 1967.

[92] L. S. Pontryagin. On the zeros of some elementary transcendental functions. *AMS Translations, Series 2*, 1:95–110, 1955.

[93] I. Prigogine and R. Herman. *Kinetic Theory of Vehicular Traffic*. Elsevier, New York, 1971.

[94] V. Rottschäfer and B. Krauskopf. A three-parameter study of external cavity modes in semiconductor lasers with optical feedback. In W. Michiels and D. Roose, editors, *Fifth IFAC Workshop on Time-Delay Systems*. International Federation of Automatic Control (IFAC), Leuven, Belgium, 2004.

[95] L. A. Safonov, E. Tomer, V. V. Strygin, Y. Ashkenazy, and S. Havlin. Multifractal chaotic attractors in a system of delay-differential equations modeling road traffic. *CHAOS*, 12(4):1006–1014, 2002.

[96] L. A. Safonov, E. Tomer, V. V. Strygin, and S. Havlin. Periodic solutions of a non-linear traffic model. *Physica A*, 285(1-2):147–155, 2000.

[97] A. Sasoh. Impact of unsteady disturbance on multi-lane traffic flow. *Journal of the Physical Society of Japan*, 71(3):989–996, 2002.

[98] M. Sasvári and J. Kertész. Cellular automata models of single-lane traffic. *Physical Review E*, 56(4):4104–4110, 1997.

[99] S. Sawada. Nonlinear analysis of a differential-difference equation with next-nearest-neighbour interaction for traffic flow. *Journal of Physics A*, 34:11253–11259, 2001.

[100] L. P. Shayer and S. A. Campbell. Stability, bifurcation and multistability in a system of two coupled neurons with multiple time delays. *SIAM Journal on Applied Mathematics*, 61(2):673–700, 2000.

[101] V. Shvetsov and D. Helbing. Macroscopic dynamics of multilane traffic. *Physical Review E*, 59(6):6328–6339, 1999.

[102] J. Sieber and B. Krauskopf. Bifurcation analysis of an inverted pendulum with delayed feedback control near a triple-zero eigenvalue singularity. *Nonlinearity*, 17(1):85–104, 2004.

[103] R. Sipahi and N. Olgac. Degenerate cases in using the direct method. *Journal of Dynamic Systems Measurement and Control, Transactions of the ASME*, 125(2):194–201, 2003.

[104] G. Stépán. Great delay in a predator-prey model. *Nonlinear Analysis TMA*, 10(9):913–929, 1986.

[105] G. Stépán. *Retarded Dynamical Systems: Stability and Characteristic Functions*, volume 210 of *Pitman Research Notes in Mathematics*. Longman, Essex, England, 1989.

[106] G. Stépán and G. Haller. Quasiperiodic oscillations in robot dynamics. *Nonlinear Dynamics*, 8(4):513–528, 1995.

[107] Y. Sugiyama and H. Yamada. Aspects of optimal velocity model for traffic flow. In M. Schreckenberg and D. E. Wolf, editors, *Traffic and Granular Flow '97*, pages 301–318. Springer-Verlag, Singapore, 1998.

[108] R. Szalai. PDDE-CONT: A continuation and bifurcation software for delay-differential equations. Technical report, Massachusetts Institute of Technology, Cambridge, Massachusetts, USA, 2005. `http://www.mm.bme.hu/ szalai/pdde/`.

[109] R. Szalai, G. Stépán, and S. J. Hogan. Continuation of bifurcations in periodic delay differential equations using characteristic matrices. submitted to *SIAM Journal on Scientific Computing*, 2004. `http://www.enm.bris.ac.uk/anm/preprints/2004r23.html`.

[110] S. Tadaki, M. Kikuchi, and Y. Sugiyama S. Yukawa. Noise induced congested traffic flow in coupled map optimal velocity models. *Journal of the Physical Society of Japan*, 68(9):3110–3114, 1999.

[111] E. Tomer, L. A. Safonov, and S. Havlin. Presence of many stable nonhomogeneous states in an inertial car-following model. *Physical Review Letters*, 84(2):382–385, 2000.

[112] E. Tomer, L. A. Safonov, N. Madar, and S. Havlin. Optimization of congested traffic by controlling stop-and-go waves. *Physical Review E*, 65(6):065101(R), 2002.

[113] M. Treiber, A. Hennecke, and D. Helbing. Congested traffic states in empirical observations and microscopic simulations. *Physical Review E*, 62(2):1805–1824, 2000.

[114] M. Treiber, A. Kesting, and D. Helbing. Delays, inaccuracies and anticipation in microscopic traffic models. *Physica A*, 360(1):71–88, 2005.

[115] S. M. Verduyn Lunel and B. Krauskopf. The mathematics of delay equations with an application to the Lang-Kobayashi equations. In B. Krauskopf and D. Lenstra, editors, *Fundamental Issues of Nonlinear Laser Dynamics*, volume 548 of *AIP Conference Proceedings*, pages 66–86. American Institute of Physics, Melville, New York, 2000.

[116] K. Verheyden and K. Lust. A Newton-Picard collocation method for periodic solutions of delay differential equations. *BIT Numerical Mathematics*, 45(3):605–625, 2005.

[117] M. S. Watanabe. Dynamics of group motions controlled by signal processing: A cellular-automaton model and its applications. to appear in *Journal of Computational Methods in Sciences and Engineering*, 2005.

[118] G. B. Whitham. *Linear and Nonlinear Waves*. Wiley-Interscience, New York, 1999.

[119] R. E. Wilson. An analysis of Gipps's car-following model of highway traffic. *IMA Journal of Applied Mathematics*, 66(5):509–537, 2001.

[120] R. E. Wilson and P. Berg. Existence and classification of travelling wave solutions to second order highway traffic models. In M. Fukui, Y. Sugiyama, M. Schreckenberg, and D. E. Wolf, editors, *Traffic and Granular Flow '01*, pages 85–90. Springer-Verlag, Berlin, 2003.

[121] R. E. Wilson, P. Berg, S. Hooper, and G. Lunt. Many-neighbour interaction and non-locality in traffic models. *The European Physical Journal B*, 39(3):397408, 2004.